Spray-wall-flow interaction within a gasoline direct-injection (GDI) engine using Large Eddy Simulation

Spray-Wand-Strömung-Interaktion in einem Benzin-Direkteinspritzmotor (GDI) mittels Large Eddy Simulation

Zur Erlangung des akademischen Grades Doktor-Ingenieur (Dr.-Ing.)
Genehmigte Dissertation von Hao-Pin Lien aus Taichung city - Taiwan
Tag der Einreichung: 08.08.2023, Tag der Prüfung: 08.11.2023

1. Gutachten: Prof. Dr.-Ing. Christian Hasse
2. Gutachten: Prof. Dr.-Ing. Tommaso Lucchini
Darmstadt – D17

TECHNISCHE UNIVERSITÄT DARMSTADT

Mechanical Engineering Department

Simulation reaktiver Thermo-Fluid Systeme

Lien, Hao-Pin: Spray-wall-flow interaction within a gasoline direct-injection (GDI) engine using Large Eddy Simulation
Lien, Hao-Pin: Spray-Wand-Strömung-Interaktion in einem Benzin-Direkteinspritzmotor (GDI) mittels Large Eddy Simulation

Darmstadt, Technische Universität Darmstadt,
Year thesis published in TUprints 2023

Date of the submission: 08.08.2023
Date of thesis defense: 08.11.2023

URN: urn:nbn:de:tuda-tuprints-264302
URL: https://tuprints.ulb.tu-darmstadt.de/26430

Preface

This dissertation was written in the context of my work as a research assistant at TU Darmstadt. Parts of this work have already been published and submitted in the following publications:

- [1] Hao-Pin Lien et al. “Numerical studies of gasoline direct-injection sprays (ECN Spray G) under early- and late-injection conditions using Large Eddy Simulation and droplets-statistics-based Eulerian–Lagrangian framework”. en. In: *Fuel* 357 (Feb. 2024), p. 129708. ISSN: 00162361. DOI: 10.1016/j.fuel.2023.129708. URL: https://linkinghub.elsevier.com/retrieve/pii/S0016236123023220

- [2] Hao-Pin Lien et al. “Characteristics of near-wall flow and free-stream turbulence during the intake phase of a direct-injection engine”. In: *Int J Heat Fluid Flow* (2023)(Under Review)

- [3] Hao-Pin Lien et al. “Spray formation and spray-wall-flow interaction within a gasoline direct-injection (GDI) engine under early-injection conditions – a flow bench study”. In: *Int. J. Engine Res.* (2023)(Under Review)

Other publication related to this work is:

- [4] Yongxiang Li, Florian Ries, Yaquan Sun, Hao-Pin Lien, Kaushal Nishad, Amsini Sadiki. “Direct Numerical Simulation of Atomization Characteristics of ECN Spray-G Injector: In-Nozzle Fluid Flow and Breakup Processes”. In: Flow Turbul. Combust.(2023) DOI:10.1007/s10494-023-00514-2 (Accepted)

The Deutsche Forschungsgemeinschaft (DFG, German Research Foundation), and the Darmstadt Graduate School of Energy Science and Engineering funded part of this work.

The computing time was provided at the NHR Center NHR4CES at TU Darmstadt. This is funded by the Federal Ministry of Education and Research, and the state governments participating on the basis of the resolutions of the GWK for national high-performance computing at universities (www.nhr-verein.de/unsere-partner).

The successful completion and achievement of my Ph.D. study would not have been possible without wholehearted support, valuable advice, and guidance from numerous individuals whom I may not be able to mention individually. Nevertheless, I extend my gratitude and appreciation to everyone who contributed to this journey.

First and foremost, I am deeply grateful to my supervisor, Prof. Dr.-Ing. Christian Hasse. His unwavering support and vast knowledge provided me with the opportunity to pursue and accomplish my Ph.D. study.

I would also like to express my sincere thanks to Prof. Tommaso Lucchini from Politecnico di Milano for his invaluable support during the final stages of my Ph.D. study. Additionally, I am truly fortunate to have worked with and benefited from the wisdom of Prof. Dr.-Ing. Habil. Suad Jakirlic, particularly in discussions concerning turbulence-related topics.

My journey would not have been as enriching and fulfilling without the support and cheer from all my colleagues at the Simulation of Reactive Thermo-Fluid Systems (STFS) at the Technical University Darmstadt. I am especially grateful to my fellow colleagues in the OpneFOAM internal combustion engines group. Special thanks go to my group leader, Dr.-Ing. Andrea Pati, for his exceptional guidance and discussions. Moreover, I greatly appreciate the insightful discussions on near-wall physics with Dr.-Ing. Yongxiang Li from Reactive Flows and Diagnostics (RSM) at the Technical University Darmstadt.

The success of this work owes a debt of gratitude to the experimental support received from Reactive Flows and Diagnostics (RSM), Sandia National Laboratories, and the Engine Combustion Network (ECN). Access to the experimental data was crucial in enhancing my understanding of spray and in-cylinder flow and refining my modeling. I extend special thanks to Dr. Lyle Pickett, Dr. Tuan Nguyen, and Dr. Meghnaa Dhanji for their invaluable contributions and insightful discussions throughout the research process.

Finally, I wish to express my heartfelt appreciation to my family, especially my parents and my wife, Petra. The four-year journey of my Ph.D. was not without its challenges. Still, their unwavering support and encouragement played a vital role in my successful completion and attainment of the doctorate degree at the Technical University Darmstadt.

Abstract

With the need and urgency to the imposed regulation of zero-carbon emissions, the development of high-fidelity models for gasoline direct-injection (GDI) spray becomes crucial. This study first focuses on the development of robust Lagrangian models and a comprehensive exploration of the underlying physics across various operating conditions in a constant-volume chamber, ranging from early- to late-injection conditions. The Lagrangian models are extended to assess the spray-wall-flow interaction within an engine flow bench, simulating early-injection conditions of real GDI engines.

The concept of these models is based on a Direct Numerical Simulation (DNS) inner-nozzle flow simulation, indicating that the liquid spray experiences complete atomization near the injector hole. Consequently, the deformation and secondary breakup of liquid droplets play a significant role in spray evolution. The models' effectiveness and accuracy are meticulously validated against experimental data, including liquid and vapor phases obtained by diffuse back-illumination (DBI) and Schlieren measurements, respectively.

An important aspect of the research involves the investigation of different droplet distribution models. Using the blob method, assuming ejected droplet size equivalent to the injector diameter, is able to accurately capture global properties like liquid penetration length. However, it tends to cause delayed evaporation and breakup, resulting in an unphysical sharp plume tip downstream. To address future fuel-blended gasoline and E-fuels scenarios, the models have been extended to handle multi-component fuels. The successful simulation of a three-component gasoline surrogate (E00) demonstrates the models' capability to reproduce both the overall spray plume characteristics and the spatial distribution of high- and low-volatile fuels.

Furthermore, the research expands into the intricate spray-wall interaction within a constant-volume chamber under simulated cold start conditions. The simulation successfully replicates characteristic flows, such as wall jets and wall jet vortices induced by spray-wall interaction. Additionally, the phenomenon of spray cooling, resulting from air-entrainment-induced evaporation, is accurately reproduced. The simulated temperatures align closely with 0-D analytical results, exhibiting a temperature drop of about 20 K from its initial value. Although the simulation over-predicts heat transfer from the wall due to the constant temperature boundary condition, it matches the experimental

aggregate wall film thickness data on the target wall, 40 mm from the injector tip.

To comprehensively examine the spray-wall-flow interaction within a GDI engine, understanding the in-cylinder flow during the intake phase is imperative. Hence, a wall-resolved Large Eddy Simulation (LES) approach is employed to investigate free-stream and near-wall turbulence within an engine flow bench, simplifying the inherent complexity of the engine flow and focusing on the intake flow. The simulated in-cylinder large-scale motion and turbulence structure aligns well with reference experimental particle image velocimetry (PIV) data. Turbulence anisotropy analysis reveals a strong orientation toward axisymmetric expansion and contraction, respectively, attributed to the specific topological pattern of the engine flow characterized by the tumble vortex and the intake overflow jet. Moreover, the near-wall budget analysis facilitates investigating near-wall non-equilibrium effects, with a particular focus on the intake valve and liner wall region. The effects of the pressure gradient induced by the high Reynolds number intake flow are found to vary across different regions, suggesting that the classical wall function modeling approach based on the classical zero pressure gradient boundary layer may no longer be valid in internal combustion engines (ICEs) applications.

Finally, the knowledge gained from the study is applied to assess the spray-wall-flow interaction in an engine flow bench under various mass flow rates (MFRs). As MFRs increase, the spray-flow interaction intensifies, and the heterogeneous behavior of all spray plumes becomes apparent. Plumes oriented along the intake flow jet exhibit higher penetration and lower evaporation, while those not aligned with the intake jet stream exhibit increased evaporation and reduced penetration. This observation confirms the significant impact of air entrainment induced by the intake flow on both evaporation and penetration length. Additionally, wall wetting is observed on the intake valves, and convective evaporation effectively reduces the fuel film, cutting its residual mass by up to 50% compared to the no-flow case when the mass flow rate is 100%. Under early-injection conditions, although the global turbulence kinetic energy experiences a transient increase during the injection, it eventually returns to its original values.

Contents

1 Introduction

The regulation of exhaust gas and fuel efficiency for transportation sectors, including both light- and heavy-duty vehicles, has been more stringent in recent years. Such a trend leads to the increasing demand for environmentally friendly vehicles to reduce carbon dioxide (CO_2) emissions. More advanced development for ICEs toward high thermal efficiency and ultra-lean emissions are required [5]. Both goals have been successfully achieved by reducing the size of spark-ignition (SI) engines, using turbo-charging to increase the volumetric efficiency, and switching the injection system from port fuel injection (PFI) to gasoline direct-injection (GDI), facilitating lean-burn combustion strategies, as shown in Figure 1.1. [6, 7].

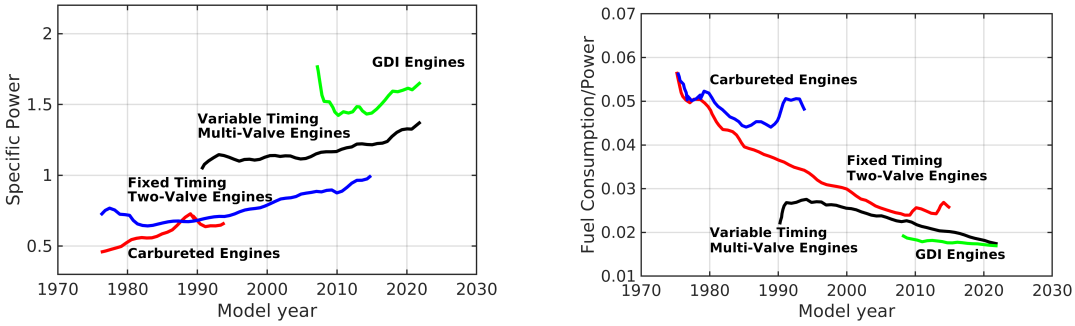

(a) Specific Power (HP/Displacement)

(b) Fuel consumption ((gal/mi)/HP)

Figure 1.1: Engine metrics for different gasoline technologies [7]

Since 2020, half of all new vehicles and approximately 30 percent of SUV truck sales have featured GDI engines [7]. This trend in the market shares is expected to be maintained by manufacturing more advanced GDI engines. Advanced GDI engines focus on improving the spray in-cylinder process, which involves spray, mixture formation, and combustion, to achieve homogeneous combustion and high fuel economy during full-load engine operation. During part-load engine operation, the spray-flow interaction is required to reach lean and ultra-lean stratified combustion without excessive unburned hydrocarbons and nitrogen oxides (NOx) [8]. Despite low carbon oxide (CO)

and nitrogen oxides (NOx) emission, GDI engines tend to produce HC formation due to the development of liquid fuel films on the piston and the cylinder wall in both early- and late-injection operating conditions. Particular attention has been devoted to understanding the wall-wetting-induced particulate matter (PM) emissions, especially soot formation [9, 10]. Thus, a great effort has been devoted to understanding spray formation and spray-wall-flow interaction to mitigate such problems and improve the combustion process [8, 11, 12].

1.1 Overview of GDI sprays and spray-wall-flow interaction

The development of GDI spray injectors, and their associated engine in-cylinder design have been transformed and improved over recent decades. To facilitate stratified combustion during part-load operation, the wall-guided in-cylinder system, in which the injector is installed on the intake side of the cylinder head, and the piston features a wedge shape, was first proposed with a notion that the air-fuel mixture supported by the large-scale motion of in-cylinder flow (tumble or swirl) is transported to the vicinity of the spark plug, as shown in Figure 1.2 [11, 13–15]. As the fuel in the wall-guided in-cylinder system was ejected on the piston, wall film deposit and dependency on the engine speed are the main challengings. To solve and advance the problems, the spray-guided in-cylinder system featuring the injector installed in the center of the cylinder head close to the spark plug was proposed. As the injector closed to the spark plug, the stratified air-fuel mixture can be achieved at the part-load condition, and the requirement of a repeatable spray pattern can be fulfilled under part- and full-load conditions. The development of a suitable GDI

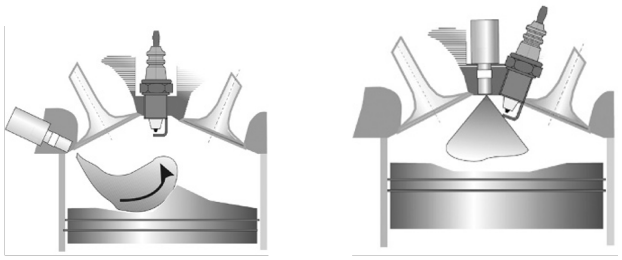

(a) Wall-guided (b) Spray-guided

Figure 1.2: Catagory of engine in-cylinder systems [13]; Reprinted with permission

injector starts from a swirl-type injector toward a multi-hole type injector, as shown in Figure 1.3. For atomization purposes, the swirl-type injector outweighs the hole-type

injector by allowing flow through the inner nozzle and further generating a hollow cone spray. This injector type is often used in wall-guided in-cylinder systems; however, it tends to produce fuel film on the spark plug and cylinder head due to its hollow-cone spray feature when installed within spray-guided systems. For spray-guided in-cylinder systems, a multi-hole injector is a better candidate with more concentrated plumes and more extended penetration. As GDI engines operate ranging from a cold start, part- to high-load conditions, the advantages of multi-hole injectors to the stratified combustion mode can become disadvantages to the others. Due to the lack of fuel atomization resulting in long penetration length, the multi-hole injector tends to produce a fuel film on the piston wall during a cold start condition. It also requires a proper air-fuel mixture supported by the in-cylinder flow to facilitate homogeneous combustion under high-load conditions.

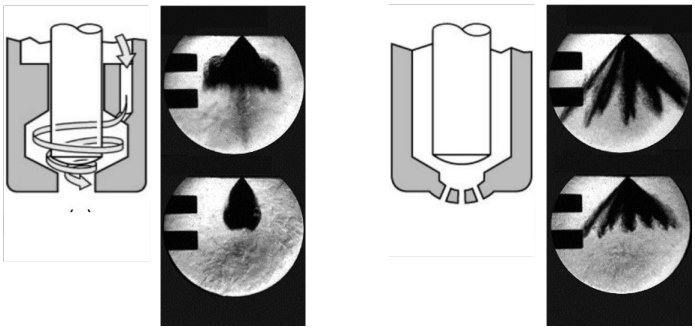

(a) Swirl-type injector (b) multi-hole type injector

Figure 1.3: Injector types and their spray morphology [13]; Reprinted with permission

Numerous studies have been dedicated to understanding the process and spray-wall-flow interaction from a constant-volume chamber to a real engine. The following literature reviews are split into the in-cylinder flow, spray formation and spray-flow interactions, and spray-wall interactions.

1.1.1 In-cylinder flow of GDI engines

Due to the complex geometry of ICEs, the wall boundary and the wall-influenced, pressure-induced turbulent in-cylinder flow effectively influence the performance of ICEs. During the intake phase, large-scale vortices are formed and determined by the geometry of the intake ports and intake valves. These coherent large-scale vortices are categorized as tumble and swirl based on their rotation [16]. During the evolution of these flow patterns,

the turbulent kinetic energy is retained, and the large-scale vortices further dissipate into numerous small-scale vortices during the compression phase. These small-scale vortices affect the mixing of fuel and oxidizer and further determine the burning rate and flame propagation during combustion [17].

Laser diagnostics in ICEs represents a reliable methodology for more in-depth investigation and visualization of the in-cylinder flow [18–27]. Such experiments provide detailed insights into turbulence structures and their evolution during engine cycles. Furthermore, they produce reference and validation data for numerical simulations. Recently, one study utilized particle image velocimetry (PIV) and tomographic particle image velocimetry (TPIV) in a motored direct-injection spark-ignition (DISI) engine to understand the instantaneous turbulence and its anisotropy phenomena [26]. The study reveals that the engine flow contains three-component isotropy, one-component axisymmetric expansion, and one-component axisymmetric contraction in both the intake and compression phases. Another study also exploited micro-particle image velocimetry (μ-PIV) measurement to investigate wall-flow interaction and the thermal and viscous boundary layer in ICEs [27].

Despite the advantages of experimental research on ICEs, such as the availability of greater statistics, such research is often constrained by an observation window and obstacles. Due to the limitations, most PIV studies have focused on investigating velocity in a single plane in a partial field of view of the turbulent flow [24]. Complementary to experiments, numerical simulation is an effective alternative for understanding turbulence within ICEs. In the last decade, LES and Direct Numerical Simulation (DNS) has received increasing attention. Unlike Reynolds-averaged Navier Stokes (RANS) simulation, LES simulation can resolve a certain level of turbulence according to its spatial and temporal resolution and capture instantaneous turbulence [2, 18, 28–31], whereas DNS is required to resolve all the scales of turbulence in time and space [32].

One study has utilized DNS to investigate the near-wall thermo-viscous boundary layer structures of a motored engine under engine-like conditions [32]. Following the DNS study, another study has employed a scale-resolved LES and the DNS data [32] to assess velocity and thermal wall models applied to a motored engine during the compression phase under engine-like conditions [31]. It revealed that the near-wall profiles on the piston no longer followed the law of the wall derived from canonical pipe flow. Further, wall functions based on a zero-pressure gradient on the wall and linear-power law led to substantial underprediction of wall heat transfer and overprediction of near-wall velocity.

Due to the complexity of engine flows, engine flow benches have been used to elucidate the physics involved in the process, such as turbulence formation, and to permit controlled variations in the specific flow conditions. Several studies have justified that engine flow benches can be a benchmark to develop and further advance the numerical models [18, 28–30, 33–35]. Among the studies above, one study suggested that the unsteady effects,

such as turbulent fluctuations due to the convergence of the intake flow from two intake ports and jet flapping might affect the stability of the bulk tumble vortex and cause cycle-to-cycle variation.

1.1.2 GDI sprays in either constant-volume chamber or real engines

Apart from the first generation GDI spray swirl-type injector[12, 13], the spray characteristics of GDI multi-hole injectors in either a constant-volume chamber or real DISI engines have been extensively studied [25, 36–42]. However, the multi-hole injectors applied in each study differ in terms of their operating conditions and geometry despite the consistency of the scientific discoveries, such as spray formation and characteristics of different fuels [43, 44] and model developments [45, 46]. This occurrence, with a lack of a detailed and consistent dataset, yields difficulties in validating numerical modelings and experimental approaches. Such difficulties are solved and advanced by the Engine Combustion Network (ECN) focusing on a multi-hole counter-bore injector, "SprayG," in a constant-volume chamber [47]. Researchers in the ECN group provide a wide range of experimental data, such as diffuse back-illumination (DBI) imaging and Mie scattering imaging for the liquid phase and Schlieren imaging for the vapor phase [48–51]. One study focused on the inner-nozzle flow and the plume-to-plume variation near the nozzle using time-resolved x-ray radiography to understand the spray rate-of-momentum effects and compare the rate-of-injection data [50]. Another study utilized DBI measurement for the liquid plume and further applied a three-dimensional tomographic reconstruction of ensemble-average extinction images to gain an insight into the structure and evolution of the multi-plume spray for ECN Spray G injectors with different fuels [48].

The original work from the ECN pertains to a constant-volume chamber under engine-like conditions, limiting the observation and investigation of spray-flow interactions. One study utilized the ECN Spray G injector into a DISI engine under late-injection conditions (Spray G1) [42]. This revealed that the in-cylinder flow is susceptible to spray formation. During injection, spray air entrainment influences the in-cylinder flow, potentially disrupting the tumble flow structure if its intensity is too weak. However, if the structure of the tumble flow is sufficiently strong, it can withstand the influence of the spray injection. Furthermore, by means of spray probability maps assembling and averaging the spray plume with multiple injections, the cycle-to-cycle fluctuations in the liquid spray spatial distribution are affected by the in-cylinder flow. Another study focuses on the spray-flow interaction within a DISI engine under early-injection conditions [25]. Both Spray G2 (flash boiling) and G3 (early injection) are discussed. The global turbulent kinetic energy remains unaffected by the spray after injection close to the ignition although it may experience a transient increase during the injection, indicating a

strong domination of in-cylinder flow velocity and velocity fluctuations. In contrast to late-injection conditions, in which spray formation is stabilized by the higher upward velocities, spray formation under early-injection conditions is highly influenced by the large-scale motion of the in-cylinder flow and engine speed. Additionally, the study suggests that wall wetting may impact emission and performance due to the occurrence of wall wetting on the spark plug.

The Spray G injector has not only been investigated experimentally but also been examined numerically. Several studies have developed a CFD framework using RANS simulation under the Eulerian-Lagrangian framework for Spray G under several engine-like conditions within a constant-volume chamber [52–54]. One study using RANS simulation investigated spray formation and spray-flow interaction within a DISI engine under early-injection conditions (Spray G3) [55]. It proposed a post-process scheme to obtain the numerical Mie scattering signal consistent with the experiment, as the numerical liquid spray penetration is often calculated based on the mass fraction of the liquid droplets. Furthermore, plume-to-plume variation was observed, with the spray plumes at the central tumble plane exhibiting the most extended penetration. The intake flow significantly impacted spray formation, and the intake valve-induced vortex enhanced air entrainment to the spray plume.

Most of the research above focused on RANS simulations, while just a few applied LES [1, 3, 56], as most of the models for Lagrangian particles are based on RANS simulations. Moreover, investigating spray-flow interaction, particularly in GDI engines, using RANS neglected the critical aspect of cycle-to-cycle variations. It is evident and widely accepted that the in-cylinder turbulent flow pattern highly affects the flame propagation in GDI engines. Although the global turbulent kinetic energy returns to its initial values before ignition, the local pattern of in-cylinder flow varied during the spray injection duration [25, 57].

1.1.3 Spray-wall impingement in either constant-volume chambers or real engines

By injecting fuel directly into the combustion chamber, GDI engines can facilitate a high thermal efficiency with a high compression ratio and suppression of the presence of knock due to charge cooling compared with PFI engines [8, 11]. However, as the injection occurs within the combustion chamber, the fuel film deposits on the walls, such as the piston, liner wall, intake valves, and even spark plug, are likely to occur, especially during cold-start conditions. Wall wetting in ICEs can lead to soot formation induced by the high-soot events and, consequently, impacts emissions [58–61]. Several studies have been devoted to investigating the fuel film formation process under engine-relevant

conditions using different measurements, such as laser-induced fluorescence (LIF) and low-coherence interferometry (LCI) [58–64].

Wall film thickness measurements using LIF for GDI engines require a fluorescent tracer, such as toluene [62] and 3-pentanone [65] added to iso-octane. One study has investigated wall film thickness within a motored, optically accessible DISI engine using LIF measurements with two different fluorescent tracers (toluene and 3-pentanone) [66]. It revealed that both tracers are sensitive to temperature, but toluene has a much stronger LIF signal than 3-pentanone. Another study has examined the wall film thickness of a surrogate gasoline (30% toluene and 70% iso-octane) in a constant-volume chamber using ultraviolet (UV) absorption [64]. Using UV absorption, the wall film signal is relatively less sensitive to temperature, but the interference of vapor on the liquid film is significant. These techniques are sensitive and dependent on temperature and oxygen concentration. On the other hand, two studies have investigated wall film thickness of E10 gasoline surrogate fuel (PACE20) in a constant-volume chamber under cold and hot conditions where the fuel, wall, and ambient temperature are 20 °C and 90°C, respectively, using LCI [61, 63]. It revealed that LCI can mitigate the problems above with limited dependency on temperature and immunity of the calibration from vapor interference. Furthermore, thicker fuel films were observed under cold conditions than hot ones.

Spray impingement and wall film development have also been studied numerically, although the effort to improve the numerical predictions is ongoing. Several studies have focused on developing predictive spray-wall interaction models under the Eulerian-Lagrangian framework [67–71]. Bai et al. [68] developed a spray-wall interaction regime, encompassing droplets stick, rebound, and splash, based on the droplets' local Weber number (*We*) derived from experimental data on single water droplets impacting on a dry or wet wall, whereas Stanton and Rutland [67] has utilized the droplets' frequency affecting on the wall to define the threshold of the splash regime. Not only the spray-wall interaction regimes are needed to be defined, but the splash mass and splash velocity are also required. These imperative parameters, however, strongly rely on empirical observations [72, 73]. One study has evaluated multiple spray-wall interaction models, Bai-Gosman [68], Stanton-Rutland [67] and O'Rourke-Amsden [70], on GDI sprays [74]. It revealed that all models have advantages and disadvantages in capturing film thickness, rebound droplet size, and height due to different models' assumptions.

The above provides a summary of the current state and the challenges for the spray-wall impingement and fuel film deposition experimentally and numerically. The numerical studies have been focused on the model development and evaluation. The test case pertains to simple geometry (constant-volume chamber) with a simplified simulation domain, solely investigating the single plume. Whole domain evaluation and its application into an engine-like geometry have not yet been explored and discussed.

1.2 Objectives and structure of this thesis

The above literature survey covers both experimental and numerical research on spray-wall-flow interaction from a constant-volume chamber toward real engine applications and from PFI engines toward GDI engines. There is still a gap in combining all the knowledge above and applying it to a GDI engine. The study will focus on developing a suite of models under the Eulerian-Lagrangian framework using LES and investigate spray-wall-flow interaction within a GDI engine under early-injection conditions. Conducting an engine study using LES simulation requires multiple engine cycles to obtain sufficient statistics. An engine flow bench is a suitable alternative as it operates under a stationary state, reducing the complexity of engine flow and providing clear conditions during the intake phase. Furthermore, the development of a suite of models for spray-wall-flow interaction will focus on the experiments in a constant-volume chamber from ECN using a multi-hole counter-bore GDI injector, "Spray G." Both free spray and spray-wall impingement will be taken into account.

The objectives of this Ph.D. study are listed in the following:

1. Develop a suite of models under the Eulerian-Lagrangian framework for spray-wall-flow interaction for GDI engines.

2. Spray morphology within a constant-volume chamber:
   - Investigate the characteristics of GDI sprays with a multi-hole counter-bore configuration.
   - Examine the spray formation and the air-fuel mixture under early- (boiling and non-boiling regimes) and late-injection conditions.
   - Understand the air-fuel mixture with different fuels (high-volatile and low-volatile fuels).

3. Spray-wall interaction and wall film development in a constant-volume chamber:
   - Investigate the spray-wall interaction process and spray cooling.
   - The effects of spray impingement on the wall temperature and wall film thickness.

4. In-cylinder flow within an GDI engine flow bench:
   - Gain insights into the coherent turbulence structure by studying the Reynolds stress tensor on both the valve and central tumble planes.

- Identify the near-wall non-equilibrium effects governing intake flow turbulence close to the intake valve and the impingement region close to the liner wall.

5. Spray-wall-flow interaction within an GDI engine flow bench:
   - Gain insight into the influence of the intake flow on spray formation.
   - Investigate the impact of the evaporation effect and local in-cylinder vortex on the spray pattern.
   - Explore the convection effect on the wall film under different operating conditions with varying mass flow rates.
   - Examine the influence of the spray-induced turbulence on the global turbulence kinetic energy during the injection.

1.2.1 Target GDI engine flow bench and hole-type injector

The engine air flow bench in this thesis is based on a single-cylinder spray-guided DISI optical engine built at the Technical University Darmstadt and designed by AVL [20–25, 51]. The engine has a pent-roof cylinder head equipped with twin cams and overhead valves. It has a dual-port system to produce a tumble motion within the combustion chamber. Furthermore, it is a square engine where the bore and the stroke are the same sizes: 86 mm. The compression ratio is 8.7. The research behind this engine aims to provide an insight into engine phenomena using optical diagnostics such as PIV [22, 23, 25]. Thus, it is equipped with an optical accessible window with a height of 55 mm on the liner wall.

In contrast to the original motored engine, the air flow bench was set up with its piston removed, an optical plate placed on the bottom attached to the cylinder, and an outlet channel, along with fixed intake valves to simulate the intake flow. The valve position was set to 9.21 mm, which is the valve lift of the motored engine at −270°CA (degrees crank-angle after combustion top dead center). Figure 1.4 shows the configuration of the engine flow bench. It was designed to measure the intake jet under various prescribed mass flow rates (100%, 75%, and 50%). Table 1.1 summarizes the relevant boundary conditions of the engine flow bench.

Apart from the target engine flow bench, the GDI spray injector in this thesis is a hole-type injector provided by ECN and manufactured by Delphi Technologies. This injector features an eight-hole and counter-bore configuration, facilitating the strategy of low-needle lift and further causing the compressible effects to enhance the spray atomization [4, 75]. This injector is able to operate at an injection pressure of up to 200 bar. Due to the dedication of researchers all around the world, a wide range of data, from

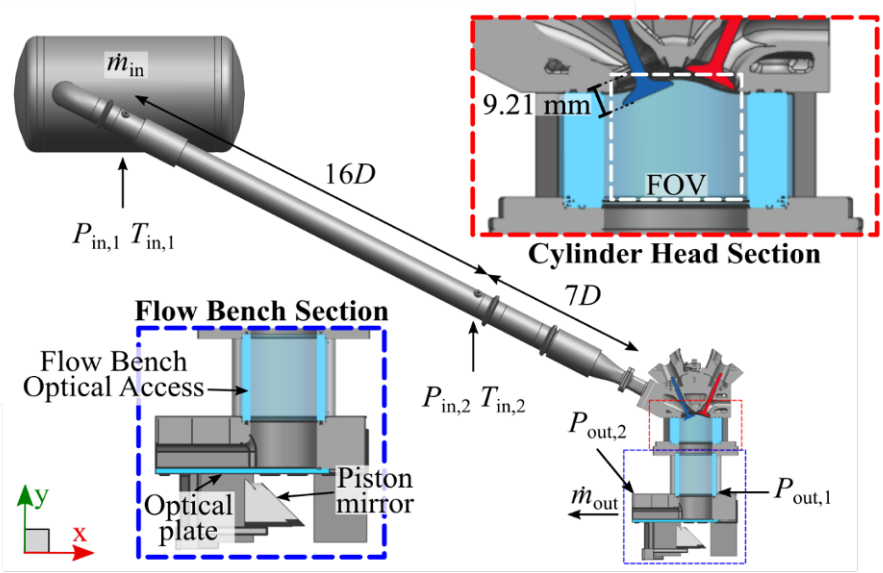

Figure 1.4: Configuration of a GDI engine flow bench [24]

Table 1.1: Experimental parameters of the operating conditions

Condition	100%	75%	50%	0%
Inlet temperature ($T_{in,2}$)(°C)	22.7	23.2	23.2	21.9
Inlet pressure ($P_{in,2}$)(bar)	1.0	1.006	1.0	1.0
Outlet pressure ($P_{out,2}$)(bar)	0.998	1.006	1.007	1.0
Mass flow rate ($\dot{m}_{in}$)(kg/h)	94.10	70.63	47.09	0.517
Reynolds number	32,400	24,300	16,200	178

inner-nozzle and near-nozzle spray characteristics to large-scale free spray evolution, can be acquired from ECN [47–51]. The dimension and geometry of the Spray G injector are shown in Figure 1.5.

1.2.2 The structure of this thesis

Based on the literature review, the scientific objectives of this thesis have been conducted and introduced. The structure of the remaining thesis is shown as the following: numerical methodology, including the governing equations of the Eulerian and Lagrangian fields, the closure model for sub-grid viscosity (μ_t) for LES and the relevant models for spray

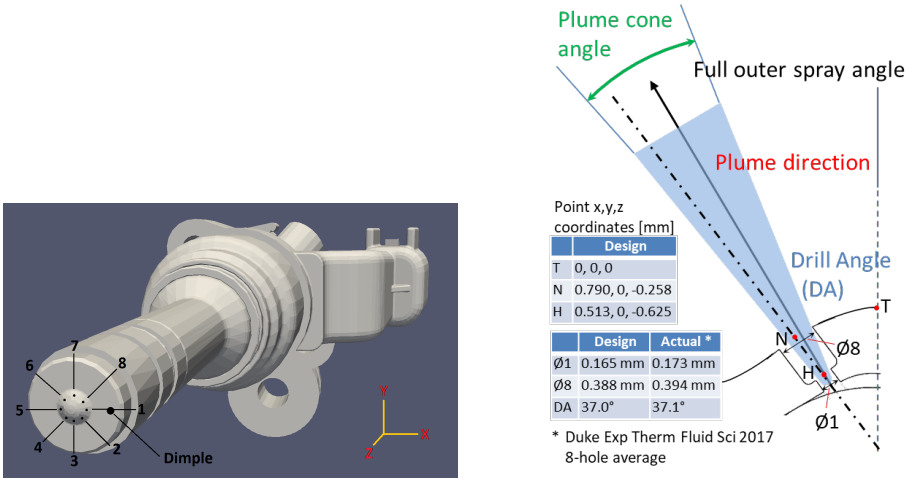

Figure 1.5: The dimension and geometry of the Spray G injector [76]

simulations, are to be introduced in Chapter 2. Following the objectives above, Chapter 3 will first introduce the numerical and experimental setup of free spray in a constant-volume chamber and investigate the spray formation under several engine-relevant conditions. Furthermore, the spray-wall interaction will be discussed in Chapter 4. The numerical and experimental setup of the GDI engine flow bench and investigation of the in-cylinder flow turbulence and its near-wall effects are presented in Chapter 5. Finally, Chapter 6 performs the investigation of spray-wall-flow interaction in a GDI engine flow bench.

2 Numerical methodologies

The multi-phase flow simulations in this study are conducted using Large Eddy Simulation (LES) under the Eulerian-Lagrangian framework. All the simulation is based on a developed code library using an open-source CFD software, OpenFOAM v2012. Under the Eulerian-Lagrangian framework, the liquid fuel represents and is modeled as stochastic Lagrangian parcels, whereas the Eulerian domain directly solves the gaseous field, as shown in Figure 2.1. This chapter will start with a description of the numerical approaches of the gas phase, including governing equations, and sub-grid viscosity models for LES. Unlike RANS simulation, LES is more demanding in terms of temporal and spatial resolution. The mesh quality plays a role in the resolution of the turbulence. Assessment approaches based on Pope [77], will be further introduced and applied in each simulated target. Since the liquid fuel is tracked inside the stochastic Lagrangian parcels, the exchange of momentum, heat, and mass between the liquid and gas phases needs to be modeled. They are described as source terms and solved using equations of the mass, momentum, energy, and species transport conservation in the gas phase. The governing equations of the liquid phase and the corresponding models, including drag, evaporation, heat transfer, and breakup models, will be illustrated in the subsequent subsections.

2.1 Gas Phase

2.1.1 Governing equations

The gaseous turbulent flow in the Eulerian-Lagrangian approach is resolved using equations for the compressible mass, species mass fractions, momentum, and energy in the Eulerian domain.

Mass conservation

The conservation of mass in the Eulerian domain is:

$$\frac{\partial \rho}{\partial t} + \frac{\partial \rho u_i}{\partial x_i} = S_\rho, \tag{2.1}$$

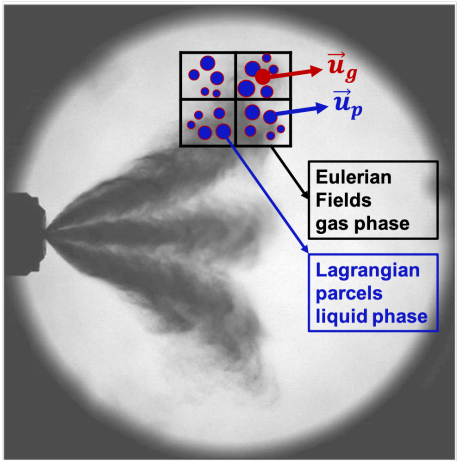

Figure 2.1: Schematic simulation under Eulerian-Lagrangian framework for spray simulation (Source background experimental DBI extinction image from Weiss et al. [51])

where ρ and u_i denotes the density, and velocity in the direction i, respctively. S_ρ is the source term of the fuel phase change (evaporation or condensation) from the Lagrangian field.

Mass conservation for each species

Mass transportation equation for each species in mass fraction exhibits:

$$\frac{\partial \rho Y_k}{\partial t} + \frac{\partial (\rho (u_i + V_{k,i}) Y_k)}{\partial x_i} = S_{Y_k} \tag{2.2}$$

where Y_k and S_{Y_k} represent the mass fraction and phase change of each species ($k = 1, N$) In this study, there are no reactions involved. $V_{k,i}$ is the diffusion velocity of each species. The sum of the diffusion velocity ($\sum_{k=1}^{N} Y_k V_{k,i} = 0$) is conserved and, therefore, it is absent in Equation (2.1). The Hirschfelder and Curtiss approximation is employed to obtain the diffusion velocity of each species, which can be found in a work by Poinsot et al. [78]. It reads:

$$V_{k,i} = -D_{k,i} \frac{\nabla Y_k}{Y_k} \tag{2.3}$$

Where $D_{k,i}$ is the diffusion coefficient.

Momentum conservation

The momentum conservation equation is given by:

$$\frac{\partial \rho u_i}{\partial t} + \frac{\partial (\rho u_i u_j)}{\partial x_j} = \frac{\partial \tau_{ij}}{\partial x_i} - \frac{\partial p}{\partial x_i} + \rho g_i + S_{u_i} \tag{2.4}$$

where p and τ_{ij} are the pressure and stress tensor, respectively. g_i represent the gravitational acceleration in the direction i. S_{u_i} is the momentum change of liquid fuel. Further, the stress tensor ($\tau_{ij} = 2\mu S_{ij}$) is linearly proportional to the rate of strain ($S_{ij} = \frac{1}{2}(\frac{\partial u_i}{\partial x_j} + \frac{\partial u_j}{\partial x_i})$).

Energy conservation

Energy appears in various forms, total internal energy (e), total enthalpy (h_t), sensible enthalpy(h_s) or even temperature (T), with their corresponding conservation equations. The study utilizes the total enthalpy ($h_t = h + \frac{1}{2}u_i u_i$) for multi-phase flow simulation, and h is the specific enthalpy ($h = h_s + \sum_{k=1}^{N} \Delta h^0_{f,k} Y_k$).

The conservation equation appears as follows:

$$\frac{\partial \rho h_t}{\partial t} + \frac{\partial (\rho u_i h_t)}{\partial x_i} = \frac{\partial p}{\partial t} - \frac{\partial q_i}{\partial t} + \tau_{ij}\frac{\partial u_i}{\partial x_j} + \rho \sum_{k=1}^{N} Y_k f_{k,i}(u_i + V_{k,i}) + S_{h_t} \tag{2.5}$$

where q_i is the energy flux, comprising a heat diffusion term expressed according to Fourier's Law ($\lambda \frac{\partial T}{\partial x_i}$) and the diffusion of different species ($\rho \sum_{k=1}^{N} h_k Y_K V_{k,i}$), whereas S_{h_t} is the enthalpy change of the liquid phase. $\rho \sum_{k=1}^{N} Y_k f_{k,i}(u_i + V_{k,i})$ is the energy produced by the volume forces f_k on species k.

To acquire the specific enthalpy (h), the sensible enthalpy ($h_s = \sum_{k=1}^{N} Y_k \int_{T_0}^{T} c_{p,k} dT$) and enthalpy formation for each specie ($h^0_{f,k}$) are required. In this study, seven-term molar-based NASA polynomial correlations are used and given below:

$$\frac{c_p^m(T)}{R} = a_0 + a_1 T + a_2 T^2 + a_3 T^3 + a_4 T^4 \tag{2.6}$$

$$\frac{h^m(T)}{RT} = a_0 + \frac{a_1}{2}T + \frac{a_2}{3}T^2 + \frac{a_3}{4}T^3 + \frac{a_4}{5}T^4 + \frac{a_5}{T} \tag{2.7}$$

where $R = 8.314 J/K/mol$ is the universal gas constant. The polynomial coefficient (a_i) of each specie in this study are shown in these two resources [79, 80]. The molar-based thermodynamic properties can be converted to mass-based ones by divided molecular mass (M_k), e.g. $c_{p,k} = c^m_{p,k}/M_k$. Finally, the ideal gas law is used to close the equations.

2.1.2 Turbulence and closure models for the governing equations

In this thesis, Large Eddy Simulation (LES) is utilized to resolve the turbulence in an instantaneous manner. LES is proposed with the notion that due to the multi scales of turbulence, the large scale unsteady turbulent motion is resolved and is directly represented, whereas the universal small scale turbulence is modeled. It can efficiently reduce the computational expense compared to DNS. Furthermore, LES can yield more accurate results compared with RANS if the resolution of the turbulence is high and only the small-scale turbulence structure, which is regarded to be homogeneous and isotropic, needs to be modeled. To achieve and facilitate the concept, Leonard [81] has introduced the scale-separating filtering equations with an operator $\widehat{(.)}$ and the filtered field $\widehat{\Phi}(x_i)$ is defined as:

$$\widehat{\Phi}(x_i) = \int_{-\infty}^{\infty} \Phi(x_i, r_j) G(x_i, r_j) dr_j \tag{2.8}$$

where $G(x_i, r_j)$ is the filter kernel covering the region with radius (r_j) and center point (x_i).

As the density varies within the turbulent flow, a density-weighed filter, Favre filter, is required under the LES framework. It is applied with an operator $\widetilde{(.)}$ and is defined as:

$$\widetilde{\Phi} = \frac{\widehat{\rho\Phi}}{\widehat{\rho}} \tag{2.9}$$

After introducing the filtering scheme for LES, the governing equations of mass, momentum, energy, and species transportation, Equation (2.1) to (2.5), need to be altered and appear as forms:

$$\frac{\partial \widehat{\rho}}{\partial t} + \frac{\partial \widehat{\rho}\widetilde{u_i}}{\partial x_i} = \widehat{S}_{\rho}, \tag{2.10}$$

$$\frac{\partial \widehat{\rho}\widetilde{Y_k}}{\partial t} + \frac{\partial (\widehat{\rho}\widetilde{u_i}\widetilde{Y_k})}{\partial x_i} = \frac{\partial}{\partial x_i}[\widehat{\rho}(\widetilde{u_i}\widetilde{Y_k} - \widetilde{u_i Y_k})] + \widehat{\rho}\widetilde{D}\frac{\partial^2 \widetilde{Y_k}}{\partial x_i^2} + \widehat{S}_{Y_k} \tag{2.11}$$

$$\frac{\partial \widehat{\rho}\widetilde{u_i}}{\partial t} + \frac{\partial (\widehat{\rho}\widetilde{u_i}\widetilde{u_j})}{\partial x_i} = \frac{\partial}{\partial x_i}[\widehat{\rho}(\widetilde{u_i}\widetilde{u_j} - \widetilde{u_i u_j})] + \frac{\widehat{\tau}_{ij}}{\partial x_i} - \frac{\partial \widehat{p}}{\partial x_i} + \widehat{S}_{u_i} \tag{2.12}$$

$$\frac{\partial \widehat{\rho}\widetilde{h_t}}{\partial t} + \frac{\partial (\widehat{\rho}\widetilde{u_i}\widetilde{h_t})}{\partial x_i} = \frac{\partial \widehat{p}}{\partial t} + \frac{\partial}{\partial x_i}[\widehat{\rho}(\widetilde{u_i}\widetilde{h_s} - \widetilde{u_i h_s}) + \widehat{\mu}\frac{\partial \widetilde{h_s}}{\partial x_i}] + \widehat{S}_{h_t} \tag{2.13}$$

The terms $\widehat{\rho}(\widetilde{u_i}\widetilde{u_j} - \widetilde{u_i u_j})$, $\widehat{\rho}(\widetilde{u_i}\widetilde{Y_k} - \widetilde{u_i Y_k})$, and $\widehat{\rho}(\widetilde{u_i}\widetilde{h_s} - \widetilde{u_i h_s})$ within Equations (2.10), (2.11) and (2.13) need to be closed by introducing an eddy viscosity model:

$$\widehat{\rho}(\widetilde{u_i}\widetilde{u_j} - \widetilde{u_i u_j}) = 2\mu_t(\widehat{S}_{ij} - \frac{1}{3}\widehat{S}_{kk}\delta_{ij}) \tag{2.14}$$

$$\widehat{\rho}(\widetilde{u_i}\widetilde{Y_k} - \widetilde{u_i Y_k}) = \frac{\mu_t}{Sc_t}\frac{\partial \widehat{Y_k}}{\partial x_i} \tag{2.15}$$

$$\widehat{\rho}(\widetilde{u_i}\widetilde{h_s} - \widetilde{u_i h_s}) = \frac{\mu_t c_p}{Pr_t}\frac{\partial \widehat{T}}{\partial x_i} \tag{2.16}$$

$\widehat{S}_{ij}$ is the resolved strain rate tensor, $\widehat{S}_{ij} = 0.5(\partial\widetilde{u_i}/\partial x_j + \partial\widetilde{u}_j/\partial x_i)$, and $\widehat{S}_{kk}$ is the rate of compression scalar, $\widehat{S}_{kk} = \partial\widetilde{u_k}/\partial x_k$. Pr_t and Sc_t refer to modeled Prandtl and Schmidt numbers, respectively. The sub-grid eddy viscosity μ_t is acquired from the static sigma model [82]. This model is suitable for the wall-confined domain as it can distinguish between the laminar and turbulent flow and reproduces the correct cubic behavior of the sub-grid scale viscosity when approaching solid walls. Moreover, the sub-grid viscosity vanishes for pure shear and solid rotation. The sub-grid viscosity of the sigma model appears as:

$$\mu_t = \widehat{\rho}(C_\sigma\Delta)^2\frac{\sigma_3(\sigma_1 - \sigma_2)(\sigma_2 - \sigma_3)}{\sigma_1^2}, \tag{2.17}$$

where C_σ is the model constant and is equal to 1.5. σ_i is the singular value of the resolved velocity gradient tensor, which is $\widehat{g}_{ij} = \frac{\partial\widetilde{u_i}}{\partial x_j}$. The sub-grid viscosity (μ_t) remains positive as the σ_i are all positive and follow the corresponding order $\sigma_1 \geq \sigma_2 \geq \sigma_3 \geq 0$.

2.1.3 Assessment of Large Eddy Simulation resolution quality

As mentioned previously, Large Eddy Simulation (LES) can have high accuracy only if the larger scale turbulence is properly resolved. Therefore, the mesh quality is imperative as it affects the resolution of the turbulence. Celik et al. [83] developed three different indexes based on the principle of the turbulence-resolved scale from Pope [77]. According to Celik et al. [83], a sufficient Large Eddy Simulation (LES) is suggested to contain 75 to 85 % of the kinetic energy. The three indexes, which are based on the turbulent viscosity, dissipation, and kinetic energy, thus focus on different examined parameters depending on the type of the sub-grid model used in LES. The study employs the sigma model developed by Nicoud et al. [82]. This is an algebraic eddy viscosity model in which the eddy viscosity ν_t is directly solved, unlike the one-equation model [84]. Therefore, the corresponding index($IQ_{LES,\nu}$) is written as:

$$IQ_{LES,\nu} = \frac{1}{1 + \alpha_\nu(\frac{\nu_{t,eff}}{\nu})^n}, \tag{2.18}$$

where α_v is a constant with a value of 0.05 and $n = 0.53$. The effective viscosity ($\nu_{t,eff}$) is the sum of the molecular viscosity (ν) and the eddy viscosity (ν_t).

The assessment of the turbulence resolution will be conducted in each case, constant volume spray chamber, spray impingement chamber, and GDI engine flow bench, and shown in the corresponding sections.

2.2 Liquid Phase

2.2.1 Governing equations

Under the Eulerian-Lagrangian framework, the liquid fuel represents and is modeled as stochastic Lagrangian parcels. The Lagrangian domain behaves discretely from the Eulerian domain and only provides the exchange of momentum, heat, and mass which appear as a source term in the gas phase, as shown from equation (2.10) to (2.13). Furthermore, these exchanges with gas are solved by either empirical or analytical models. The governing equations of the liquid phase exhibit:

$$\widehat{S}_\rho = -\frac{1}{\Delta V}\sum_{i=1}^{N}\frac{\mathrm{d}m_p}{\mathrm{d}t} \tag{2.19}$$

$$\widehat{S}_{Y_k} = -\frac{1}{\Delta V}\sum_{i=1}^{N}\frac{\mathrm{d}m_{p_k}}{\mathrm{d}t} \tag{2.20}$$

$$\widehat{S}_u = -\frac{1}{\Delta V}\sum_{i=1}^{N}\frac{\mathrm{d}(m_p u_p)}{\mathrm{d}t} \tag{2.21}$$

$$\widehat{S}_{h_t} = -\frac{1}{\Delta V}\sum_{i=1}^{N}\frac{\mathrm{d}(c_p m_p T_p)}{\mathrm{d}t} \tag{2.22}$$

where ΔV and N represent the volume of the Eulerian cell where the Lagrangian parcels dwell and the total number of the Lagrangian parcels within the Eulerian cell, respectively.

The velocity of liquid droplets tracked statistically in each Lagrangian parcel is solved as follows:

$$\frac{\mathrm{d}u_p}{\mathrm{d}t} = \frac{3}{4}\mathrm{C_D}Re_p\frac{\mu_g}{\rho_p d^2}u_{rel} + g, \tag{2.23}$$

where $(.)_p$ denotes the properties of the liquid particles, while $(.)_g$ represents gas properties. u_{rel} is the relative velocity from the ambient gas and a particle, $u_{rel} = u_g - u_p$. u_g is the resolved gas velocity ($\widetilde{u}$) within the cell where the Lagrangian parcels reside. g and d

are the gravitational acceleration and diameter of liquid particles. The drag coefficient (C_D) needs to be acquired by drag models.

The rate of mass transfer to the drop surface is written as follows:

$$\frac{dm_p}{dt} = \pi d D \rho Sh_p \ln(1.0 + BM), \tag{2.24}$$

where Sh_p is the Sherwood number from the liquid particle, and the Spalding mass transfer number (BM) is defined as

$$BM = \frac{Y_s - Y_G}{1.0 - Y_s}, \tag{2.25}$$

where Y_s refers to the fuel vapor mass fraction on the particle surface, and Y_G is the vapor mass fraction away from the particle surface.

The rate of heat transfer to the drop surface is written as follows:

$$mc_p \frac{dT_p}{dt} = h_c A_p (T_g - T_p) - \frac{dm}{dt} h_v, \tag{2.26}$$

where A_p is the surface area of each Lagrangian parcel, $h_c = \frac{Nu_p k_g}{d}$ is the heat transfer coefficient, and h_v denotes the heat of vaporization.

To close the Lagrangian parcel governing equations (2.23), (2.24), and (2.26), the drag coefficient (C_D), Sherwood number(Sh_p), and Nusselt number(Nu_p) need to be specified by either models or correlations. All the relevant models will be introduced in the subsequent sections.

2.2.2 Distorted droplet models for momentum, heat, and mass exchange

Several studies have developed models based on empirical research or DNS simulation data to improve the standard drag model accounting for the effect of droplet non-sphericity [85–88]. The most popular model is the distorted sphere drag model from Liu et al. [85]. It provides a non-dimensional droplet distortion factor (y) calculated dynamically using the TAB breakup model from O'Rourke and Amsden [89] to correct the sphere drag coefficient [90].

The correlation of the sphere drag coefficient is defined as

$$C_{D,\text{sphere}} = \begin{cases} \frac{24}{Re_p}(1.0 + \frac{1}{6}Re_p^{\frac{2}{3}}), & Re \le 1000 \\ 0.424, & Re > 1000 \end{cases}, \tag{2.27}$$

The correction formula for distorted droplets reads:

$$C_D = C_{D,sphere}(1 + 2.632y), 0 \leq y \leq 1 \tag{2.28}$$

However, this model only considers the distortion for oblate spheroids. The deformation in the form of prolate spheroids, which often occurs during droplet oscillation and deformation, is neglected. Motivated by this limitation of the currently available approach, the following is to present the models considering droplet distortion effects on drag, evaporation, and heat transfer.

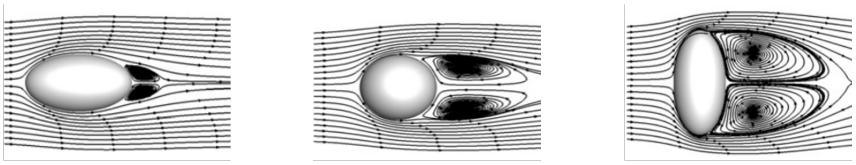

(a) Prolate particle $y = -1$ (b) Sphere particle $y = 0$ (c) Oblate particle $y = 1$

Figure 2.2: The deformation of liquid droplets and the corresponding distortion factor (y). Reprinted with permission from a study by Richter and Nikrityuk [91]

The distortion model utilized in this study is according to research by Richter and Nikrityuk [91]. It takes into account the deformation of prolate spheroids modeled using the TAB breakup model, as shown in Figure 2.2. The study employed a DNS simulation to derive a regression model that is capable of predicting 99.8 % of the variance in the drag coefficient and appears as:

$$\frac{C_D}{C_{D,sphere}} = \frac{0.21 + \frac{20}{Re_p}(\frac{l}{d})^{0.58} + \frac{6.9}{\sqrt{Re_p}}(\frac{l}{d})^{-1.4}}{0.21 + \frac{20}{Re_p} + \frac{6.9}{\sqrt{Re_p}}}, \tag{2.29}$$

where l denotes the spanwise length of the droplets and appears in the form:

$$l = d(1 - C_b y), \tag{2.30}$$

where C_b is a model constant with a value equal to 0.5.

As the oscillation and deformation of the liquid droplets occur, the surface area is no longer equal to the sphere surface. This phenomenon affects the Nusselt number (Nu_p). Richter and Nikrityuk [91] also provided a correlation by identifying the sphericity (ϕ) and the crosswise sphericity ($\phi_\perp$), shown as:

$$\frac{Nu_p}{Nu_{p,\text{sphere}}} = \frac{1.76 + 0.55\phi Pr_p^{\frac{1}{3}} Re_p^{\frac{1}{2}} \phi_\perp^{0.075} + 0.014 Pr_p^{\frac{1}{3}} Re_p^{\frac{2}{3}} (\frac{\phi}{\phi_\perp})^{7.2}}{1.76 + 0.55 Pr_p^{\frac{1}{3}} Re_p^{\frac{1}{2}} + 0.014 Pr_p^{\frac{1}{3}} Re_p^{\frac{2}{3}}}, \tag{2.31}$$

where the the sphericity (ϕ) and the crosswise sphericity ($\phi_\perp$) are defined as:

$$\phi = \frac{4\pi r_p^2}{\text{SrfC}_p}, \tag{2.32}$$

$$\phi_\perp = (\frac{r_p}{H})^2, \tag{2.33}$$

In equations (2.32) and (2.33), H and SrfC_p are half length of the crosswise axis relative to the flow direction of the droplet and the surface area of the droplet, respectively. These two parameters exhibit:

$$H = \sqrt{\frac{r_d^3}{r(1 - C_b y)}}, \tag{2.34}$$

where r is the radius of the droplet.

$$\text{SrfC}_p = \begin{cases} 2\pi H^2 (1 + \frac{1-e^2}{e} tanh^{-1}(e)), & y \geq 0 \\ 2\pi H^2 (1 + \frac{r(1-C_b y)}{He} sinh^{-1}(e)), & y < 0 \end{cases}, \tag{2.35}$$

with the eccentricity e defined as

$$e = \sqrt{1 - (\frac{\min(H, 0.5l)}{\max(H, 0.5l)})^2}, \tag{2.36}$$

2.2.3 Phase-change model

The phase-change model is imperative for the evaporation of liquid fuel and further exchanging the fuel mass from the Lagrangian domain to the Eulerian domain. Phase change for the liquid fuel can be categorized as surface evaporation and boiling. The former indicates that the liquid fuel does not fall under the superheated regime where the evaporation of the liquid fuel occurs from within as the vapor bubble grows inside the liquid droplets and further causes bubble nucleation, growth, and break up. However, GDI engines have wide-range operating conditions, and often under the cold start and part load conditions, the in-cylinder pressure may be lower than 1 bar and further leads the high-pressure liquid fuel ejected from the injector to the superheated regime.

To account for both evaporation conditions, this thesis proposes a hybrid method coupling a non-equilibrium evaporation model [92] and a boiling model [93]. The criteria

to switch both models is based on the weight of local ambient pressure to the vapor pressure of the liquid fuel, as shown in Figure 2.3.

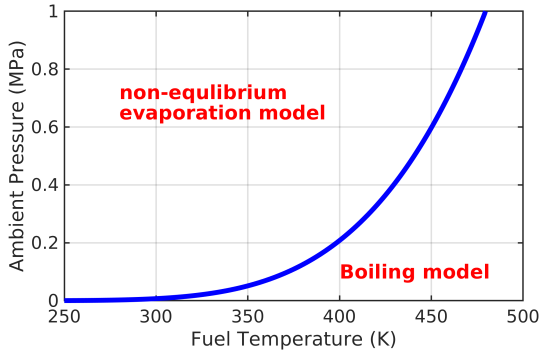

Figure 2.3: Example of the hybrid phase-change model based on the vapor pressure curve of iso-octane [94]

Non-equilibrium evaporation model

Under the non-equilibrium evaporation model, the evaporation only takes place on the surface of the droplet, assuming that the droplets are spherically symmetric and that the temperature at the droplet surface is continuous. Unlike the standard model, the non-equilibrium evaporation model does not assume that the droplet surface is in thermodynamic equilibrium, in which case the mole fraction of fuel vapor can be obtained in relation to the saturated pressure using the Clausius-Clapeyron equation.The vapor mole fraction in this non-equilibrium evaporation model reads:

$$X_{s,\mathrm{neq}} = X_{s,\mathrm{eq}} - (\frac{L_K}{D/2})\beta, \tag{2.37}$$

where $X_{s,\mathrm{eq}}$ is the equilibrium vapor mole fraction and can be obtained by the Clausius-Clapeyron equation. L_K is the Knudsen layer thickness.

$$L_K = \frac{\mu\sqrt{2\pi T_p \overline{R}/W_v}}{Sc_p p}, \tag{2.38}$$

where $\overline{R}$, T_p, and p are the gas constant, droplet temperature, and gas pressure, respectively. The non-dimensional evaporation parameter, β, is given by

$$\beta = -(\frac{3Pr_p\tau_p}{2})\frac{\dot{m}_p}{m_p}, \tag{2.39}$$

where τ_d is the particle time constant for the Stokes flow and can be defined as

$$\tau_p = \rho_p d^2/(18\mu), \tag{2.40}$$

Equation (2.37) can be further manipulated to mass fraction to calculate the Spalding mass transfer number (BM) in equation (2.25).

A solution to Lagrangian grid dependency is also applied in this evaporation model [95]. Hinrichs et al. [95] investigated droplet evaporation under both non-convective and convective conditions. The study shows that if the ratio of the Lagrangian droplet diameter to the grid size is less than 10, it will yield over-evaporated results. This observation agrees well with another study on a swirling combustor using DNS simulation by Luo et al. [96]. To mitigate this phenomenon, Hinrichs et al. proposed a correction in equation (2.24), and the modified mass rate exchange equation reads:

$$\frac{\mathrm{d}m_p}{\mathrm{d}t} = \pi d D \rho Sh_p \ln(1.0 + BM)\frac{(\Delta + r)}{\Delta}, \tag{2.41}$$

where Δ is the grid size.

The factor goes to unity when the droplet size is much smaller than the grid size ($r << \Delta$). By contrast, it becomes larger than unity to compensate for the liquid vaporization when the droplet size is much bigger than the grid size ($r >> \Delta$).

Boiling model

When the ambient pressure is lower than the vapor pressure of the liquid fuel, liquid fuel boiling occurs. This thesis applies a boiling model proposed by Zuo et al. [93]. This model considers the evaporation rate, encompassing the superheated evaporation ($\dot{m}_{boiling}$) and the surface evaporation owing to the external heat transfer($\dot{m}_{ext}$). This model has been successfully applied in spray flash boiling with different fuels, such as ammonia, iso-octane, and n-pentane, in either engine or non-engine applications [46, 97, 98].

The rate of mass transfer appears in the form:

$$\frac{\mathrm{d}m_p}{\mathrm{d}t} = \dot{m}_{boiling} + \dot{m}_{ext}, \tag{2.42}$$

where the rate of superheated evaporation ($\dot{m}_{boiling}$) reads:

$$\dot{m}_{boiling} = \pi d^2 \alpha_s \frac{(T_p - T_{boiling})}{h_v}, \tag{2.43}$$

where $T_{boiling}$, h_v, and α_s are the boiling temperature, the heat of vaporization, and the overall heat transfer coefficient, which can be obtained by empirical correlations [45].

$$\alpha_s = \begin{cases} 760(T_p - T_{boiling})^{0.26}, & 0 < T_p - T_{boiling} < 5 \\ 27(T_p - T_{boiling})^{2.33}, & 5 < T_p - T_{boiling} < 25 \\ 13800(T_p - T_{boiling})^{0.39}, & 25 \leq T_p - T_{boiling} \end{cases}, \tag{2.44}$$

Finally, the external heat transfer caused evaporation is expressed as:

$$\dot{m}_{ext} = \pi d \frac{k_g Sh_p}{c_p} \frac{1}{1 + \dot{m}_{boiling}/\dot{m}_{ext}} \ln\left(1 + \left(1 + \frac{\dot{m}_{boiling}}{\dot{m}_{ext}}\right)\left(\frac{h_g - h_s}{h_v}\right)\right), \tag{2.45}$$

where k_g is the thermal conductivity. h_g and h_s are the enthalpy of the surrounding gas and the vapor, respectively.

2.2.4 Secondary breakup model

The breakup model is imperative in spray simulation using the Eulerian-Lagrangian approach. The liquid droplets ejected from the high-pressure injector, such as gasoline spray and diesel spray, contain droplet dynamics that behave in non-equilibrium with the local gas-phase flow. Thus, the droplets, based on their local gas Weber number (We), undergo drop deformation, oscillation, and a variety of breakup events. Such phenomena require a breakup model to reproduce as the droplets are solved and modeled in the form of Lagrangian parcels. Two models are widely accepted and applied extensively in academia and industry. One is the Taylor Analogy Breakup model (TAB) [89], which is built on Taylors's analogy between drop dynamics and a forced spring-mass-damper system [99]. In this model, the drop deformation and oscillation are explicitly modeled, and the drop breakup occurs when the drop distortion pole reaches the drop center. However, several studies have proven that the TAB model tends to yield under-predicted droplet sizes and liquid penetration length [85, 87, 100, 101].

This thesis employs the WAVE breakup model proposed by Patterson and Reitz [102]. Within this model, the breakup mechanism is triggered by the competition between the growth rate and wavelength of Kelvin-Helmholz and Rayleigh-Taylor instability. The essential parameters, B_0, B_1, and C_{rt}, are ad hoc and often appear in different values with different studies about the same application. Thus, the corrections proposed by Nagaoka and Kawamura [103] can be applied to avoid extensive parameter tuning effort, especially for low Weber number conditions. The corrections are calculated based on the local gas Weber number (We) and appear in the form:

$$B_0 = 0.61\left(1 - 1.43\left(\frac{\rho}{\rho_p}\right)^{0.2} \exp\left(-\frac{We}{10}\right)\right), \tag{2.46}$$

$$B_1 = 161.7\sqrt{\frac{\rho}{\rho_p}} \min\left(1, \left(\frac{15}{We}\right)^{0.8}\right), \tag{2.47}$$

$$C_{rt} = \max(0.2, (0.11\sqrt{We}), \tag{2.48}$$

Furthermore, Nagaoka and Kawamura [103] combined the WAVE breakup model and the correlations proposed by Pilch and Erdman [104] to consider the droplet deformation.

2.2.5 Spray-wall interaction model

Since the injection system of SI engines changes from PFI to GDI, the fuel film has become a crucial problem influencing the emission and performance of ICEs. Especially during the cold start condition with a cold cylinder and piston wall, fuel film may develop and consequently cause soot and HC emission. Several studies have been dedicated to the development of a predictive spray-wall impingement model for gasoline sprays based on empirical and analytical studies [67, 68, 70, 71, 105]. Given that various available spray-wall interaction models, all categorize similar regimes of spray-wall interaction, such as absorb, rebound, and splash, and have their upsides and downsides in capturing certain phenomena such as wall film thickness, rebound velocity, and so on [74].

A spray-wall interaction model from Bai et al. [68] is used in this thesis. The spray-wall impingement regimes, as shown in Figure 2.4, are based on the droplets' local Weber number (We) derived from experimental data on single water droplets impacting on a dry or wet wall.

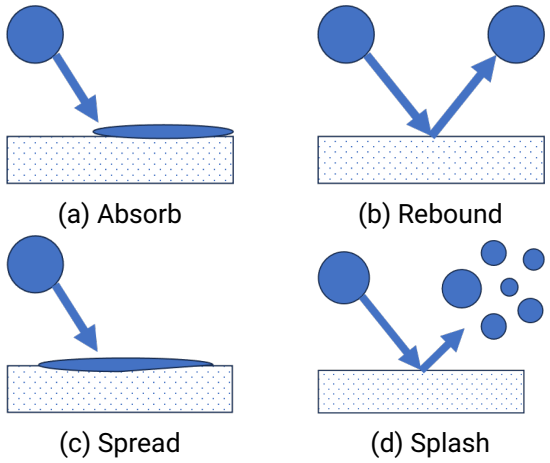

Figure 2.4: Schematic of different droplet wall impingement regimes

The criteria based on the Bai-Gosman model [68] are written as:

$$\text{dry wall} \begin{cases} \text{Absorb} & We < We_c \\ \text{Splash} & We_c < We \end{cases}, \tag{2.49}$$

$$\text{wet wall} \begin{cases} \text{Absorb} & We < 2 \\ \text{Rebound} & 2 < We < 20 \\ \text{Spread} & 20 < We < We_c \\ \text{Splash} & We_c < We \end{cases}, \tag{2.50}$$

where We is the local droplets' liquid Weber number and We_c is the critical Weber number, which is written as:

$$We_c = \begin{cases} 2630La^{-0.183}, & \text{dry wall} \\ 1320La^{-0.183}, & \text{wet wall} \end{cases}, \tag{2.51}$$

where $La = \rho_p \sigma d/\mu$ is the Laplace number.

In the splash onset, the droplet breakup cause the kinetic energy and total droplet mass loss. The splash mass ratios base on its wall condition (dry or wet) are defined as

$$M_{ratio} = \begin{cases} 0.2 + 0.6x, & \text{dry wall} \\ 0.2 + 0.9x, & \text{wet wall} \end{cases}, \tag{2.52}$$

where $x \in [0, 1]$ is an uniform random number.

Finally, the energy conservation for the splash onset is defined as:

$$E_{KS} = E_{KI} + E_{I\sigma} - E_D - E_{S\sigma}, \tag{2.53}$$

where E_{KS} and E_{KI} are the total kinetic energy of residual splashed droplets and of incident droplets. $E_{I\sigma}$ and $E_{S\sigma}$ are the total surface energy of residual splashed droplets and of incident droplets. E_D is the dissipation during the splash.

2.2.6 Injection and droplet distribution models

The droplet distribution model of the Eulerian-Lagrangian approach determines the initial size of the Lagrangian parcels ejected from the injector. Often, researchers and engineers are not aware of the geometry of the inner nozzle and the flow mechanism of the inner-nozzle flow. Moreover, conducting a reliable inner-nozzle flow simulation and near-nozzle measurement is expensive and time-consuming. It is challenging to provide a droplet size distribution. The most popular method, proposed by Reitz and Diwakar [106], assumes that the ejected drops ("blobs") from the injector are equal in size to the nozzle diameter. This is called the blob method. This model has been proven to predict the penetration length correctly in high-pressure sprays [52, 55, 56, 88, 107]. However, it can yield

uncertainties when the targeted spray has a counter-bore inner nozzle, such as ECN Spray G. Several studies devoted attention to the inner-nozzle flow of the ECN Spray G and discovered that the size of the droplets is much smaller than the nozzle diameter, as most primary atomization takes place within the inner nozzle and near-nozzle region. [4, 54, 108, 109]

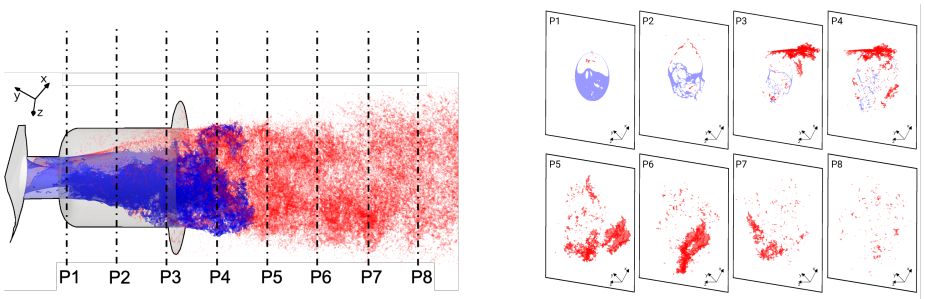

Figure 2.5: Evolution of the droplet dynamics along the injector axis with eight different sections [1, 4].(note: with a uniform distance of 0.2 mm between each section)(Reprinted with permission)

Figure 2.5 shows the evolution of the droplet dynamics along the injector axis acquired from a DNS simulation [4]. The location of P8 is 1 mm from the nozzle exit. The liquid droplets in the blue region are still within the liquid core, whereas the red region indicates that the liquid ligament breaks up and the droplets detach from the liquid core. Evidently, the liquid core only exists up to 0.4 mm from the nozzle exit. The liquid ligament breakup almost completes after P5. Therefore, this study develops a cumulative distribution function (CDF) for the droplet size distribution derived from the DNS data to mitigate the uncertainty yielded by the blob method.

Figure 2.6 shows the droplet size distribution function in section plane P6. It reveals that the droplet size is less than 25 µm, and the majority of the droplet size (40% of the distribution) is approximately between 5 µm to 10 µm. This reaches an agreement with experimental data from ECN [48, 51]. The droplet size distribution function reads:

$$d(x) = 1.569 \exp(1.823x) + 5.185 \cdot 10^{-13} \exp(30.88x), \tag{2.54}$$

where $x \in [0, 1]$ is an uniform random number.

Apart from the droplet distribution function, the ejected velocity, plume direction, and plume cone angle of the Lagrangian parcels ejected from each injector nozzle need to be further defined. The targeted injector, Spray G, features an eight-hole counter-bore configuration. All the injector holes must be considered to capture the interaction between

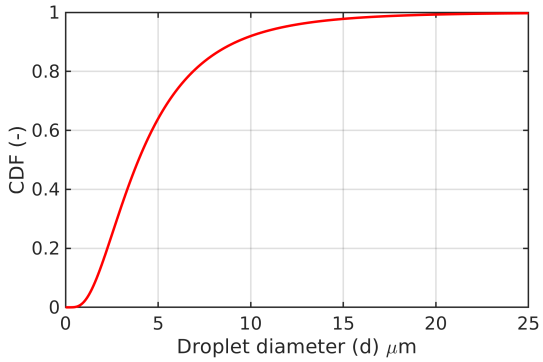

Figure 2.6: Cumulative distribution function (CDF) of the droplet size distribution at section P6, shown in Figure 2.5

each spray plume and in-cylinder flow. The diameter (d_{inj}) of each injector hole is 388 µm, and the drill angle is 37° [50].

By applying a mass flow rate type injection model, the injected velocity can be calculated from the following:

$$U_{p,0} = \dot{m}/(\rho_p C_d A_{inj}), \tag{2.55}$$

where C_d is the discharge coefficient, and $A_{inj} = \frac{\pi d_{inj}^2}{4}$ is the cross-section area of each injector hole.

A previous study by Duke et al. [50] proved that the drill angle and plume direction are not consistent. Each spray plume exhibits a different spray direction and plume cone angle. This is known as "plume-to-plume variation." Furthermore, numerous experimental and numerical studies of the inner-nozzle flow provided different values for the plume direction and cone angle at each injector hole [50, 108, 109]. To reduce the complexity and uncertainty caused by having different values of plume direction and plume cone angle at each injector hole, both are set up as a constant value of 35° and 30°, respectively. All the essential parameters are summarized in Table 2.1.

Finally, the mass flow rate type injection model requires a mass flow rate profile and total injected mass to integrate with time and obtain the instantaneous mass with each time step. In the thesis, even though different fuels, pure iso-octane, E00, and E10 gasoline surrogates, the targeted injector remains. The mass flow profile can be applied to each case; however, in Chapter 4, "Spray-wall interaction and wall film development in a constant-volume chamber," double injection with a dwell time 0.9 ms is set up from the experiment. To clarify all the settings, the necessary information, such as mass flow rate

Table 2.1: Essential parameters of ECN Spray G Injector

Parameters of the injector for simulation input	
Plume cone angle (°)	30
Plume direction (°)	35
Injector diameter (μm)	388
Discharge coefficient (C_d)	0.73

profile, total injected mass, and injection duration, will be introduced in each following chapter.

3 Spray morphology within a constant-volume chamber[1]

This chapter will focus on the GDI spray morphology in a constant-volume chamber provided by ECN. The GDI spray, referred to as “Spray G,” operates inside a hole-type injector featuring an eight-hole counter-bore configuration with injection pressure up to 200 bar. According to available experimental data from ECN [47], the operating conditions of Spray G covered not only early- and late-injection conditions but also the critical conditions within the boiling regime. Furthermore, different fuels are studied, including pure iso-octane and surrogate gasoline fuels, E00 and E10 (PACE20). Pure iso-octane will be the primary fuel throughout the thesis, aligning with available experimental data. As e-fuel and synthesis fuel blend gasoline are the trend for future research, the two multi-component surrogate gasoline fuels are also discussed. E00 is a surrogate gasoline comprised of three different alkanes, n-pentane, iso-octane, and n-undecane [110]. This fuel is designed as a base to investigate ethanol blend gasoline surrogates, such as E20 and E85, whereas the E10 fuel, referred to as “PACE20,” is a 9-component fuel and has been experimentally investigated in spray-wall impingement using LCI [61, 63]and free spray using DBI and 3-D computer tomographic (3-D CT) reconstruction [111, 112]. The mass and volume fractions of each component in these two surrogates are shown in Tables 3.1 and 3.2.

Table 3.1: Volume and mass fraction of liquid E00 surrogate fuel

E00	Volume fraction(%)(-)	Mass fraction(%)(-)
n-pentane	36	33.1904
iso-octane	46	47.1248
n-undecane	18	19.6848

[1]This section is partly taken from a publication by Lien et al. [1], which was accomplished during the work on this thesis. In Ref. [1], I was the first author.

Table 3.2: Volume and mass fraction of liquid E10 surrogate fuel

PACE20	Volume fraction(%)(-)	Mass fraction(%)(-)
ethanol	9.55	10.16
n-pentane	13.95	11.68
cyclopentane	10.50	10.62
1-hexene	5.41	4.91
n-heptane	11.53	10.63
toluene	9.19	10.79
iso-octane	25.05	23.41
1,2,4-trimethylbenzene	11.87	13.96
tetralin	2.95	3.84

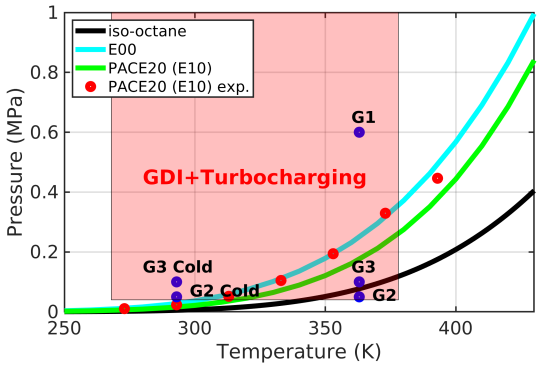

Figure 3.1: Targeted operating conditions of Spray G within p-T diagram; the red patch denotes the possible conditions for the GDI engine with turbocharging while the solid lines and red points indicate the saturated vapor pressure of each fuel

All the available operating conditions are distributed over the diagram of ambient pressure against fuel temperature, as shown in Figure 3.1. It depicts all the available data from ECN, and further, the data is categorized with numbers from one to three. The regime below the boiling curve in Figure 3.1 is the boiling regime. In this regime, droplets experience substantial evaporation, encompassing both heat exchange at the droplet surface and internal heat exchange due to bubble nucleation, growth, and breakup within the droplet. E00 and PACE20 fuels are more volatile compared with iso-octane, as they both are blended with high-volatile fuels such as n-heptane, cyclopentane, and ethanol. It

is worth noting that the vapor pressure curve of E00 and PACE20 are calculated based on ideal vapor-liquid equilibrium, so-called “Raoult’s Law.” Raoult’s law is proposed based on vapor-liquid equilibrium expressing that the liquid mole fraction of each species is equivalent to the mole fraction of its vapor and further simplifies by assuming the Fugacity coefficient of each species is unity. This assumption can be valid in a mixture of non-polar molecules, such as a mixture of alkanes. However, it is widely accepted that Raoult’s law can yield deviations in a mixture of non-polar and polar molecules, such as a mixture of ethanol and iso-octane [113–116]. To ensure the validity of Raoult’s law applied to PACE20, ECN provides experimental data on PACE20 and facilitates a comparison, as shown in Figure 3.1. The experimental pressure curve of PACE20 aligns well with the vapor pressure of E00, whereas the deviation between the curve using Raoult’s law and the experimental one can be observed, albeit minor.

To avoid any uncertainties yielded by Raoult’s law, the investigation of the spray characteristics of each fuel is only conducted in cold-start (G2 Cold) and late-injection (G1) conditions. Under late-injection conditions (G1), unlike pure iso-octane, the footprint of each fuel from E00 and PACE20 is crucial to facilitate stratified combustion. This chapter will transition from the experimental measurement and numerical setup to the validation and examination under each injection condition.

3.1 Experimental measurement and numerical setup

3.1.1 Experimental measurement and available data

The experimental data from ECN are acquired by means of diffuse back-illumination (DBI) extinction imaging measurement for the liquid phase and Schlieren measurement for the vapor phase. The laser signal intensity from DBI measurement varies based on the extinction threshold. Furthermore, Schlieren’s (beam-steering) effects can be mitigated by applying the light diffuser to obtain a proper diffusion angle [51, 117, 118]. Rather than Mie-scattering imaging, ECN recommends DBI measurement as it can provide a less biased liquid boundary and is more suitable as a reference for CFD simulation as it takes into account Schlieren (beam-steering) effects.

Following the assumption that scattering objects are spherical, Mie scattering extinction theory can be applied to obtain the droplets’ liquid volume fraction (LVF). To provide a quantitative and qualitative comparison with CFD simulation data, ECN further post-processed the LVF to acquire projected liquid volume (PLV) images. Therefore, the liquid penetration length and possible liquid boundary can be procured through two different extinction values defined by ECN, as shown in equation (3.1). In this study, the lower

threshold $0.2 \cdot 10^{-3} \mathrm{mm}^3(\mathrm{liquid})/\mathrm{mm}^2$ was applied to process binary PLV data.

$$\begin{aligned} \mathrm{PLV} = \int_{-y\infty}^{y_\infty} \mathrm{LVF}.\mathrm{d}y &= 0.2 \cdot 10^{-3} \frac{\mathrm{mm}^3(\mathrm{liquid})}{\mathrm{mm}^2} \\ &= 2.0 \cdot 10^{-3} \frac{\mathrm{mm}^3(\mathrm{liquid})}{\mathrm{mm}^2}, \end{aligned} \tag{3.1}$$

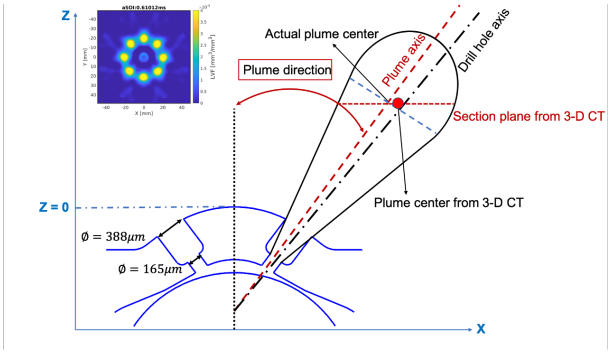

Figure 3.2: The geometry of the Spray G and an example of 3-D computer tomographic (3-D CT) reconstruction section at Z = 30 mm at after the start of injection (aSOI) = 0.61 ms [1]

To follow the concept, “Follow the fuel,” ECN utilized the ensemble-averaged PLV data from 300 injections at three different observing angles, 0°, 22.5°, and 11.25°, to reconstruct the 3-D plume shape using 3-D computer tomographic (3-D CT) reconstruction. The image obtained at the section 30 mm below the injector is shown in Figure 3.2.

However, this technique assumes that the Spray G with an 8-hole configuration is 45° symmetric and requires linear interpolation to fill the gap. It also yields some uncertainties and deviations [51]. The main uncertainty is the droplet diameter d used to acquire the LVF value. As the droplet diameter d varies from region to region, the experimental data is processed using a constant droplet diameter $d = 7\,\mu\mathrm{m}$ measured using phase-doppler interferometry (PDI) [48]. Following this procedure, the produced LVF signal is often underpredicted. Furthermore, the deviation is that the maximum signal pivot point is not always a plume center as the plume axis is not perpendicular to the plume section, as shown in Figure 3.2. Despite all the uncertainties and deviations, the processed 3-D computer tomographic reconstruction data is still reliable regarding the location of the maximum signal pivot point and plume directions [48, 51].

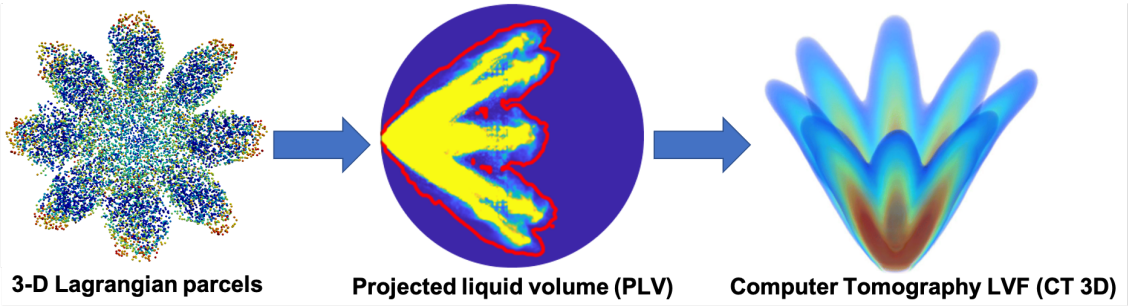

Figure 3.3: The procedure to post-process the simulation data, PLV and 3-D LVF, for comparison [1]; Reprinted with permission

In this chapter, all the simulation data are post-processed in the same manner using Python scripts provided by ECN to deliver a consistent dataset for comparison. The procedure is shown in Figure 3.3. The extinction threshold for the numerical liquid boundary from PLV and the vapor boundary projected using Schlieren probabilities are set to $0.2 \cdot 10^{-3}\text{mm}^3(\text{liquid})/\text{mm}^2$ and $1.0 \cdot 10^{-3}\text{mm}^3(\text{vapor})/\text{mm}^2$, respectively.

3.1.2 Numerical setup

This chapter performs simulations in a computational domain close to the ECN constant-volume chamber, allowing observation of the entire spray evolution under different operating conditions. The computational domain in this study is set up as a cube with a dimension 100 mm. The meshing strategy is to apply a static mesh with several mesh refinements, from the coarsest mesh size 1000 µm to the finest mesh size 125 µm to resolve the turbulence induced by spray. Therefore, the total number of computational cells is 15 million. Figure 3.4 shows the computational domain and mesh details.

The simulation is grid-dependent as the study utilizes Large Eddy Simulation (LES). The mesh quality assessment is carried out using the viscosity ratio proposed by Celik et al. [83] as a criterion for the resolution of LES, described in section 2.1.3. By applying equation (2.18), Figure 3.5 shows the highlighted region (Y = −20 mm to Y = 20 mm and Z = 0 mm to Z = 40 mm) of the spray velocity and the quality examining index.

In Figure 3.5 (b), the viscosity ratio ($\frac{\nu_{t,eff}}{\nu}$) is employed to weigh the overall viscosity against the molecular viscosity. The ratio reaches unity as the sub-grid model produces no sub-grid viscosity. According to Celik et al. [83], the ratio needs to be lower than 20 to resolve 80 % of the kinetic energy. The presented mesh quality is thus sufficient, with a global viscosity ratio between 15 to 20 and a corresponding index around 80 % to 85

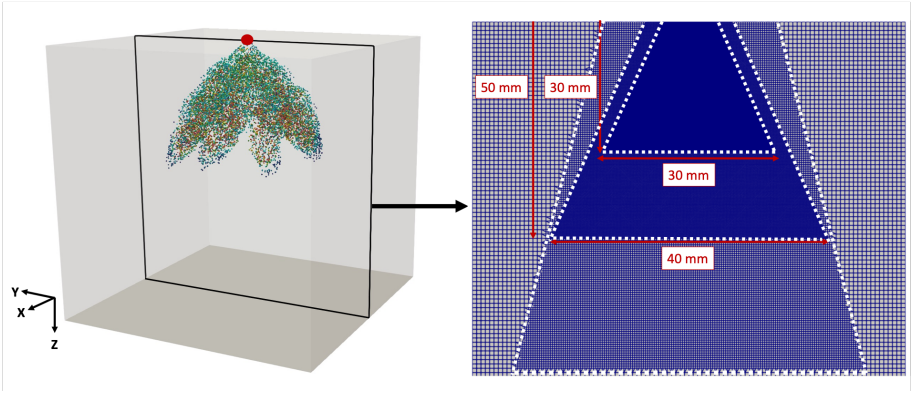

Figure 3.4: The computational domain and mesh details for ECN Spray G (The center of the injector is set up at the origin of the computational domain, which is marked as a red circle)(note: the white broken line is to outline the mesh refinement)

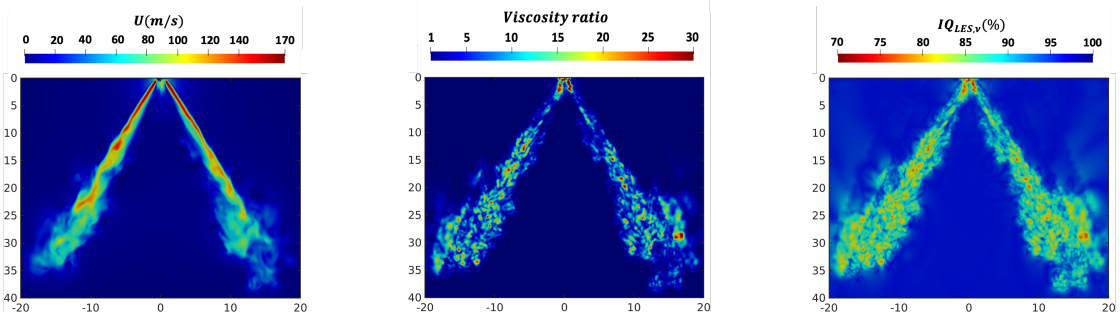

(a) Gas phase velocity (b) Viscosity ratio ($\frac{\nu_{t,eff}}{\nu}$) (c) LES quality index ($IQ_{LES,\nu}$)

Figure 3.5: Examining mesh quality at a time after the start of injection (aSOI) = 0.64 ms

%. Although the maximum value of the viscosity ratio is 25.58 in the region of mesh transition and injector tip, the converted value to the corresponding index is 78.205%. It lies within the suggested range between 75 to 85 % of the kinetic energy [83].

As mentioned in section 2.2.5, the mass flow rate needed to be specified to facilitate the injection model. Figure 3.6 displays the mass flow rate profile from ECN to provide a spray evolution with the consistent experiment [76].

To clarify all the targeted conditions in Figure 3.1, Table 3.3 summarizes the necessary

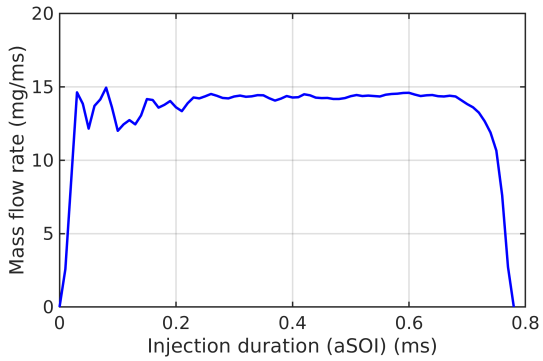

Figure 3.6: Mass flow rate profile of Spray G

information of each condition.

Table 3.3: Essential parameters of the three operating conditions

Spray G	G1	G3	G3 Cold	G2 Cold
Injection condition	late	early	early	early (cold start)
Fuel Temperature (K)	363	363	293	293
Injection Pressure (bar)	200	200	200	200
Ambient Temperature (K)	573	333	293	293
Ambient Pressure (bar)	6	1	1	0.5
Injected Mass (mg)	10	10	10	10

3.2 Early-injection conditions (Spray G3, G3 Cold, and G2 Cold)

3.2.1 Spray characteristics and validation

This section focuses on Spray G under early-injection conditions, as shown in Table 3.3. Under these conditions, the spray is less susceptible to evaporation than Spray G1 under high-pressure, high-temperature ambient conditions. Therefore, the spray ligament breakup is the main characteristic. Figure 3.7 demonstrates the liquid droplets in section P5 scattering within a breakup regime, according to the droplets' local *Oh* and Weber number (*We*). The inner-nozzle flow simulation is conducted using DNS [4].

Figure 3.7 reveals that the majority of the droplets in section P5 (0.4 mm from the

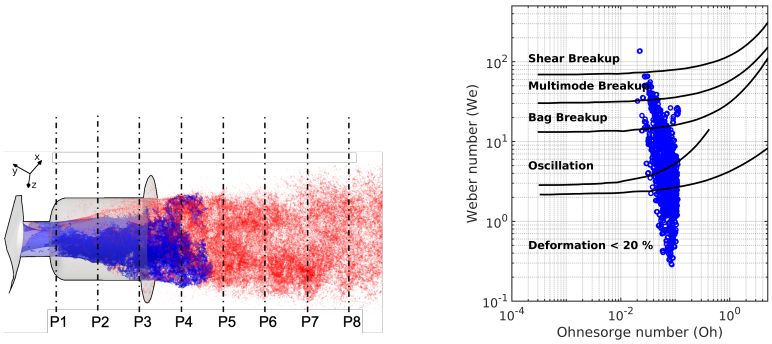

Figure 3.7: Droplets at section P5 distributes within a breakup regime diagram based on Ohnesorge number *Oh* and Weber number (*We*) [4, 119]

nozzle exit) lie within the bag breakup and oscillation regimes. A few droplets with their Weber number (*We*) exceeding 100 may encounter a shear breakup. A three-dimensional morphology is utilized to distinguish the liquid core structure and the liquid droplets marked as blue and red, respectively. After section P6 (0.6 mm from the nozzle exit), the liquid ligament breakup completes.

This thesis applies the necessary information from the DNS simulation to simulate the spray evolution of Spray G under early-injection conditions (G3) using pure iso-octane. Figure 3.8 depicts the spray at aSOI = 0.58 ms and the breakup regimes of droplets at certain regions from upstream to downstream.

In Figure 3.8, the liquid droplets follow the previous pathway from the inner-nozzle flow simulation and start to break up into small droplets. The droplet dynamics move toward the oscillation and deformation region as the Weber number (*We*) decays from spray upstream to downstream. However, the corresponding Ohnesorge number (*Oh*) does not have significant change, and yet the droplets lie within a range $0.03 < Oh < 0.05$. According to the breakup regime, shown in Figure 3.8 (b) and (c), the Ohnesorge number has trivial impacts on the identified drop dynamics only if the Ohnesorge number (*Oh*) below unity. It can be explained that the droplets, after injection, experience droplet breakup and oscillation and further lose their momentum. However, the ratio of the viscous force to the inertial force and surface tension remains balanced. Figure 3.8 indicates that droplet deformation plays a crucial role in Spray G.

Figure 3.9 provides a quantitative comparison with experimental data. The liquid and vapor phases are compared. The difference between all the conditions is the injection and ambient temperatures and ambient pressure, highlighted in Table 3.3. To identify whether all the cases fall into the boiling regime, two parameters are often used [46, 53, 120]; one

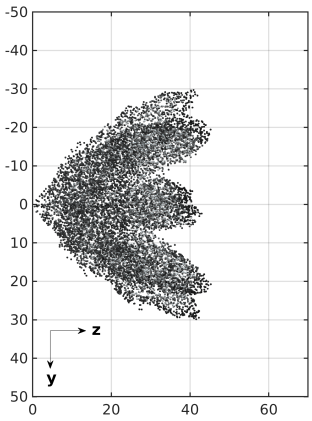

(a) A Lagrangian fields of Spray G at aSOI = 0.58 ms

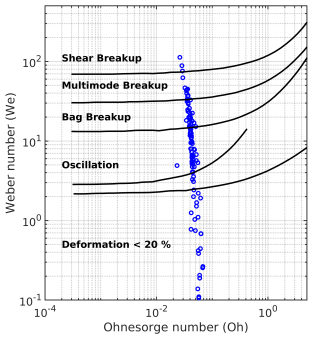

(b) A breakup regime of the upstream droplets within the region z < 5 mm

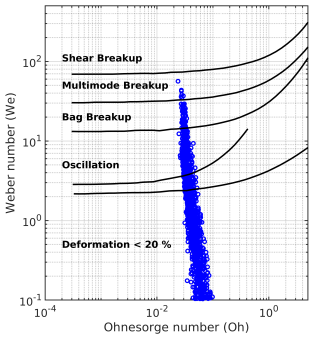

(c) A breakup regime of the downstream droplets within the region z > 35 mm

Figure 3.8: Demonstration of the spray droplets distribution under G3 conditions within the breakup regime diagram [119]

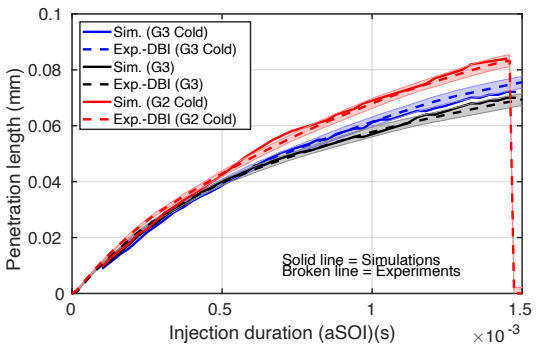

(a) Liquid penetration length

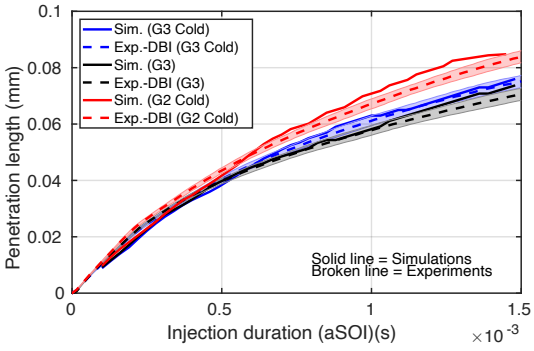

(b) Vapor penetration length

Figure 3.9: Quantitative comparison of the liquid and vapor penetration length. All conditions (G3, G3 Cold, and G2 Cold) are involved.

is the difference between the liquid temperature and the saturated temperature at the ambient pressure, and the other is the ratio (R_p) of the ambient pressure to the saturated pressure at liquid temperature. The criteria of the pressure ratio (R_p) is displayed in Table 3.4.

Table 3.4: Boiling regime from the pressure ratio (R_p)

$R_p < 0.3$	Flash boiling
$0.3 < R_p < 1$	Boiling onset
$R_p > 1$	Non-boiling

By applying the pressure ratio (R_p) to all three cases, only the G3 case is close to the boiling onset with its pressure ratio (R_p) equal to 1.296, compared with G2 Cold and G3 Cold with their ratio (R_p) equal to 9.78 and 19.57, respectively. Furthermore, the ambient pressure of the G2 Cold case is half of those in the G3 and G3 Cold cases. All the effects will influence the penetration length in both liquid and vapor phases. As evident in Figure 3.9, G2 Cold exhibits the longest penetration length due to low ambient pressure. Interestingly, the penetration of G3 and G3 Cold are comparable even though the G3 case is close to the boiling regime and may yield higher evaporation. By merely investigating both the vapor and liquid penetration length, it provides limited information for the evaporation effect between different conditions; furthermore, the penetration of both liquid and vapor remains comparable. Notably, the simulation data demonstrate a strong agreement with the experimental data in all cases. For a qualitative assessment, Figure 3.10 presents a comparison of the liquid plume boundary using the projected liquid volume data (PLV).

The evaporation effect can be observed in the liquid plume boundary, as shown in Figure 3.10. Due to the minor evaporation effect, the liquid plume boundary in G3 cold case is more intact, and no plume detachment appears at aSOI = 1.21 ms compared with the other two cases. The evaporation effect can be captured by the simulation. The numerical spray plume tips downstream in the G3 Cold case are more revealing than Spray G3. The under-prediction of liquid penetration length at aSOI = 1.21 ms in the G3 Cold case also appears in Figure 3.9.

Due to the boiling onset in G3, each plume can not be easily identified compared with G3 Cold cases, especially at aSOI = 0.58 ms. In a comparison of G3 Cold and G2 Cold, the plume shape of G2 Cold also cannot be easily identified even though both are far from the boiling regime. This phenomenon can also be influenced by the ambient pressure. With low ambient pressure, the spray plume tends to be more dispersed even though it does not reach the boiling regime with strong spray collapse [112]. The deviation between the simulation and experiment occurs at a late-injecting time aSOI = 1.21 ms, where the simulation produced a more dispersed boundary compared with the experiment. This will not be observed if one solely conducts a global quantitative comparison, such as penetration length. Furthermore, by comparing the experimental liquid boundary

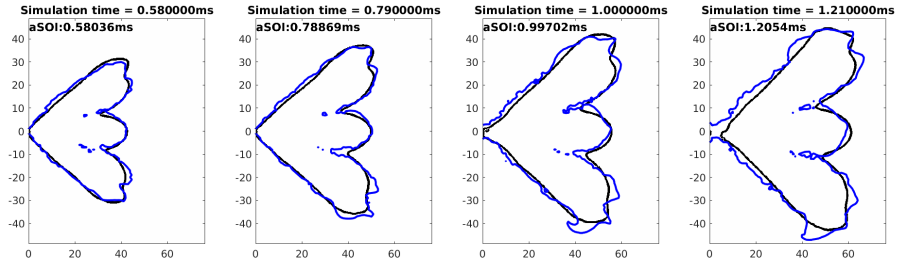

(a) Spray G3

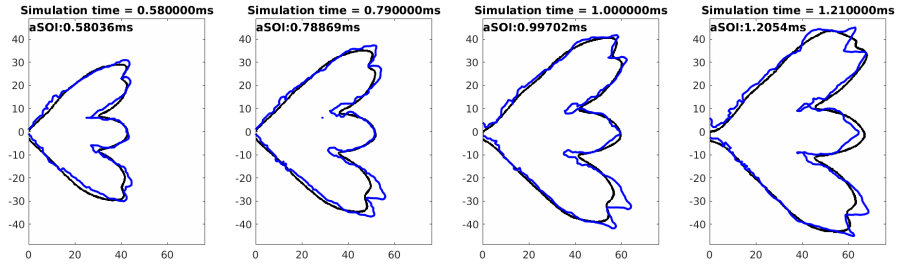

(b) Spray G3 Cold

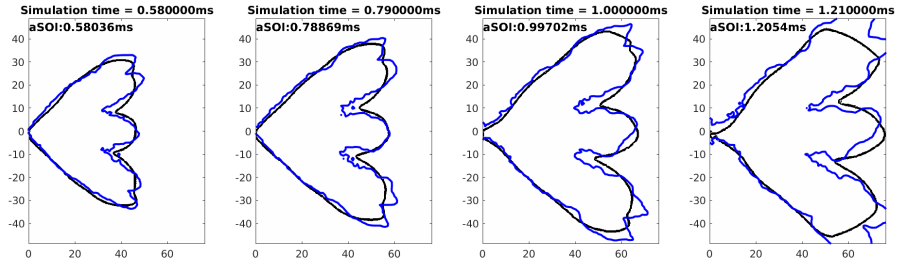

(c) Spray G2 Cold

Figure 3.10: Qualitative comparison of the projected liquid boundary measured by DBI with extinction threshold equal to $0.2 \cdot 10^{-3}(\mathrm{mm}^3(\mathrm{liquid})/\mathrm{mm}^2)$. Black line: the experimental data, Blue line: the simulation data)

between G3 and G2 Cold cases solely, the spray plume detachment can be clearly observed in the G3 case, revealing higher evaporation.

Figure 3.11 provides a more direct comparison of the evaporation effect between these

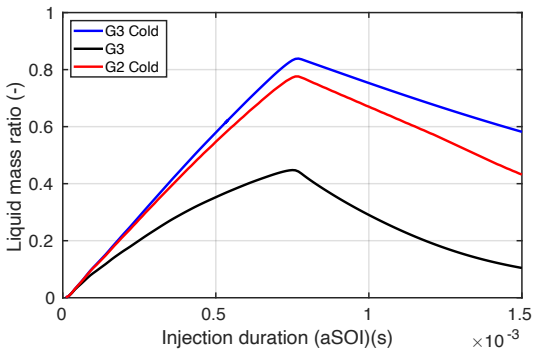

Figure 3.11: Time evolution of the liquid mass ratio($\text{mass}_{liquid}/\text{mass}_{total}$) demonstrates the evaporation effect between G3, G3 Cold and G2 Cold.

three cases by demonstrating the liquid mass ratio, which is the current liquid fuel mass in the constant-volume chamber normalized by the overall injected mass (10 mg). Both profiles reach the peak at aSOI = 0.78 ms, which is the overall injection duration. Despite following the same trend, G3 contains only 45 % of the liquid mass at the end of the injection duration, while G3 Cold and G2 Cold have almost 85 % and 75% of the liquid mass within the constant-volume chamber, respectively. The contained liquid mass in Spray G3 vaporizes exponentially in the aftermath of the injection.

3.2.2 Assessment of injection distribution models

Efforts, by far, have been dedicated to comparing experimental data and the simulation, and, further, focusing on the spray characteristics under different conditions. It is evident that due to the counter-bore inner-nozzle configuration, the primary atomization takes place in the inner-nozzle region. This mechanism, consequently, triggers the liquid core breakup in the vicinity of the nozzle exit, as shown in Figure 3.7. The conventional injection distribution model, commonly referred to as “the blob method,” assumes that the ejected droplets are uniformly distributed and behave as a “blob” with a size equivalent to the nozzle diameter. This widely accepted model has found success in both academic and industrial applications. However, under this assumption, the droplet size is approximately 10 to 20 times larger than the observed droplet sizes obtained from experiments and simulations. This section will carry out a comprehensive comparison between the blob method and the statistical droplet distribution method in equation (2.54). The two cases are referred to as Cases 1 and 2, as shown in Table 3.5. Both utilize the same framework for the rest of the Lagrangian models proposed in Chapter 2 to deliver a fair comparison.

The presented assessment is based on the G3 case. Figure 3.12 compares the different droplet distribution models in the liquid phase.

Table 3.5: Lagrangian models used in the present study

simulation cases	Case 1	Case 2
Droplet distribution	statistical droplet distribution Eq.(2.54)	Blob method (d = 165 µm)

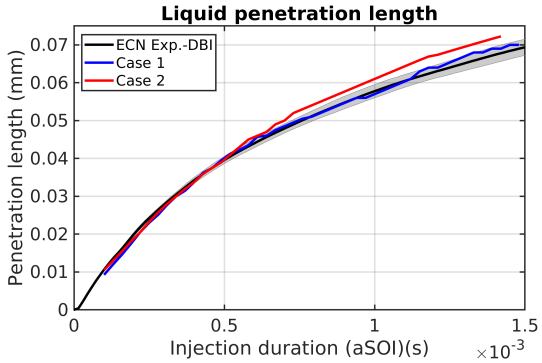

(a) Quantitative comparison of the liquid penetration length

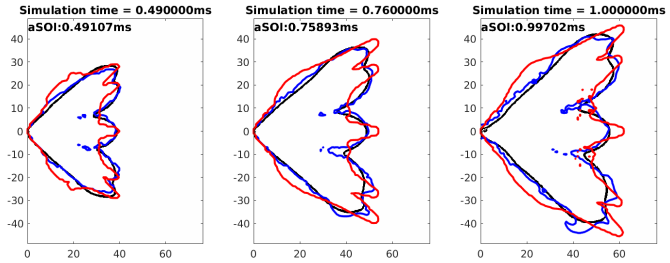

(b) Qualitative comparison of the projected liquid plume boundary derived by projected liquid volume (PLV). The black solid line indicates the experiment (ECN), blue: Case 1, and red: Case 2

Figure 3.12: Comparison between different droplet distribution models in liquid phase

By using the blob method, the penetration length is in good agreement with experimental data, even though some minor overprediction appears after aSOI = 0.76 ms. However, the generated spray plume shape from Case 2 is relatively wide, and the spray plume tips downstream are unphysically sharp. In the previous discussion in Section 4.1.1, The sharp

tip can be observed in the Spray G3 Cold case experimentally and numerically owing to the evaporation effect, shown in Figure 3.10. It is, however, absent in the Spray G3 case. The cause of the disparity between the plume shapes yielded by different models may lie in the droplet momentum due to large droplets generated by the blob method. It merits a more in-depth investigation by extracting the Weber number (*We*) and the Ohnesorge number (*Oh*).

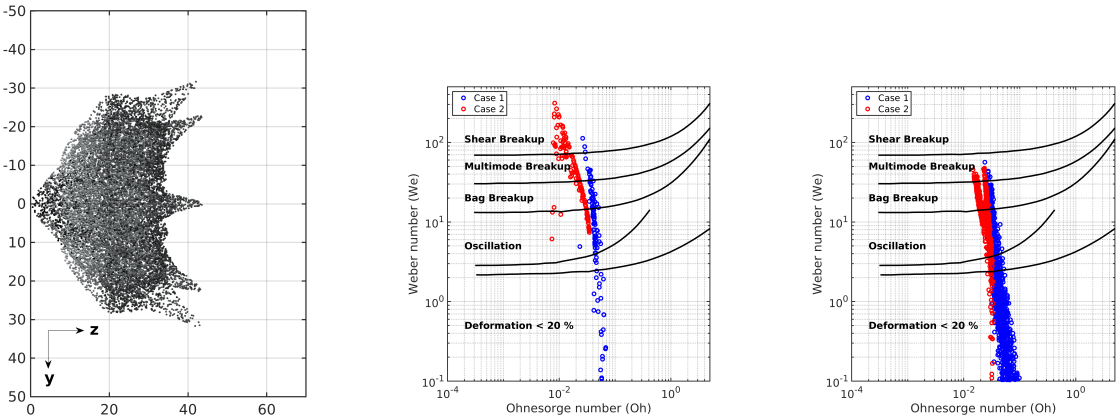

(a) Lagrangian fields of Spray G using the blob method at aSOI = 0.58 ms

(b) Breakup regime of the upstream droplets within the region z < 5 mm

(c) breakup regime of the downstream droplets within the region z > 35 mm

Figure 3.13: Comparison of the spray droplets distribution under G3 condition within the breakup regime diagram by Hsiang and Faeth [119].

Figure 3.13 presents a comparison of different droplets' distribution within the breakup regime at aSOI = 0.58 ms. In comparison to the spray shape using the statistic droplet distribution method, as shown in Figure 3.8 (a), the sharp plume tips appear in the Lagrangian fields, as shown in Figure 3.13 (a). Using the Blob method, the ejected Lagrangian particles are at the size of the inner-nozzle diameter (165 µm). Although the same momentum setup is applied from the injection model, the Weber number of the droplets in the vicinity of the nozzle exit is higher, and the vast majority of the droplets still lie on the shear breakup regime, as shown in Figure 3.13 (b). In the spray downstream region, the majority of the droplets are still at the multi-mode and bag breakup regime stages, in contrast, with the droplets using the droplet distribution function. Thus, it is evident using the blob method that the liquid droplets experience a delayed breakup, resulting in sharp spray plume tips downstream.

Regardless of which droplet distribution models are utilized, the obtained momentum must be conserved using the same injection model. Using the blob method, the Lagrangian particles may contain lower-density liquid fuel. This phenomenon can be proven by comparing the cross-section liquid volume fraction (LVF) using 3-D computer tomographic reconstruction, as shown in Figures 3.2 and 3.3.

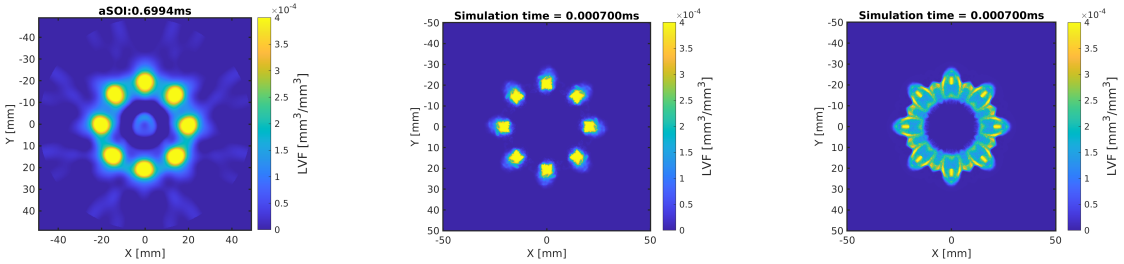

(a) Experiment (ECN) (b) Case 1 (c) Case 2

Figure 3.14: Comparison of the liquid volume fraction (LVF) at cross-section z = 30 mm acquired by 3-D computer tomographic reconstruction

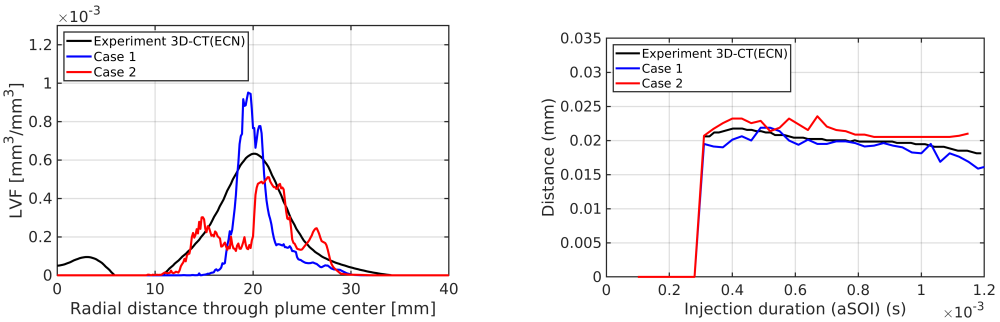

(a) The averaged LVF profiles of the eight plumes

(b) The location of the plume center

Figure 3.15: Quantitative comparison of the liquid volume fraction (LVF) at cross-section $z = 30$ mm acquired by 3-D computer tomographic reconstruction

Figure 3.14 compares the liquid volume fraction (LVF) at a cross-section z = 30 mm, which is recommended by ECN. According to the experimental data, the spray penetrates the cross-section in the shape of a complete circle. The spray does not disperse, although there are some weak signals in the surroundings. This phenomenon can be reproduced in Case 1 using the statistical droplet distribution method. In contrast, the spray is

notably dispersed in Case 2 using the blob method. The results reflect the fact that using the blob method with the same mass and velocity setup for the injection model, the Lagrangian particles may contain lower-density liquid fuel. Figure 3.15 further compares the averaged LVF profiles of the eight plumes and the location of the plume center obtained from 3-D computer tomographic reconstruction. This makes it possible to quantitatively investigate the LVF signal produced by different simulations. Case 1, using the statistical droplet distribution method, yields a concentrated LVF signal and a narrower profile than experimental data, although the plume cross-section shapes are consistent with experimental data. On the other hand, Case 2, using the blob method, yields a dispersed LVF signal. This results in a mismatch with the plume center acquired by 3-D computer tomographic reconstruction, as shown in Figure 3.15 (b).

Utilizing the blob method as an injection distribution model is a practical approach to achieving accurate penetration lengths. However, its application can introduce uncertainties, especially when dealing with different types of injectors, and it tends to overpredict the size of ejected Lagrangian particles, particularly in the case of ECN Spray G. This overprediction leads to unphysical spray plume tips downstream due to the delayed breakup process. Additionally, the larger Lagrangian particles result in smaller densities, thereby generating a dispersed liquid volume fraction (LVF).

3.2.3 Fuel characteristics under the G2 Cold condition

By far, the suite of Lagrangian models for GDI spray is validated under several operating conditions (G3, G3 Cold, and G2 Cold) using pure iso-octane. In real GDI engines, however, gasoline consists of several hydrocarbons, including Paraffins, Aromatics, Oxygenates, and so on. Although iso-octane is widely used as a gasoline surrogate due to its chemical similarity and major compound of gasoline, the evaporation effects in between behave differently, as shown in Figure 3.1. The evaporation effects of multi-component fuel can influence the emission of GDI engines, especially in stratified combustion mode and cold-start conditions. This section is the preliminary work for Chapter 4, Spray-wall interaction and wall film development in a constant-volume chamber, and focuses on multi-component gasoline surrogates (E00 and PACE20 (E10)) under G2 Cold condition. This condition is set up by ECN to simulate cold-start conditions in real GDI engines.

Figure 3.16 demonstrates a comparison of the global penetration length in both liquid and vapor phases. All fuel exhibits comparable behavior in penetration length, although all have different values of the pressure ratio (R_p), 2.01 for E00 and 3.53 for PACE20. Furthermore, different values of the pressure ratio (R_p) between the experiment and Raoult's law are also found. The experimental value is 2.13, close to E00 fuel. However, this deviation does not affect the global penetration length. A phenomenon of this kind

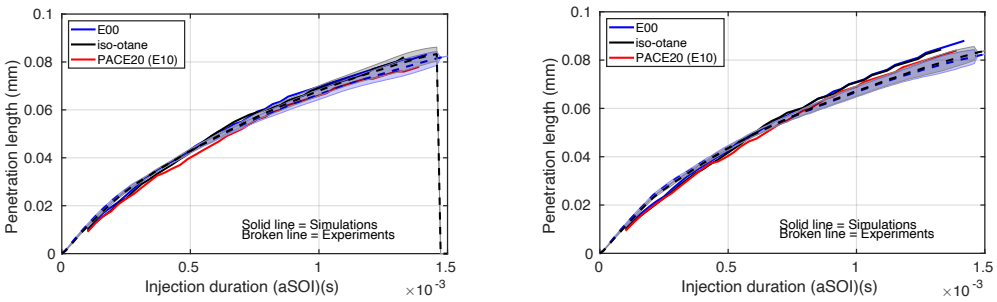

(a) Liquid penetration length (b) Vapor penetration length

Figure 3.16: Quantitative comparison of the liquid and vapor penetration length using different fuels at ECN G2 Cold condition

has been proved and justified by Keller et al. [121]. It reveals that the spatial distribution can vary between the ideal vapor-liquid equilibrium schemes and the non-ideal ones due to liquid fuel azeotropic behaviors.

To provide a more complete analysis of different fuels and comparison against experimental data on E00 and PACE20, Figures 3.17 display a comparison of PLV images. Figures 3.17 (a) and (b) show a good agreement between the experiment and simulation and can further justify that under cold-start conditions without any boiling onset, liquid fuel azeotropic behaviors have a minor effect. Most interestingly, the plume shapes of all fuels are nearly identical despite their difference in vapor pressure, as shown in Figure 3.1. This phenomenon explains under the cold-start conditions with fuel temperature at the ambient temperature (T = 293 K), the evaporation is induced mainly by the air entrainment. Moreover, the air entrainment is influenced by the ambient pressure. With low ambient pressure, the spray plume is more dispersed and allows more air to circulate toward the spray plume. This reflects the previous discussion that the G2 Cold case has merely 5% less liquid mass of iso-octane than the G3 Cold case, as shown in Figure 3.11. Furthermore, by solely examining the plume shapes, information can only be acquired, which are the similarity of the global spray momentum and the similarity of the boiling effect. Given that all fuels exhibit consistent plume shapes, E00 and PACE20 have lower R_p as they consist of several high-volatile fuels, which are n-pentane, cyclopentane, and ethanol. Both should have stronger evaporation effects than pure iso-octane.

Figure 3.18 demonstrates the residual liquid mass with injection time. The evaporation effects between different fuels can be observed. E00 with a high percentage of high-volatile fuel, n-pentane, yields at least residual liquid mass. In contrast, PACE20 has a similar evaporation trend to E00 despite containing approximately 10% of ethanol in mass.

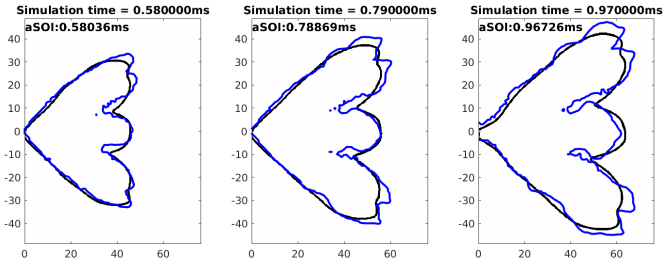

(a) E00. Black line: the experimental data, Blue line: the simulation data

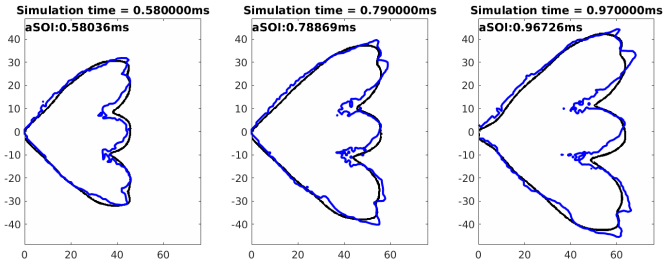

(b) PACE20. Black line: the experimental data, Blue line: the simulation data

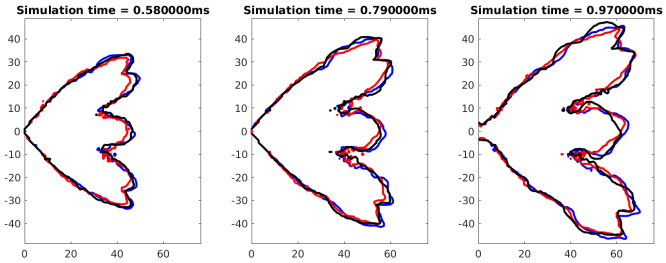

(c) Comparison of different fuels. Black line: E00, Blue line: iso-octane, and red line: PACE20 (E10)

Figure 3.17: Qualitative comparison of the projected liquid boundary measured by DBI with extinction threshold equal to $0.2 \cdot 10^{-3} (\mathrm{mm}^3(\mathrm{liquid})/\mathrm{mm}^2)$

It is evident that both gasoline surrogates have stronger evaporation than iso-octane, which is limited to be observed in plume shapes.

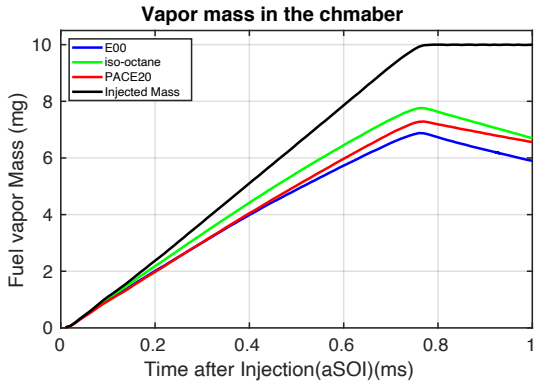

Figure 3.18: Temporal evolution of the residual liquid mass and injected mass demonstrates the evaporation effect between E00, iso-octane, and PACE20 (E10).

3.3 Late-injection conditions (Spray G1)

In the previous section, the suite of models used in this thesis has been proven capable of capturing the spray penetration and projected spray plume boundary in both the liquid and vapor phases under early-injection conditions. However, GDI engines operate not only under early-injection conditions (to achieve homogeneous combustion or proper mixture for a cold start) but also under late-injection conditions (for stratified combustion). The latter type of combustion takes place during the compression phase and close to the cylinder top dead center (TDC) [12]. There is limited time for spray atomization and further mixture with the in-cylinder flow to achieve lean or ultra-lean stratified combustion. ECN thus set up engine-like late-injection operating conditions to acquire an in-depth understanding. The operating conditions of Spray G1 are shown in Figure 3.1 and Table 3.3. This section transitions from an investigation of the cases using pure iso-octane to the cases using multi-component gasoline surrogates (E00 and E10).

3.3.1 Investigation on spray characteristics using iso-octane and on spray distribution models

Following the previous discussion, the unphysical effects induced by the blob method can be observed under the G3 condition due to the delayed breakup process. Hereby, the investigation ensues on late-injection conditions (G1). Furthermore, a simulation conducted by a research group in ECN using LES and their Corrected Distortion model [88] are utilized for this comparison [107]. All the cases are shown in Table 3.6.

Table 3.6: Lagrangian models used in the present study

simulation cases	Case 3	Case 4	Case 5
Evaporation	Section 2.2.3	Section 2.2.3	CD-Frössling[88]
Heat transfer	Eq.(2.31)	Eq.(2.31)	Eq.(2.31)
Breakup model	Section 2.2.4	Section 2.2.4	KH-RT [102]
Droplet distribution	Eq.(2.54)	Blob (d = 165 µm)	Blob (d = 165 µm)

Figure 3.19 provides a quantitative and qualitative comparison in the liquid phase using the projected liquid volume (PLV) data. Unlike early-injection cases, (G3, G3 Cold, and G2 Cold), Spray G1 yields strong evaporation, and consequently, the extinction of the projected liquid volume (PLV) signal takes place at approximately aSOI = 1.1 ms. This phenomenon is captured in Case 3. On the contrary, PLV extinction remains absent in Cases 4 and 5, which use the blob method as an injection distribution model. Furthermore, the liquid penetration of Spray G1 is shorter than in early-injection cases due to the high ambient pressure and temperature. With high ambient pressure, spray plumes are less dispersed and more intact compared with early-injection cases, especially the G2 Cold case.

Figure 3.19 (b) presents a qualitative comparison of the projected liquid volume (PLV) boundary, contrasting the experimental data and numerical results. The blue and red solid lines refer to Cases 3 and 4, respectively. In Case 4, the sharp tips of the spray downstream disappear compared with the G3 case. Compared to early-injection conditions, Spray G1 has a more compact plume shape due to high ambient pressure and temperature. Both experimental and numerical data show that the projected liquid boundary starts to extinct at aSOI = 1.12 ms. The extinction of the projected liquid boundary is almost complete at aSOI = 1.21 ms. It results in a sudden drop in the liquid penetration length at aSOI = 1.25 ms, as shown in Figure 3.19 (a). In Figure 3.19 (b), Case 3, using the statistical droplet distribution method, behaves consistently with the experimental data. Interestingly, Case 4 has slower extinction, and the projected liquid volume (PLV) boundary remains intact even at aSOI = 1.25 ms. Furthermore, the extinction in Case 4 starts from the edge instead of in the middle, as the experimental data and the data in Case 3. This phenomenon likely occurs due to the size of the liquid droplets. As the Lagrangian particles introduced to the constant-volume chamber in Case 4 are of the size as the inner-injector diameter (165 µ/meter), the volume-to-surface ratio of each droplet is much larger than the real liquid droplets. It can yield an evaporation delay, resulting in the phenomenon shown in Figure 3.19.

Figure 3.20 further demonstrates the time evolution of the Sauter mean diameter (SMD).

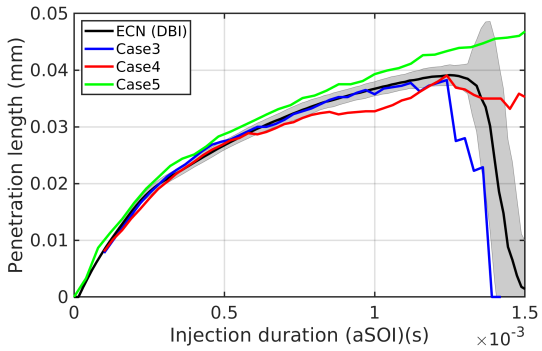

(a) Quantitative comparison of the liquid penetration length

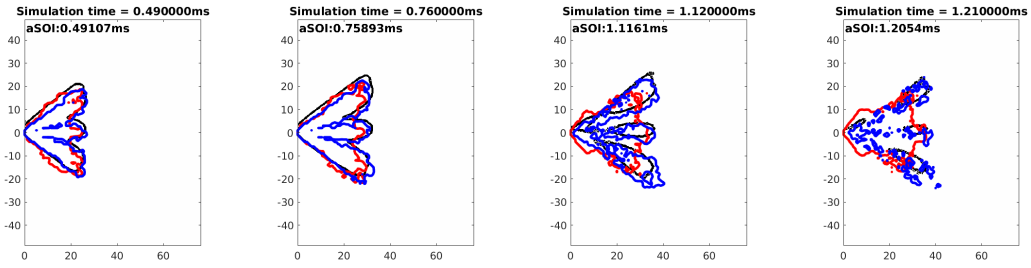

(b) Qualitative comparison of the projected liquid plume boundary derived from projected liquid volume (PLV) data(Note: black line: experiment, blue line: Case 3 and red line: Case 4)

Figure 3.19: A comparison of different simulations in the liquid phase.

The measured section is at z = 15 mm. The experimental SMD data is acquired from ECN and measured by means of phase-Doppler interferometry (PDI) [47, 51]. It is worth noting that the measured experimental data is focused on a single spray plume, whereas the numerical data is averaged from eight spray plumes. The experimental droplet SMD lies in a region between 7 to 10 µm after aSOI = 0.9 ms, whereas the numerical droplet SMD in Case 3 is approximately at 7 µm. Although this is a slight underprediction, Case 3 agrees well with the measured SMD data. Interestingly, the numerical droplet's SMD in Case 4 lies in the range between 12.5 to 16 µm after aSOI = 0.9 ms. It is 1.5 to 2 times larger than the measured liquid droplets' SMD. Large droplets can yield delayed evaporation, which explains the problem with signal extinction and liquid penetration length, as shown in Figure 3.19.

So far, the delayed evaporation effect has been observed in the case using the blob method and is further investigated by comparing the Sauter mean diameter of the liquid

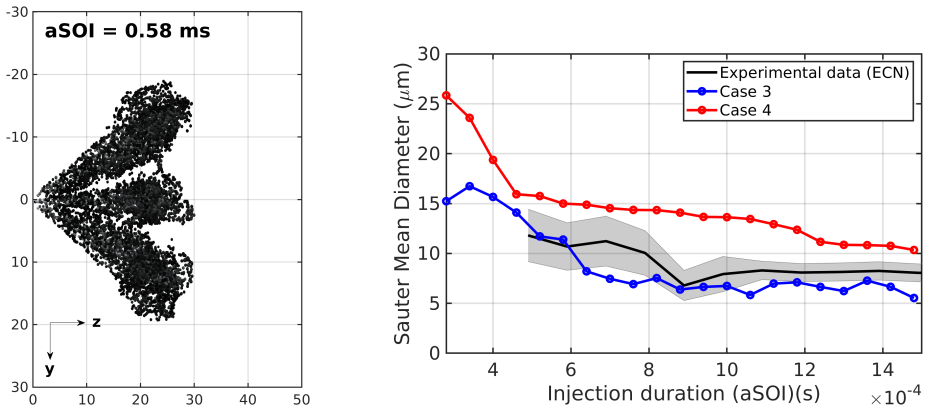

Figure 3.20: Sauter mean diameter (SMD) time evolution profile at section z = 15 mm; the experimental data is measured by Scott Parish (GM) using phase-doppler interferometry (PDI) [47, 51]. (Note: The PDI data is temporal and spatial with a radial direction. The black solid line is the spatially averaged data, and the shadow represents the range.)

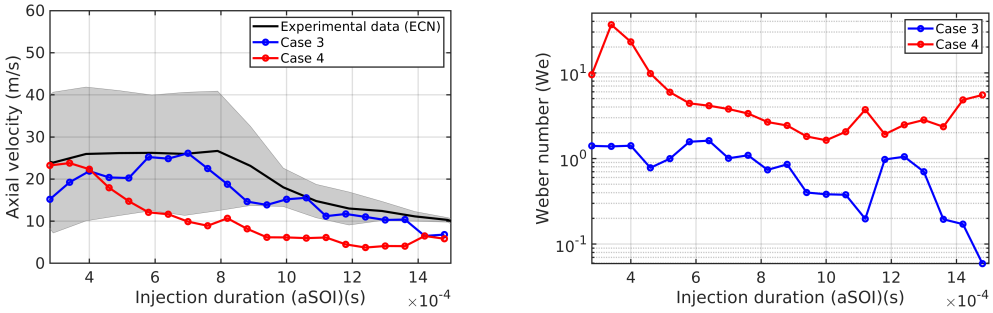

Figure 3.21: Mean velocity normal to the z direction profile and the corresponding mean Weber number profile with time at section z = 15 mm; the experimental data is measured by Scott Parish (GM) using phase-Doppler interferometry(PDI) (ECN 3^{rd} workshop) [47]. (Note: the PDI data is temporal and spatial with a radial direction. The black solid line is the spatially averaged data, and the shadow represents the range.)

droplets at the cross-section z = 15 mm. The deviation in the liquid droplet size can further affect the momentum and inertial force of the droplets and, consequently, result in a different penetration length. It merits more investigation by extracting the axial

velocity of the plume (normal to the z-direction) and its corresponding Weber number (*We*) at the cross-section z = 15 mm, as shown in Figure 3.21.

The axial velocity in Case 3 agrees well with the experimental data, whereas the velocity in Case 4 decays notably after the injection aSOI = 0.78 ms. This explains the underprediction of the liquid penetration length in Case 4 after aSOI = 0.78 ms, as shown in Figure 3.19. Case 4, using the blob method, has a relatively high Weber number, indicating a higher inertial force but a fast axial velocity decay. The high Weber number might be due to the droplet size. Furthermore, the Weber number in Case 3 strongly decays after aSOI = 1.25 ms, whereas it remains in Case 4. This reflects the full evaporation of the liquid droplets. A phenomenon of this kind can be observed in Figure 3.19 as liquid signal extinction.

Under late-injection conditions (Spray G1), evaporation effects are crucial in spray formation. Evaporation effects are susceptible to the accurate prediction of droplet size. Using the blob method, droplet size is overpredicted, resulting in an evaporation delay.

3.3.2 Spray characteristics of different fuels

Under late-injection conditions (G1), the time for processing the air-fuel mixture is limited. Evaporation, therefore, plays a crucial role in the performance of stratified combustion. From a simulation modeling point of view, it is even imperative to correctly capture the evaporation effect and further reproduce the stratified combustion. As previously discussed, the evaporation and breakup delay will happen if the blob method is used. However, this is still unclear whether the statistical droplet distribution function can also be applied to multi-component fuels (E00 and PACE20 (E10)) and further capture the evaporation effect. Hereby, an assessment of the capabilities of the suite of Lagrangian models proposed in this thesis for capturing the evaporation effect on multi-component fuels is conducted.

Figure 3.22 (a) compares the liquid penetration length of different fuels (iso-octane, E00, and PACE20 (E10)). The simulation data align well with the experimental data from DBI measurement both qualitatively and quantitatively, as shown in Figure 3.22 (a) and (b). During the injection, all fuels behave identically; however, E00 and PACE20 exhibit late full evaporation compared with iso-octane. The phenomenon occurs due to the containing of heavy, low-volatile components, such as n-undecane, tetralin, and 1,2,4-trimethylbenzene, in both E00 and PACE20. The evaporation difference on different fuels can be clearly observed in Figure 3.22 (c). During the injection(aSOI before 0.78 ms), the projected liquid boundary of all fuels aligns together, whereas the evaporation effects start to manifest after aSOI = 1.21 ms. At aSOI = 1.21 ms, all liquid iso-octane is fully evaporated, while the plume of E00 and PACE20 remains despite fractured plume shape.

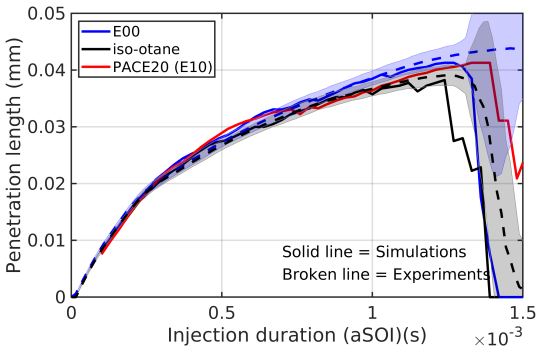

(a) Quantitative comparison of the liquid penetration length

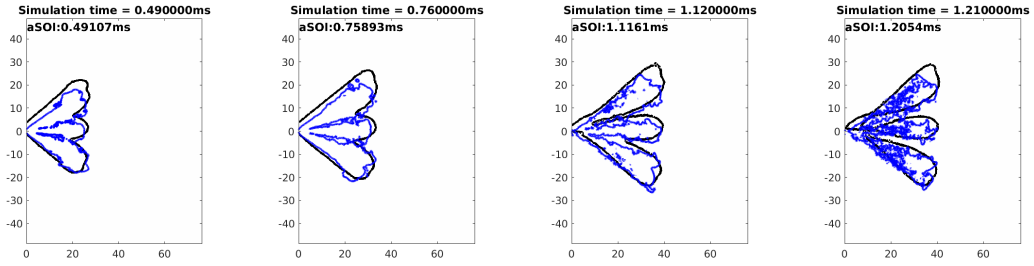

(b) Qualitative comparison of the projected liquid plume boundary derived from projected liquid volume (PLV) data of E00 (Note: black line: experiment, blue line: simulation)

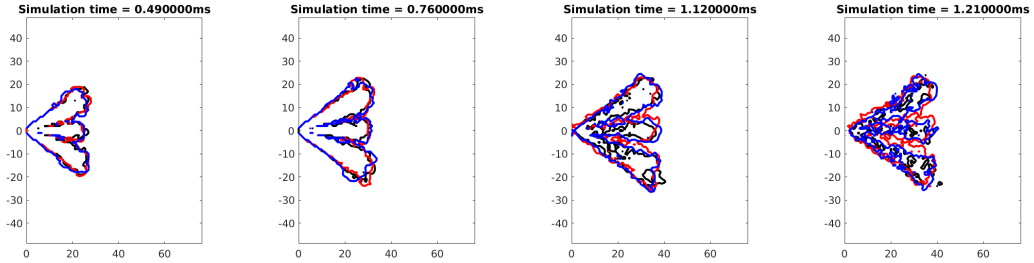

(c) Qualitative comparison of the projected liquid plume boundary derived from projected liquid volume (PLV) data of different fuels (Note: black line: iso-octane, blue line: E00, and red line: PACE20 (E10))

Figure 3.22: A comparison of different simulations in the liquid phase.

To justify and clarify the evaporation effects on different fuels, Figure 3.23 demonstrates

the temporal evolution of high-volatile and low-volatile components mass in E00 and PACE20. The category of high-volatile and low-volatile components in E00 and PACE20 are shown in Table 3.7.

Table 3.7: Definition of high-volatile and low-volatile fuels

E00		PACE20	
high-volatility	low-volatility	high-volatility	low-volatility
iso-octane	n-undecane	iso-octane	tetralin
n-pentane	(x)	n-pentane	toluene
(x)	(x)	cyclopentane	1,2,4-trimethylbenzene
(x)	(x)	1-hexene	(x)
(x)	(x)	ethanol	(x)
(x)	(x)	n-heptane	(x)

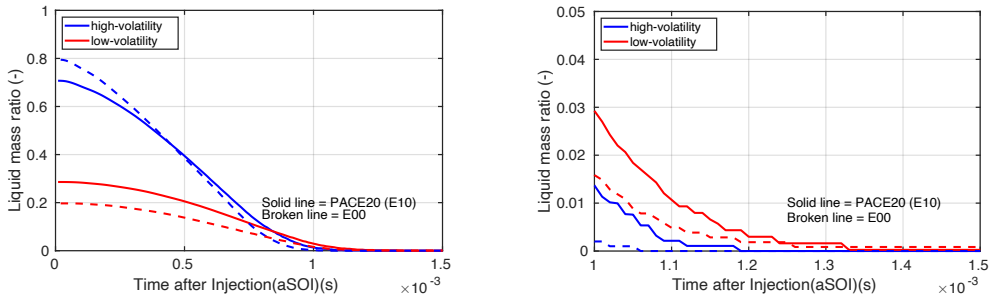

Figure 3.23: Temporal evolution of the liquid mass ratio ($\text{mass}_{liquid}/\text{mass}_{total}$) demonstrates the evaporation effect between E00, and PACE20 (E10). Note: figure on the right-hand side is zoomed in from aSOI = 1 to 1.5 ms.

Figure 3.23 shows that the high-volatile components of E00 exhibit more rapid evaporation than those of PCAE20. It is because E00 comprises a high amount of n-pentane, which is highly volatile even compared with ethanol under the G1 condition. On the other hand, n-undecane, the low-volatile component of E00, behaves similarly to those of PACE20. As PACE20 contains approximately 30% of low-volatile components, the overall liquid fuel remains until aSOI = 1.35. This phenomenon explains the extended liquid penetration of PACE20, as shown in Figure 3.22.

As normally, low-volatile fuels are heavy and might be less influenced by spray jet flow. High-volatile fuels, on the contrary, have their characteristics otherwise. To investigate such phenomena between high- and low-volatile components, one can define the indexes

of those two groups by summing up their mass fractions. The indexes are expressed as:

$$\text{High-volatility} = \frac{Y_{iso-octane} + Y_{n-pentane}}{Y_{iso-octane} + Y_{n-pentane} + Y_{n-undecane}}, \tag{3.2}$$

$$\text{Low-volatility} = \frac{Y_{n-undecane}}{Y_{iso-octane} + Y_{n-pentane} + Y_{n-undecane}}, \tag{3.3}$$

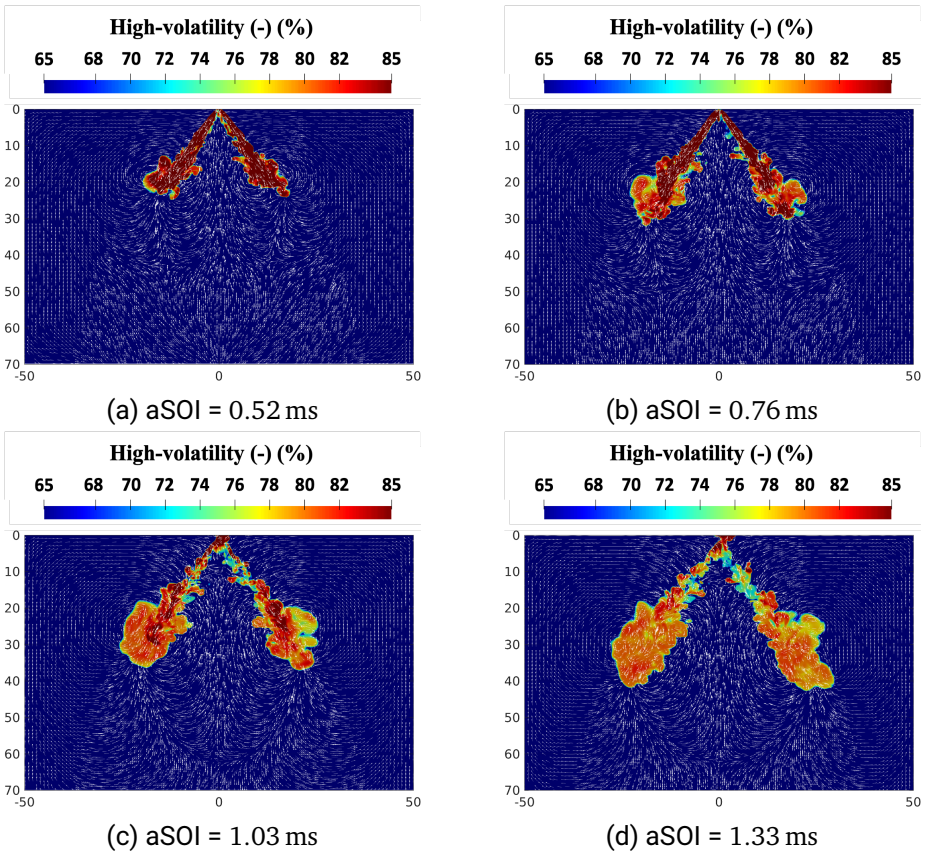

(a) aSOI = 0.52 ms (b) aSOI = 0.76 ms

(c) aSOI = 1.03 ms (d) aSOI = 1.33 ms

Figure 3.24: Time evolution of the high-volatile components of E00 fuel at late-injection condition (ECN G1); The definition of high-volatile components can be found in equation 3.2

Figures 3.24 and 3.25 demonstrate the time consecutive spatial distribution of high- and low-volatile components up to aSOI = 1.33 ms. It is worth noting that the presented ranges

of these two indexes are different, as liquid E00 fuel contains merely 18% n-undecane by volume. The characteristics of these two groups are distinctively different. During the injection (aSOI $<$ 0.78 ms), a high amount of high-volatile components vaporizes. The evaporation of high-volatile components occurs mainly along the spray core, whereas n-undecane evaporates on the edge of the spray core. Due to the heavy weight of n-

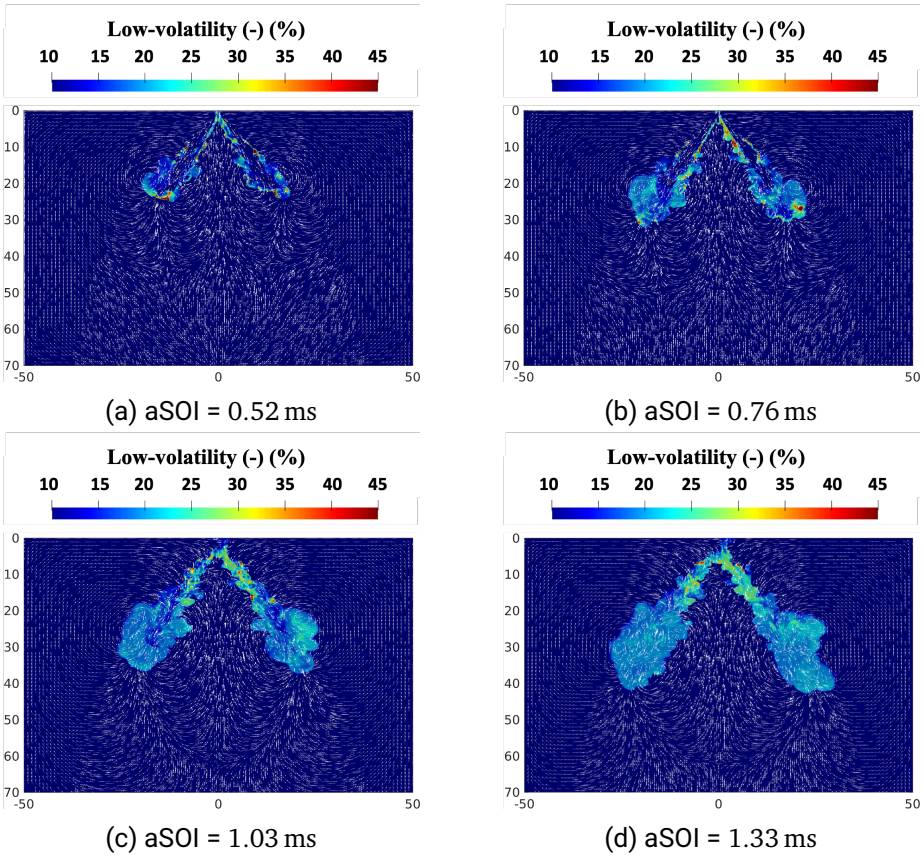

(a) aSOI = 0.52 ms (b) aSOI = 0.76 ms

(c) aSOI = 1.03 ms (d) aSOI = 1.33 ms

Figure 3.25: Time evolution of the low-volatile component of E00 at late-injection condition (ECN G1); The definition of high-volatile components can be found in equation 3.3

undecane, it is less susceptible to spray jet flow; a high percentage of n-undecane appears upstream after aSOI = 1.03 ms. Furthermore, as spray jet flow propagates downstream, it pushes static air and further generates air entrainment disturbing the spray vapor plumes. This phenomenon is clearly observed. However, due to different densities of high- and

low-volatile components, the susceptibility of the air entrainment is different in between. The low-volatile vapor plume remains intact with time until aSOI = 1.33 ms, whereas the structure of the high-volatile vapor plume is destroyed by the air entrainment, especially after the injection. It, furthermore, provides a notion that under stratified combustion, low-volatile fuels are likely first to be ignited, and the flame propagates toward the high-volatile fuels.

Similar research has also been done experimentally by Cordier et al. [110], using planar laser-induced fluorescence (PLIF) to investigate different characteristics between fuels blended with different percentages of ethanol from E00 to E85. The study proposed a mechanism for the heterogeneous phenomenon of multi-component fuels. According to the mechanism, the heterogeneous phenomenon occurs after the injection where the strong air entrainment due to momentum exchange between static air and spray disturbs the high-volatile vapor plume and pushes the plume further downstream. The simulation results align well with the proposed mechanism.

Cordier et al. [110] have investigated the fuel component segregation by means of the spatial distribution of high- and low-volatile components of different fuels (E00, E20, and E85) at aSOI = 3 ms. To provide a consistent comparison, Figure 3.26 displays the spatial distribution of high- and low-volatile components of E00 at the same domain size. The simulation results of E00, as shown in Figure 3.26, align well with experimental data, where a high proportion of n-undecane appears upstream with a range of 10 to 25 mm away from the injector. Furthermore, the high agreement also appears on the high-volatile fuels, where the majority appears downstream with a range of 30 to 60 mm away from the injector.

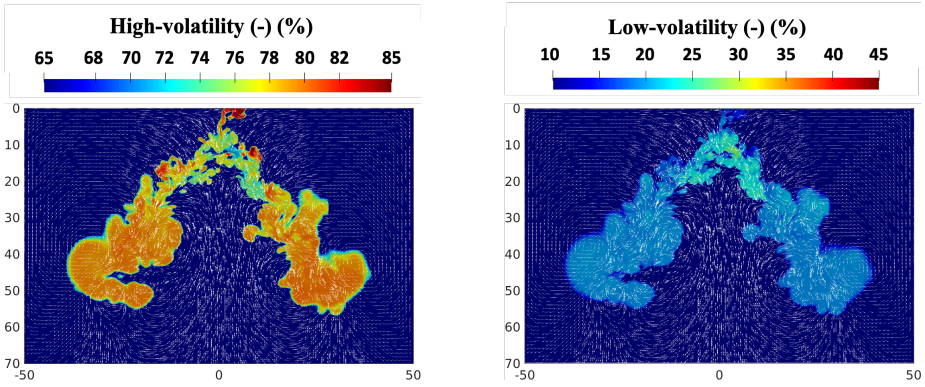

Figure 3.26: Comparison of high- and low-volatile components of E00 at aSOI = 3 ms

3.4 Conclusion

A robust and high-fidelity suite of Lagrangian models for the GDI injector, featuring counter-bore multi-hole configuration, has been proposed and well-validated under several operating conditions from early to late injections within a constant-volume chamber. The findings of this chapter can be summarized as follows:

- The liquid spray, owing to the counter-bore configuration, undergoes primary atomization within the inner-nozzle region, with complete liquid core breakup occurring in the vicinity of the nozzle exit. Consequently, the deformation of liquid droplets becomes significant.
- Significant evaporation can be observed in all early-injection conditions (G3, G3 Cold, and G2 Cold (cold start)). By means of the pressure index (R_p), all conditions do not fall in the boiling regime. G3, due to the low-pressure index, exhibits the highest evaporation contribution.
- The blob method, used as the droplet distribution model, yields satisfactory results in comparisons of global quantities, such as the penetration length in both the liquid and vapor phases. However, assuming that the ejected Lagrangian particles have the size of the injector's inner diameter can lead to delays in droplet breakup and the formation of unphysically sharp spray plume tips in the G3 case. Furthermore, it results in a more dispersed liquid volume fraction (LVF) compared to experimental data.
- Under late-injection conditions with high ambient pressure and temperature (G1), the spray has a more compact plume shape and penetrates less compared with cases under early-injection conditions. Due to high evaporation in the Spray G1 case, the liquid spray signal extinction can be recovered using the droplet distribution model. However, using the blob method, the liquid droplets have a strong evaporation delay, and the liquid spray signal does not disappear.
- Applying a multi-component gasoline surrogate (E00), the heterogenous behavior between high- and low-volatile fuels can be observed in the G1 case. Due to the small density of high-volatile fuels, they evaporate along the spray core and propagate further downstream. On the contrary, low-volatile fuels evaporate only in the vicinity of the spray and are less susceptible to air entrainment, with their majority staying upstream.

4 Spray-wall interaction and wall film development in a constant-volume chamber

Spray morphology in a constant-volume chamber under several engine-like conditions, from early- to late-injection conditions, and the characteristics of different fuels under cold-start and late-injection conditions have been extensively discussed. The proposed suite of Lagrangian models is capable of capturing free spray; however, there is a gap to be filled as spray-wall-flow interaction is the ultimate objective of this thesis.

In real GDI engines, spray-wall interaction and wall film deposit are inevitable as the injection process takes place directly into the combustion chamber. It can be alleviated and even avoided by altering the injection orientation and timing. The ongoing challenge lies in how the GDI engines can achieve homogeneous combustion for cold-start and part-load conditions. Under stratified combustion, the fuel is injected during the compression phase. Given that the wall film and spray-wall interaction may occur on the piston, fuel film would not be easy to develop due to high ambient pressure and temperature.

The examined target in this chapter is a constant-volume chamber simulating a cold-start condition to address the issues and investigate the phenomenon of spray-wall interaction. All the experimental setup and data is provided by ECN [47, 63]. The same injector, “Spray G,” and the constant-volume chamber discussed in Chapter 3 are employed. A 9-component E10 gasoline surrogate (PACE20) is used in this chapter. The details of E10 can be found in Table 3.2. The wall is placed 40 mm downstream from the injector tip. This position is chosen to represent the piston location during injection at −310°CA (310 degree crank angle before compression top center) in a typical GDI engine [10]. The ambient pressure is set up at 0.5 bar to simulate a part-load and cold-start condition, as shown in Table 4.1. As the times of injection and the total injected mass differ from the free spray cases, the corresponding mass flow rate for this section is shown in Figure 4.1

Table 4.1: Essential parameters of the operating conditions

Spray G	Case 1	Case 2
Injection	double injection	double injection
Fuel temperature (K)	293	363
Injection pressure (bar)	200	200
Ambient temperature (K)	293	363
Wall temperature (K)	293	363
Ambient pressure (bar)	0.5	1
Total injected Mass (mg)	20.3	20.3
Injection duration each time (ms)	0.74	0.74
Dwell time (ms)	0.9	0.9

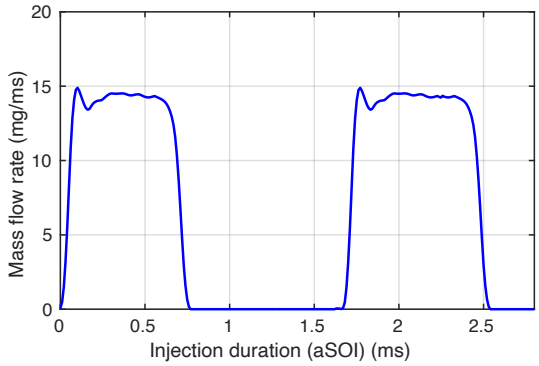

Figure 4.1: Profile of the rate of injection (RoI)

4.1 Numerical and experimental setup

To capture the wall film development and spray-wall interaction, the numerical strategy in this chapter is to apply single-layer cells for wall film calculation, and a spray-wall interaction model from Bai et al. [68]. Furthermore, a computational domain with an exact size of 133 mm of its width and length is utilized to capture the spray splash onset from the wall. A similar setup to the free spray is utilized with the primary and smallest cell size, 1000 and 125 µm, respectively. Therefore, the total number of computational grids is 18 million. Figure 4.2 shows the computational domain and mesh details.

A single layer is marked as red in Figure 4.2. In comparison to the previous mesh setup in Chapter 3, the mesh refinement extends up to 90 mm as the exact size of the

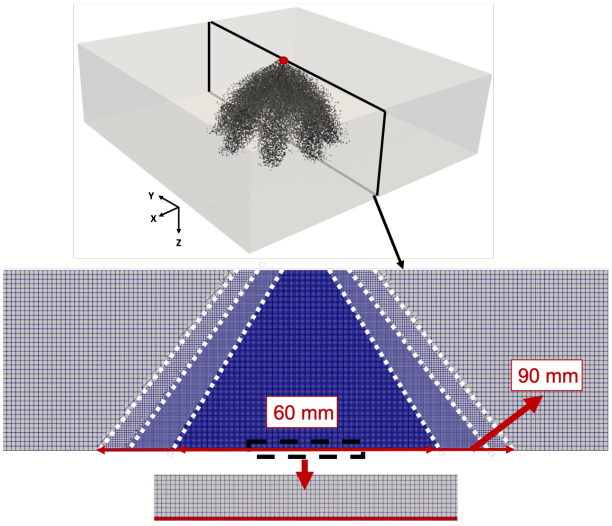

Figure 4.2: The computational domain and mesh details for ECN spray impingement (The center of the injector is set up at the origin of the computational domain, which is marked as a red circle)(note: the white broken line is to outline the mesh refinement)

impingement plate for temperature and wall film thickness measurement. It is to cover the whole evolution of the spray and wall film development.

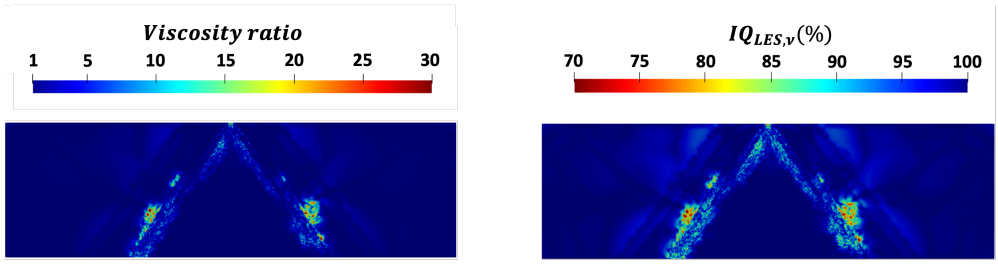

(a) Viscosity ratio ($\frac{\nu_{t,eff}}{\nu}$)

(b) LES quality index ($IQ_{LES,\nu}$)

Figure 4.3: Examining mesh quality at a time after the start of injection (aSOI) = 0.55 ms

The simulation is grid-dependent as the study utilizes Large Eddy Simulation (LES). The mesh quality assessment uses the viscosity ratio proposed by Celik et al. [83] as a criterion for the resolution of LES, described in section 2.1.3. By applying equation (2.18).

In Figure 4.3 (a), the viscosity ratio ($\frac{\nu_{t,eff}}{\nu}$) is employed to weigh the overall viscosity against the molecular viscosity. The ratio reaches unity as the sub-grid model produces no sub-grid viscosity. According to Celik et al.[83], the ratio needs to be lower than 20 to resolve 80 % of the kinetic energy. The presented mesh quality is thus sufficient with a majority of viscosity ratio below 15 and a corresponding examining index around 80 %. Only the transition region of the mesh size yields a relatively large value.

For experimental setup, a spray impingement plate with a temperature-controlled configuration is placed at 40 mm downstream from the injector tip. A 3-D printed liquid circulation is installed within the impingement plate to provide a well-controlled wall temperature. Furthermore, a thermocouple array was positioned with a range of 20 to 35 mm from the plate center. The thermocouple array provides a spatial temperature gradient distribution averaged up to 25 consecutive injections. The details are shown in Figure 4.4.

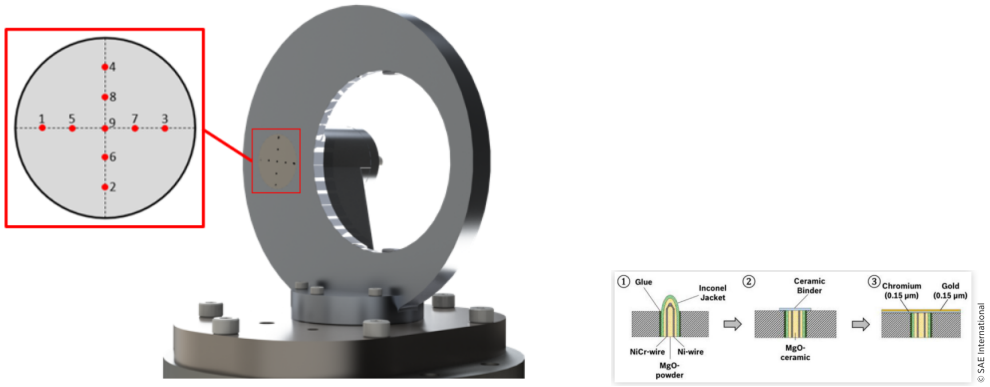

Figure 4.4: Spray impingement plate with a nine thermocouples array. The original images are from Mayer et al. [122]

Furthermore, low-coherence interferometry (LCI) measurement is used for film thickness quantification. The averaged images of wall film thickness are computed using the 150 frames before and the 150 frames after the frame being observed.

4.2 Spray-wall interaction and spray cooling

This section aims to explore and understand the spray-wall interaction and spray cooling during both spray propagation and spray impingement. Figure 4.5 demonstrates the process of the spray-wall interaction with the essential physics behind it.

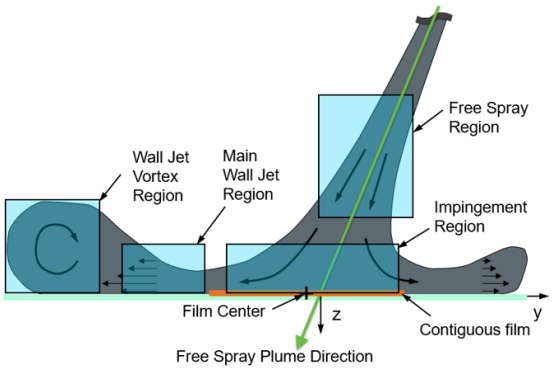

Figure 4.5: Schematic of spray-wall interaction. Original image is from Dhanji et al. [63]

Spray-wall interaction comprises both free spray and spray impingement. Along the spray plume, the spray core can be identified and impacts the fuel film formation. As soon as the spray impinges on the wall, the liquid fuel starts to settle on the wall due to the no-slip static wall and further develops film, labeled as “film center and impingement Region.” Due to wall impingement, the deflected spray retains its momentum from free spray motion and further propagates parallel along the wall, labeled as “main wall jet region.” Subsequently, the wall jet experiences the unbalanced shear contribution from the wall and ambient gas phase and eventually results in the formation of vortices, labeled as “wall jet vortex region.”

Figure 4.6 demonstrates the time evolution spray using a projected liquid volume fraction (red solid line) and a projected mass fraction (contour) to examine if the simulation can well capture these phenomena. Before going directly into the examination, it is worth noting that the free spray formation, encompassing penetration length and PLV images, has been investigated and validated against experimental data from ECN, as described in section 3.2.3. The threshold of the projected mass fraction is set up as 0.05, suggested by ECN.

The time evolution covers only half of the injection duration as the cases in this chapter are set up as double injection with 0.9 ms dwell time. Spray plumes at aSOI = 0.54 ms arrive at the wall, which is aligned with experimental data (aSOI = 0.56 ms) [63]. By only observing the projected mass fraction, the spray core remains intact even at the end of injection (aSOI = 0.72 ms); Furthermore, the liquid plume starts to collapse after aSOI = 1.08 ms.

Interestingly, the main wall jet region can be clearly observed from aSOI = 0.72 ms until 1.26 ms. The near wall jet propagates until 50 mm from the coordinate center and,

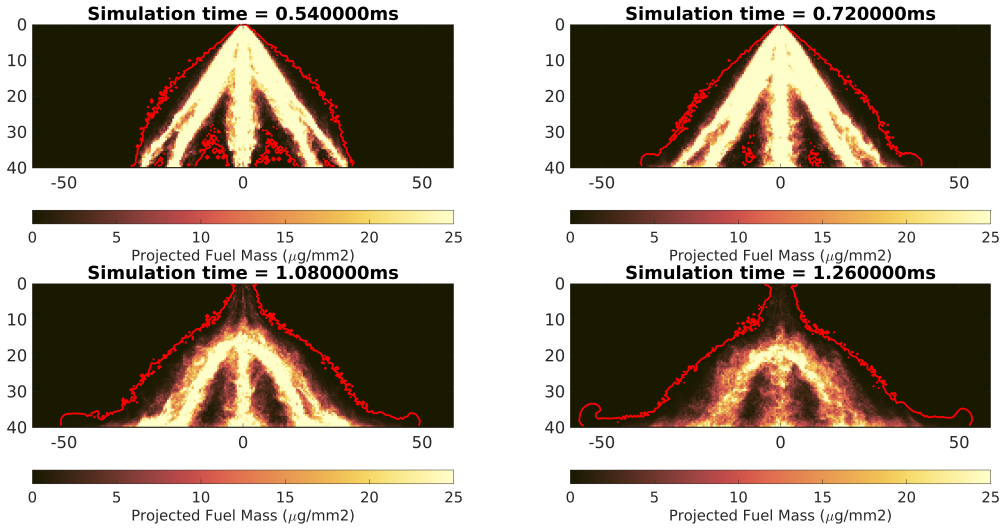

Figure 4.6: Time evolution of spray-wall interaction. (Note: contour: projected mass fraction (Threshold: $0.05\mu g(\text{liquid})/\text{mm}^2$), red solid line: projected volume fraction (Threshold: $0.2 \cdot 10^{-3}\text{mm}^3(\text{liquid})/\text{mm}^2$))

further, transitions to the wall jet vortex region. However, the spray splash phenomenon seems absent only by examining the projected volume and mass fractions. It is likely to occur as the wall and fuel temperature are relatively low at 293 K; this argument is yet convincing unless an examination can quantify and further justify.

Figure 4.7 demonstrates the droplet distribution of the spray-wall interaction regime from Bai et al. [68] by extracting the local droplets at the location 0.5 mm from the impinging wall. The criteria of the spray-wall interaction regimes are described in section 2.2.5. The uncolored regime where the local *We* is greater than the critical Weber number (We_c) is referred to as the splashing regime. The droplets that undergo this regime will induce breakup, and further, the local droplet loses part of its incident kinetic energy and mass.

By investigating the evolution of the local droplets from aSOI = 0.54 to 0.78 ms, more droplets loss their momentum as the local *We* decrease and further cause rebound or develop wall film. In comparison to the time aSOI = 0.54 ms, in which the spray plume starts to impinge on the wall, the local droplets' We_c increases, indicating that the local Ohnesorge number (Oh) increases as We_c is proportional to Oh and inversely proportional to local Laplace number (La). This phenomenon occurs because the impact velocity is high, resulting in an inertial force dominating small droplets after splash onset. This will

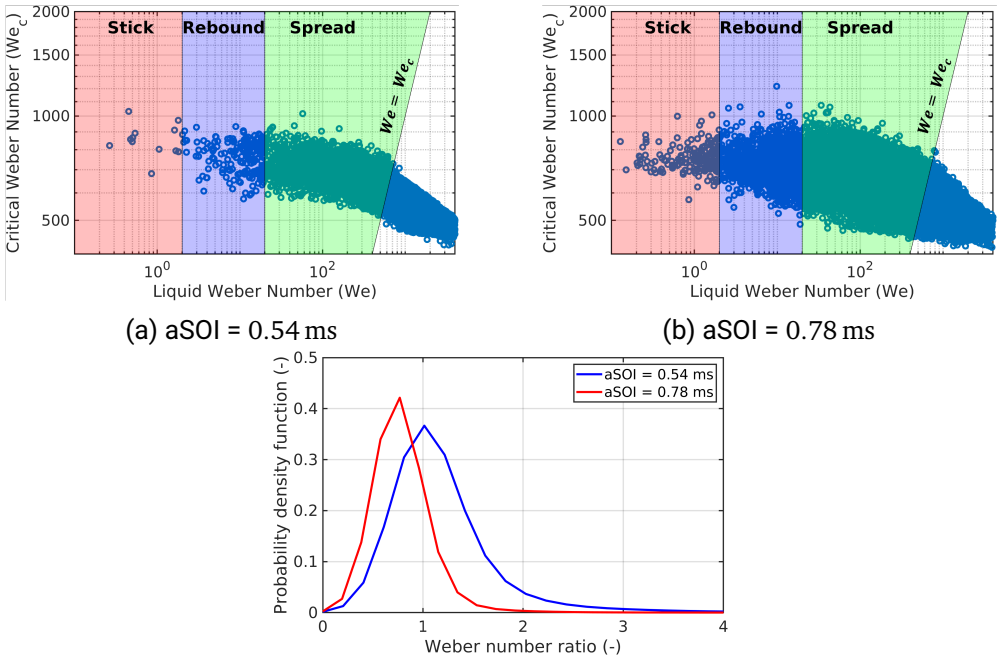

(a) aSOI = 0.54 ms (b) aSOI = 0.78 ms

(c) probability density of the droplets

Figure 4.7: Local droplets undergo the breakup regimes from Bai et al. [68]. (Note: the white region beyond the boundary ($We = We_c$) represents spray splash)

further lead to the breakup or deformation of the small droplets.

To provide a more quantitative comparison of the local liquid droplets' transition. Figure 4.7 (C) further investigates the local Weber ratio (We/We_c) by using the probability density function. The ratio above unity indicates the droplets will undergo the splash regime. At aSOI $= 0.54$ mm, almost half of the overall droplets lie within the splashing regime, whereas the vast majority of the local droplets due to breakup and deformation after splashing reduce their local Weber number at aSOI $= 0.78$ mm.

Spray cooling on the wall and surroundings benefits GDI engines by allowing a higher compression ratio to improve thermal efficiency [8, 12, 123]. Several effects will trigger the occurrence of spray cooling, such as fuel vaporization and convective evaporation. In this case, the spray with high injection pressure is injected into the ambient, which is less than one bar. The fuel then undergoes rapid evaporation, especially for PACE20 containing several high-volatile components, such as n-pentane, cyclopentane, and ethanol. It was investigated in Chapter 3 that approximately 35% of liquid PACE20 fuel evaporates at the

free spray G2 Cold case. Fuel vaporization requires the heat from the ambient to fulfill the threshold of latent heat of vaporization. Furthermore, as the spray plumes arrive at the wall, the accompanied cold ambient vapor and gas cause heat transfer from the wall.

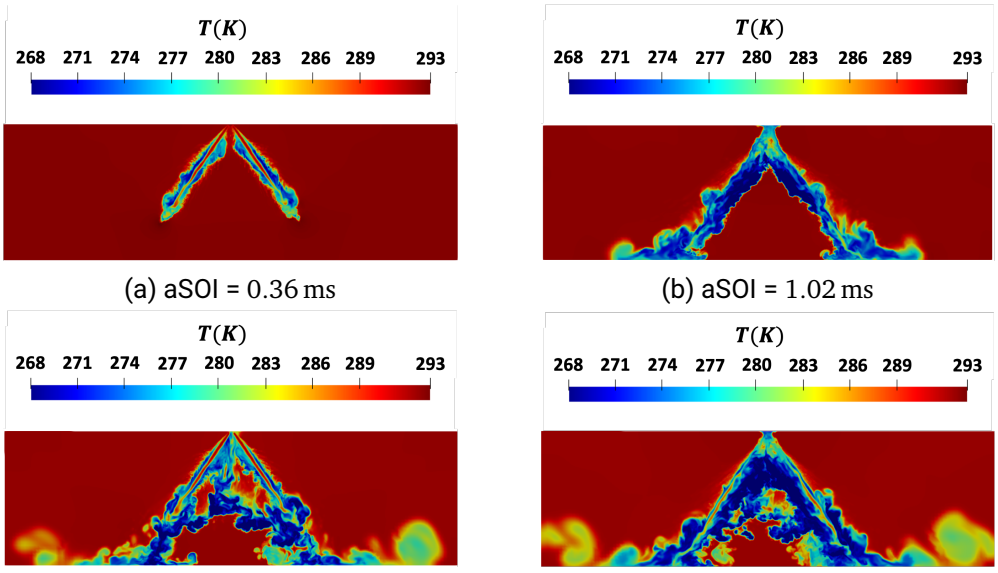

(a) aSOI = 0.36 ms (b) aSOI = 1.02 ms

(c) aSOI = 2.04 ms (d) aSOI = 2.58 ms

Figure 4.8: Time evolution of spatial temperature distribution.

To investigate whether the simulation can reproduce spray cooling, Figure 4.8 demonstrates the time evolution of the spatial temperature distribution covering the whole injection duration. As discussed previously in Table 4.1, each injection duration is 0.74 ms with the dwell time, 0.9 ms. At the first injection before the spray-wall impingement occurs (aSOI = 0.36 ms), spray cooling can be observed in the vicinity of the spray core, whereas the temperature of the spray core remains at approximately its original temperature (293 K). The phenomenon aligns well with the physics of spray cooling due to fuel vaporization. Due to fuel vaporization, spray fuel withdraws the heat from the surrounding ambient and fulfills its latent heat vaporization, leading to a temperature drop.

However, the convection effect is yet intense until the end of the first injection (aSOI = 0.74 ms). During the injection, the momentum is exchanged from the spray to the ambient, leading to air entrainment and increasing air-fuel mixing. This convective effect can be observed at aSOI = 1.02 ms, where the spray starts to detach the injector tip. Due to the loss of spray momentum and the increasing air-fuel mixing, the spray cooling region

expands. Furthermore, the other spray cooling effect induced by the wall impingement can also be observed. As the spray arrives at the wall, the conduction from the wall starts to play a role in the wall film and the fuel vapor near the wall. The combined heat transfer will moderate spray cooling by heating up the cool ambient and fuel vapor, as shown in Figure 4.8 (c) and (d).

To examine how the temperature drops due to spray cooling, a study from Dhanji et al. [63] conducted a 0-D calculation of fuel liquid and vapor under equilibrium states. Due to the air entrainment, the mixture fraction of fuel reduces and causes strong evaporation. By reaching the equilibrium state, the temperature is approximately 272 K and drops up to 20 K from its initial values. This 0-D equilibrium-state calculation shed insight into the relationship between air entrainment and fuel evaporation, resulting in spray cooling. The calculated results also agree with the CFD simulation, as shown in Figure 4.8.

As the spray-wall impingement occurs and the fuel film settles on the wall, those cool air-fuel mixtures will further transfer the heat from the wall, leading to wall cooling. An experimental data of the spatial temperature gradient with a range of 20 to 35 mm from the plate center at aSOI = 1.5 mm facilitates comparison with simulation data, as shown in Figure 4.9.

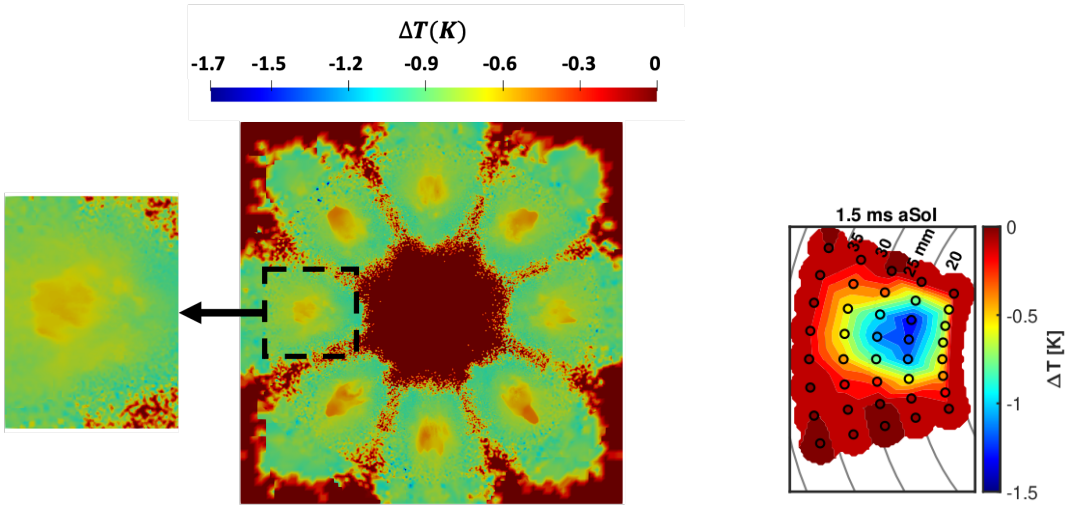

(a) Simulation (b) Experiment

Figure 4.9: Spatial temperature gradient distribution at aSOI = 1.5 ms. The presented temperature gradient is calculated by the difference between the initial temperature and the current temperature on the wall

The effect of spray cooling on the wall can be observed at approximately 1 degree lower than its initial temperature (293 K). The simulation data show underprediction compared with those measured by the thermocouple array. This might be due to the incomplete setup of wall boundary conditions. The current setup is constant temperature, which may yield greater heat transfer than 1-D conjugate heat transfer (CHT).

4.3 Wall film development and evaporation

So far, the efforts have been dedicated to investigating the spray-wall interaction and spray cooling from free spray toward wall impingement. This section focuses on the wall film development in an effort to examine the capability of the spray-wall interaction model employed in this thesis [68] and to understand the evaporation effects of different cases, as shown in Table 4.1.

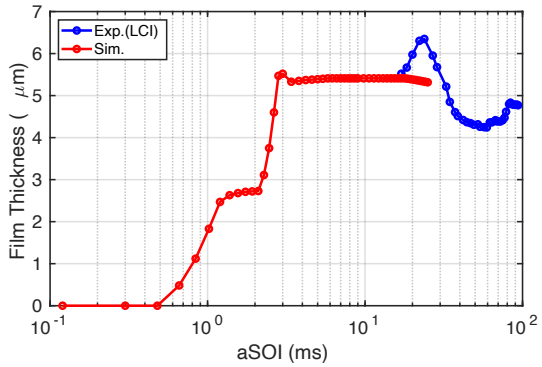

Figure 4.10: Quantitative comparison of the transient averaged film thickness with LCI measurement [63]

Figure 4.10 demonstrates the film thickness evolution with injection time and a comparison with experimental data. The thickness presented is the spatially averaged data of a single plume in a range of 20 to 35 mm from the impingement plate center. The film thickness by the LCI measurement starts at aSOI = 15 ms until 100 ms due to the stabilization of the measured signal from the fuel droplets. Before this time frame, a strong film corrugation causes the signal washout, resulting in insufficient spatial resolution [61, 63]. It is worth noting that the demonstrated case is Case 1, with the wall, ambient, and fuel temperature at 293 K, as detailed in Table 4.1. With a high-temperature setting, the vapor evaporation may impact the accuracy of the film thickness measurement [61].

Approximately at aSOI = 0.54 ms, the fuel film starts to develop. Two-stage film development due to double injection can be observed; furthermore, a significant increase in the film thickness occurs after each injection duration, ranging from aSOI = 0 to 0.74 ms, and from aSOI = 1.64 to 2.38 ms. This is due to the momentum loss of spray droplets and, further, those droplets settle on the wall, causing fuel film accumulation. At approximately aSOI = 3.5 ms, the aggregate film thickness reaches its stability despite minor decay due to evaporation. The average film thickness remains at 5 µm and fits in the range of experimental data. The agreement proves the capability of the spray-wall interaction model [68] used in this thesis.

It is worth noting that the aggregate wall film thickness can lead to bias from the actual wall film deposit as it is averaged spatially, neglecting the local maximum thickness. And yet, that local maximum thickness is likely to cause soot formation and poor fired conditions. Figure 4.11 shows the spatial distribution of the fuel film thickness at aSOI

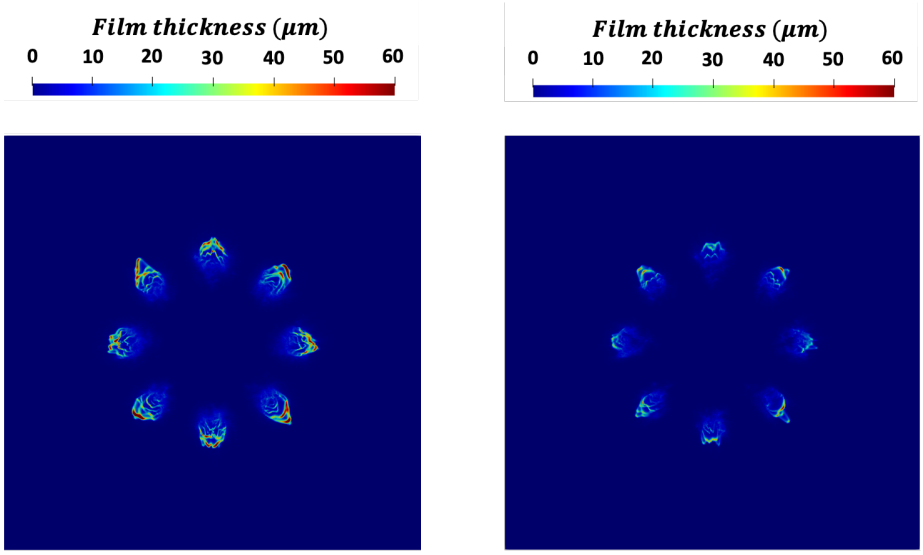

(a) Case 1 (b) Case 2

Figure 4.11: Comparison of film thickness at aSOI = 3 ms. (Note: Case 1: wall, ambient, and fuel temperature are 293 K, Case 2: wall, ambient, and fuel temperature are 363 K)

= 3 ms. It is evident that the maximum thickness is about ten times higher than the aggregate values, even though it occupies only a tiny area. The cause of the fuel film not accumulating homogeneously at the spray impingement center is that spray impinging

on the wall transitions to the wall jet dominated by the near-wall shears. Once the jet loses momentum, it will settle on the wall and develop fuel film.

Case 2, with the wall, ambient, and fuel temperature at 363 K, exhibits a notable drop in the film thickness due to the contribution of evaporation. Employing the pressure ratio (R_p) determining the boiling effect, as described in Table 3.4, the values are 3.53 and 0.62 for Case 1 and 2, respectively. Case 2 lies in the boiling onset regime, whereas Case 1 only has surface evaporation. It also indicates that increasing ambient temperature toward its boiling regime can effectively reduce the fuel film.

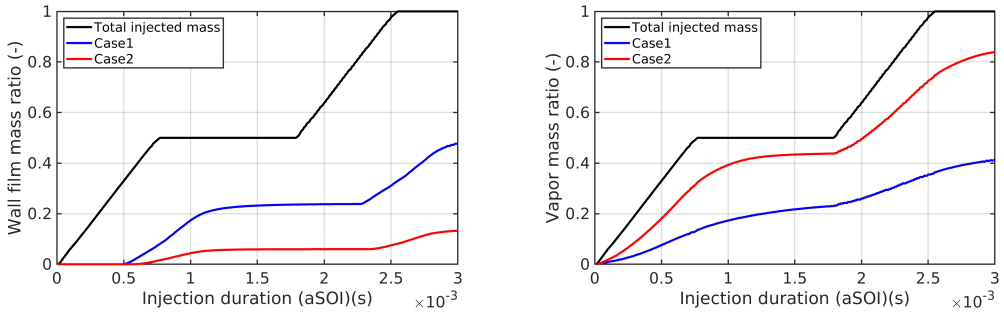

(a) Fuel film mass ratio (b) Vapor mass ratio

Figure 4.12: Comparison of transient fuel mass (mass$_{film}$/mass$_{total}$) and vapor mass ratio (mass$_{vapor}$/mass$_{total}$)

To quantify the evaporation effects, Figure 4.12 demonstrates the transient fuel film and vapor mass ratio, normalized by the total injected fuel mass (20.3 mg), and provides a comparison between the two cases. Case 2, due to reaching its boiling onset, residues less than ten folds of its total injected mass as the film mass during the first injection. On the contrary, for Case 1, there are more than 20% of its total injected mass deposited on the wall, resembling low evaporation contribution. Even at the end of the overall injection, Case 2 contains 80% of its total injected mass as fuel vapor, whereas Case 1 has merely 40% of its total injected mass.

4.4 Conclusion

In this chapter, the proposed suite of models has been further extended to investigate spray-wall interaction within a constant-volume chamber under cold start conditions. It can be concluded as follows:

- The characteristic flow derived from spray-wall interaction, such as the main wall jet region and the wall jet vortex region, can be captured by means of projected liquid volume boundaries.
- The occurrence of the liquid splashing on the wall causes the breakup and deformation of the liquid droplets, resulting in decreasing local *We* number.
- Spray cooling can be observed in both free spray and spray impingement regions. Due to the air-entrainment-induced evaporation, the liquid spray undergoes evaporation and further withdraws heat from the ambient, resulting in spray cooling. Furthermore, the cooled air reaches the impingement wall and causes a wall impingement cooling effect. As the constant temperature boundary is used for heat transfer, the temperature gradient appears to be minor compared with experimental data.
- Wall film thickness from the simulation aligns well with the experimental aggregate data. The evolution of the wall film deposit from the double-injection setup can be captured by the simulation. It can yield a bias by solely comparing the aggregate average film thickness as fuel film tends to accumulate at a small spot influenced by the near-wall jet flow induced by the spray-wall interaction.
- By increasing the temperature of the wall, ambient, and fuel, the film thickness can be effectively reduced, indicating the importance of temperature control during cold start conditions.

5 In-cylinder turbulence and near-wall flow in a GDI engine flow bench[1]

Previously, the spray morphologies of Spray G and its interaction with walls and wall film development within a constant-volume chamber are exclusively discussed. In real engine applications, the in-cylinder flow influences the spray formation and, consequently, may reduce the wall film via convective evaporation. This chapter focuses on in-cylinder turbulence and near-wall flow in an engine flow bench.

The engine flow bench is based on a single-cylinder spray-guided DISI optically accessible engine built at the Technical University of Darmstadt [20–25]. The engine features a pent-roof cylinder head and overhead valves inside a dual-port system to produce a tumble motion within the combustion chamber. The bore and stroke are both 86 mm, and the compression ratio is 8.7. This research engine was designed to provide well-controlled boundary conditions under various operating conditions, from high to part load [124].

Table 5.1: Essential parameters of the targeted engine flow bench

Working fluid	Air
Inlet temperature ($T_{\mathrm{in},2}$) (°C)	22.7
Inlet pressure ($P_{\mathrm{in},2}$) (bar)	1.000
Outlet pressure ($P_{\mathrm{out},2}$)(bar)	0.998
Mass flow rate (100%) ($\dot{m}_{\mathrm{in}}$)(kg/h)	94.10
Reynolds number	32,400

The engine air flow bench aims to reduce the complexity of engine flows and further focus on the physics of the intake flow during the intake phase. Therefore, it operates with its piston removed, which allows an optical plate to be placed on the bottom of the cylinder and an outlet channel to be provided for optical access, such as PIV measurement. The intake valve is fixed at the position of 9.21 mm, which is the valve lift of the motored engine at −270°CA (270 degree crank angle before compression top center), to simulate

[1]This section is partly taken from a publication by Lien et al. [2], which was accomplished during the work on this thesis. In Ref. [2], I was the first author.

the intake flow. Detailed information on the engine flow bench and characterization of the operating conditions have been published by Welch et al. [24]. Figure 5.1 demonstrates the configuration of the engine flow bench.

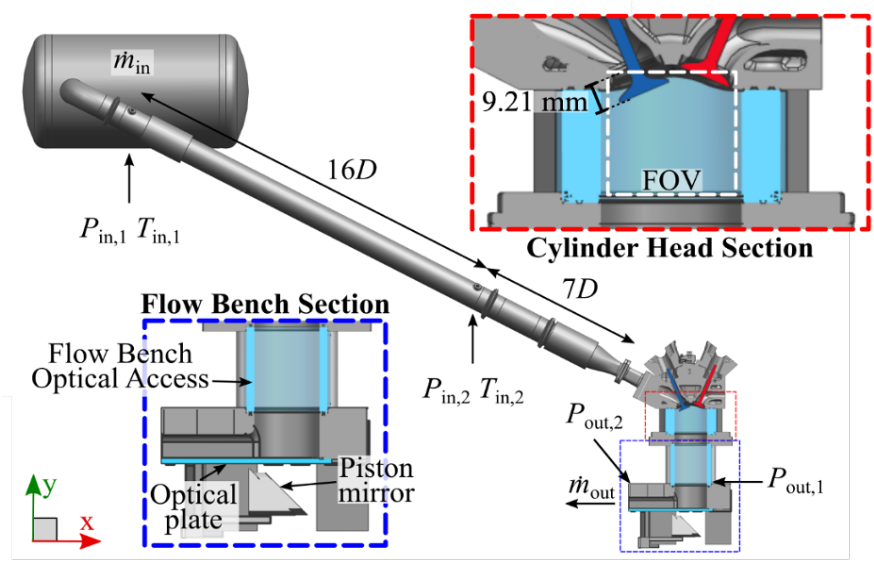

Figure 5.1: Engine flow bench configuration and experimental setup [24]

The air flow bench operates with various mass flow rates (100%, 75%, and 50%), as discussed in Chapter 1. The 100% mass flow rate was set by adjusting the mass flow rate to match the intake velocity of a motored engine at a crank angle -270° CA. The engine speed and intake pressure of the motored engine described here are 800 rpm and 0.95 bar, respectively. This section chooses the 100% mass flow rate, and its corresponding *Re* is 32,400. The *Re* is calculated by applying the corresponding mass flow rates, the intake pipe diameter of 56.3 mm as the characteristic length and dynamic viscosity of $1.83 \cdot 10^{-5}$ kg/ms. [24] Table 5.1 summarizes the relevant boundary conditions of the engine flow bench.

5.1 Engine flow bench numerical setup

Following the experimental configuration of the air flow bench in Figure 5.1, Figure 5.2 shows the computational domain from the side and top views. Its inlet boundary starts from the second inlet measured probe ($P_{in,2}$ and $T_{in,2}$) in Figure 5.1 and its outlet remains

consistent through to the exit channel in the experiment.

Figure 5.2 (b) further represents the target planes (symmetry plane (SP) and valve plane (VP)) for investigation throughout the entire study. The symmetry plane is located at the center of the cylinder with z = 0 mm, whereas the valve plane is located at the center of the intake valve, which is the plane offset 19 mm from the z direction. Due to the axisymmetric layout of the engine flow bench, it is assumed that the intake flow from the two intake ports is identical.

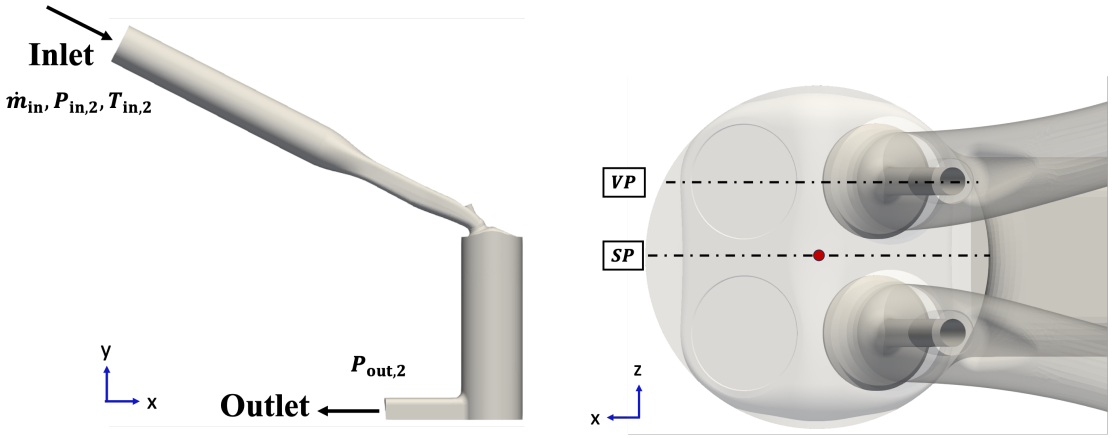

(a) Side view (b) Top view

Figure 5.2: Side and top view of the simulation model. Note: the presented ports are only intake ports as the exhaust valves are closed in this flow bench application, and the two broken lines and the red circle in Figure 5.2 (b) represent the target planes (SP: symmetry plane, VP: valve plane) and the origin of the coordinate, respectively

Figure 5.3 shows the generated mesh near the intake valve, exemplifying the near-wall meshes for LES in the valve region. The meshing strategy is to deliver a hybrid mesh; accordingly, from the near-wall region to the main flow region, there is a pattern of hexahedron-polyhedron-hexahedron grid shapes. This approach aims to alleviate the errors induced by the near-wall mesh transition to the primary mesh. Thus, polyhedral layers must be placed in between. The primary cell size is set at 350 µm. For the near-wall treatment, 15 near-wall cell layers with a growing ratio of 1.05 are placed to resolve the near-wall boundary layer sufficiently, and the cell size nearest to the wall is 12 µm (y^+_{avg} = 0.6). The superscript + refers to quantities that are non-dimensionalized via the viscous length scale $\sigma_v = \mu/u_\tau$, where μ and u_τ are the molecular viscosity and friction

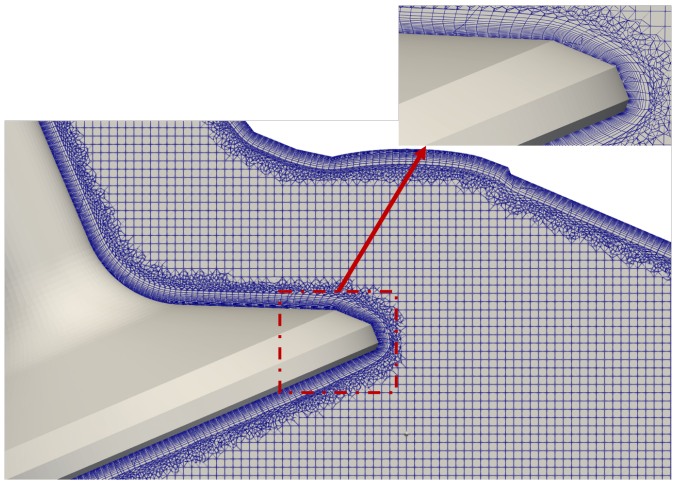

Figure 5.3: Mesh configuration and near-wall meshing strategy of LES

velocity, respectively.

A summary of the relevant mesh parameters is given in Table 5.2.

Table 5.2: Detals of the mesh setup for LES simulation

LES	
Cell number	11 millions
y^+	avg. 0.6
x^+ *and* z^+	avg. 1.0
Boundary layers	15

The following results first present an evaluation of the first-order statistics encompassing the global large-scale motion, in which the time-averaged velocity field ($\overline{u}$) is the main focus, interpreted in the central tumble and the valve planes. Different localities in the two planes are of interest to merit the present investigation, considering the topological difference in the respective flow structure. The second-order statistics accounting for the coherent turbulence structure are then highlighted by illustrating the turbulence kinetic energy turbulence kinetic energy (TKE) and Reynolds stress tensor fields and their associated anisotropy. Based on local flow patterns, such as the valve overflow jet and near-wall flow adjacent to the valves, the resolved coherent turbulence structures are evaluated through anisotropy analysis. Finally, a near-wall flow analysis is performed to describe any non-equilibrium effects in the near-wall region, particularly at the intake

valves and the cylinder liner wall.

5.2 Assessment of large-scale motion

As elucidated by Heywood [125], the instantaneous flow velocity in ICEs can be decomposed into three distinct components: large-scale motion, coherent turbulence structure, and cycle-to-cycle fluctuation. The latter stems from variations in fuel mixture and inherent complexities in the combustion process across different engine cycles. This is not considered in this study.

Large-scale motion represents a first-order time-averaged flow. It encompasses critical flow patterns within the engine cylinder, including the tumble and intake jet flow. This section assesses the capability of LES in capturing the large-scale motion characteristics within an engine flow bench. Through qualitative and quantitative analyses, it aims to comprehensively evaluate the performance of LES against experimental PIV data.

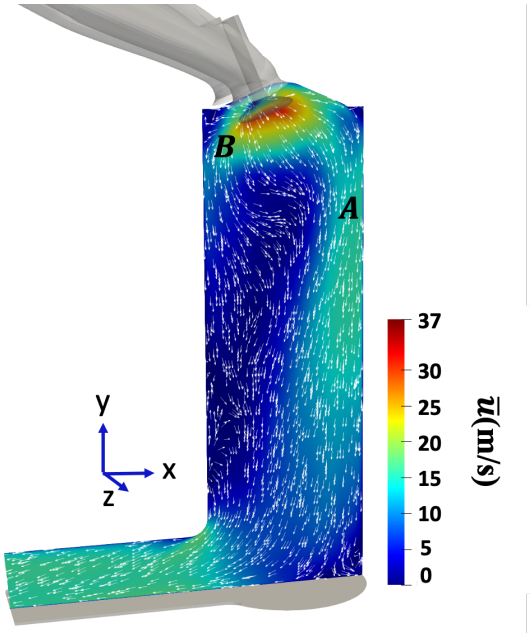

Figure 5.4: Demonstration of crucial physics on symmetry plane (SP) during the intake phase

5.2.1 Symmetry plane

The geometry of the intake valves and ports leads to the generation of the tumble flow within the cylinder, which enhances the fuel-air mixture process. Additionally, due to the axisymmetry of the intake ports, the convergence of the two intake jets within the symmetry plane is observed. The two characteristics are identified as (A) and (B) in Figure 5.4. Interestingly, the counterflow induced by the convergence of the intake jet flows has a much greater velocity than the tumble flow. This phenomenon was discovered by Falkenstein et al. [35], who went on to discuss its impacts on the stability of the tumble flow. However, in the flow bench configuration, the tumble flow (A) does not form a complete tumble motion but rather impinges on the liner wall. It eventually navigates directly toward the flow exit.

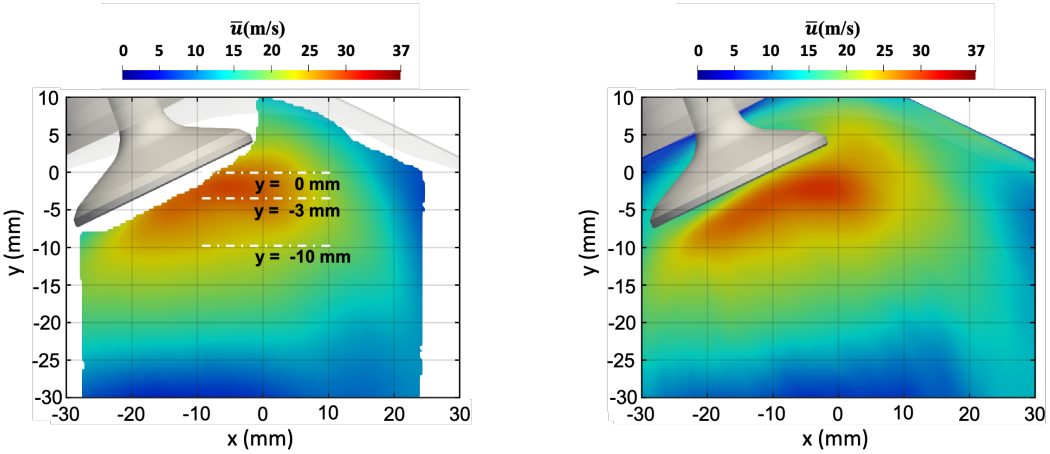

(a) PIV experiment (b) LES

Figure 5.5: Qualitative comparison in the symmetry plane. Note: due to the PIV measurement, the time-averaged mean velocity is ($\overline{u} = \sqrt{\overline{u}_x^2 + \overline{u}_y^2}$) and the broken lines indicate the line profile locations for the quantitative comparison, as illustrated in Figure 5.6

Figure 5.5 shows a qualitative comparison between experimental PIV data and numerical LES data. Since the PIV measurements were performed in a 2-D laser sheet, the time-averaged mean velocity magnitude presented here is determined by the in-plane velocity components ($\overline{u} = \sqrt{\overline{u}_x^2 + \overline{u}_y^2}$). Due to the engine wall constraint, the primary tumble vortex identified as (A) in Figure 5.5 cannot be obtained from PIV. LES captures

not only the overall shape but also the center position of the intake counterflow.

The quantitative comparison is based on measurements taken at specific locations (y = 0, -3 and -10 mm, as depicted in Figure 5.5 (a)) and is displayed in Figure 5.6. As discussed in the previous section, the mass flow rate of this target engine flow bench was chosen by comparing the magnitude of the time-averaged velocity on the symmetry plane, particularly in the vicinity of the intake valves, to those of the motored engine case (800 rpm and 0.95 bar) as outlined in the previous study by Welch et al. [24]. Thus, the time-averaged velocity profiles of the motored case are also included in the comparison. The experimental setup and processing of the motored engine data are comprehensively detailed by Welch et al. [126].

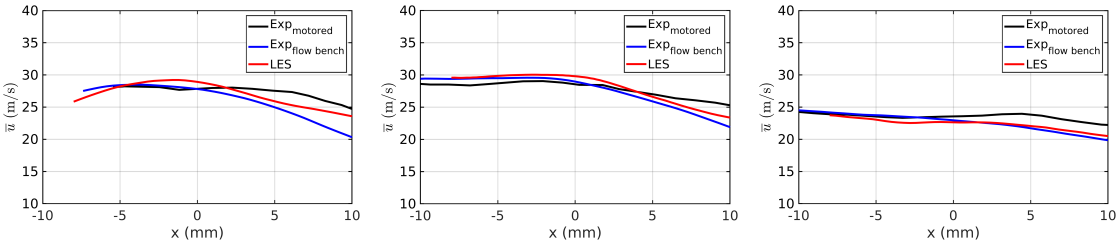

(a) y = 0 mm (b) y = -3 mm (c) y = -10 mm

Figure 5.6: Quantitative comparison of the mean intake velocity profile in the symmetry plane with the location chosen based on the experimental setup [24], as shown in Figure 5.5

In Figure 5.6, a comparison is presented between the time-averaged velocity magnitudes obtained from the experiment and those derived from the numerical simulation. Following the experimental setup, the flow bench under investigation is configured to replicate the velocity profile within the spatial domain, spanning from y = 0 mm to -3 mm and from x = -10 mm to 10 mm. Consequently, it is evident that the LES yields comparable results with both experiments.

5.2.2 Valve plane

According to a study by Buhl et al. [18], the intake flow in the valve plane comprises several physical phenomena from fundamental flows. The most crucial ones are the intake jet flow, the induced vortices from the valve flow separation, and liner wall impingement, labeled (C), (D), and (E) in Figure 5.7, respectively. The intake jet flow (C1) is the main drive during the intake phase inside ICEs. It causes the wall impingement flow (E1) and further generates the tumble flow (A) in the symmetry plane, as shown in Figure 5.4. On

the other hand, due to the constrained layout of the intake valves, the intake jet flow (C2) deviates from resembling the tumble flow but rather hits the liner wall, causing the wall impinging flow (E2).

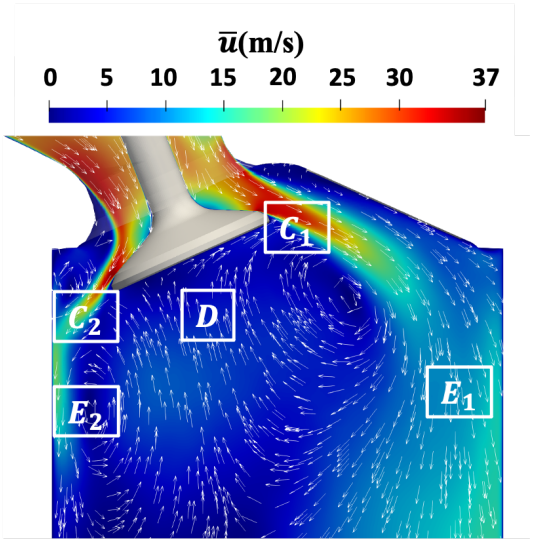

Figure 5.7: Demonstration of crucial physics during the intake phase in the valve plane (VP)

Subsequently, a comparison of the time-averaged intake flow is performed in the valve plane, as illustrated in Figure 5.8. Figure 5.8 (a) and (b) provide a qualitative comparison of the intake flow jet. The flow patterns obtained through numerical simulation and experimental measurements exhibit satisfactory agreements. However, it is noteworthy that the LES results in a relatively narrower shape for the intake flow jet. This divergence could stem from either the inability of the ensemble-averaged PIV data to mitigate the influence of jet flapping [24], or the simulation's incapacity to accurately capture the vortex shedding phenomena. A more comprehensive comparison entails the analysis of the jet centerline trajectory and its velocity to delve deeper into the disparities.

The intake flow jet centerline can be depicted well by extracting the maximum velocity. According to a study by Buhl et al. [18], the sampling location is based on the valve ring edge and extends along the trajectory of the intake flow jet, as shown in Figure 5.9 (a). In Figure 5.9 (b), the coordinate axes have been redefined and adjusted in alignment with the flow direction of the jet and the normal direction of the jet flow, respectively.

Despite the deviations between the experimental and numerical data on the valve jet

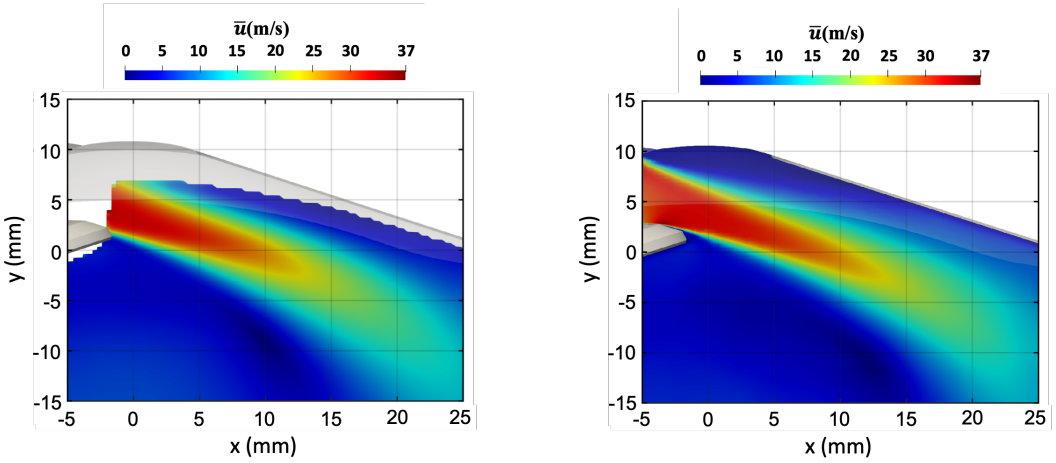

(a) PIV experiment (b) LES

Figure 5.8: Qualitative comparison of the time-averaged velocity of the intake jet in the valve plane

observed in Figure 5.8, Figure 5.9 shows that the jet centerline between the two is highly comparable. The LES applied in this study is proven capable of capturing large-scale motion. Good Agreements are achieved on both the symmetry plane and the valve plane.

5.3 Analysis of the turbulence structure

The previous section undertook a first-order statistical analysis of the intake flow, focusing solely on assessing time-averaged velocity. However, the turbulence structure characterizing the in-cylinder flow is fundamentally derived from Reynolds stresses as opposed to the time-averaged velocity field.

In this section, a second-order statistic analysis is performed. Reynolds stress tensors represent the turbulence structure with its fluctuation velocity. These tensors provide insights into various facets of in-cylinder turbulence, encompassing energy levels, intensity, and the landscape of anisotropic structure. The entirety of this section is dedicated to the examination of these tensors.

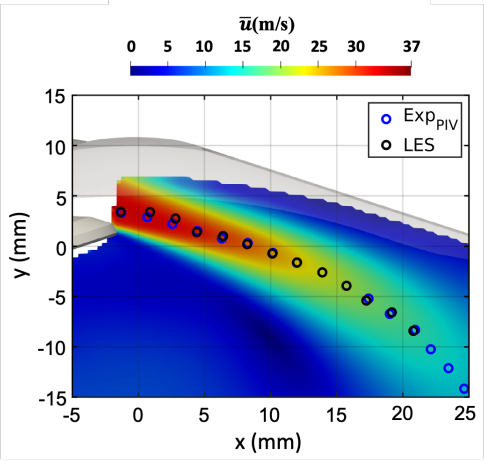

(a) Intake overflow Jet trajectory

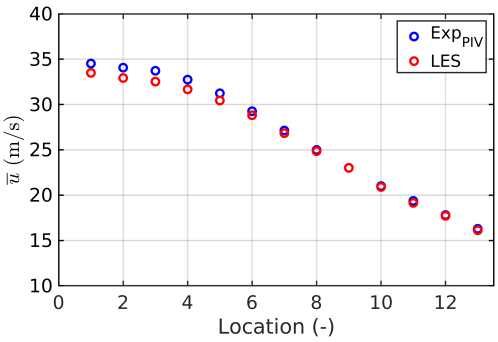

(b) Magnitude of the time-averaged velocity at the intake flow jet centerline

Figure 5.9: Comparison of the intake flow jet centerline. Note: coordinate axis of Figure 5.9 (b) is changed with its location sequence from intake upstream toward downstream.

5.3.1 Turbulent kinetic energy of the intake flow

The second-order Reynolds stress tensors are symmetrical and can thus be categorized as diagonal and off-diagonal [77]. Half of the trace of the diagonal components, called the normal stress components, represents the turbulent kinetic energy (TKE).

$$\text{TKE} = \frac{1}{2} < \overline{u_i' u_i'} > \tag{5.1}$$

where the filtered velocity fluctuation $\overline{u_i'}$ in the LES simulation is calculated each time step by the definition $\widetilde{u_i} = \overline{u}_i + \widetilde{u_i'}$.

The turbulent kinetic energy (TKE) is the examining approach to compare the experimental PIV data and numerical simulation in the valve plane. Due to the planar aspect of the PIV measurement applied in this study, the turbulent kinetic energy (TKE) comparison uses two components (TKE = $\frac{1}{2}(\overline{u_x' u_x'} + \overline{u_y' u_y'})$).

Figure 5.10 highlights a notable phenomenon wherein turbulence within the valve region. This turbulence generation is attributed to flow straining within the intake port, particularly near its walls. The turbulence arises from the separated shear layer originating

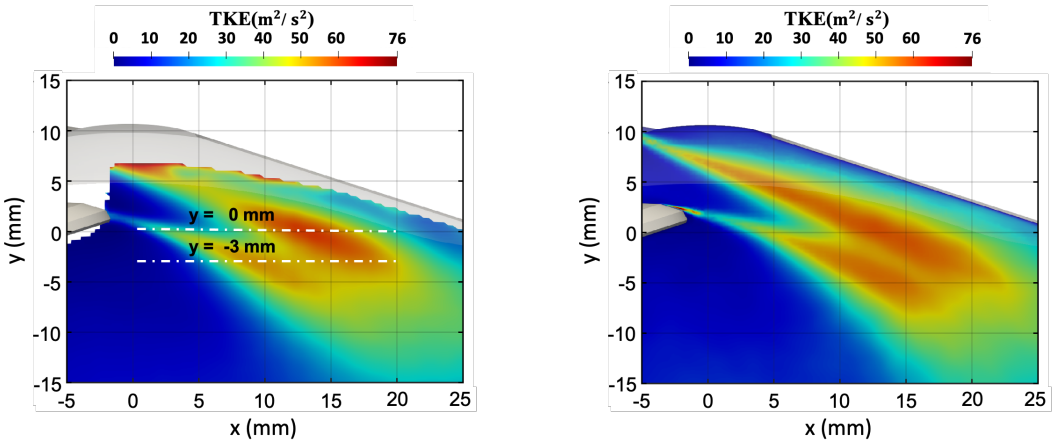

(a) PIV experiment

(b) LES

Figure 5.10: Qualitative comparison of turbulent kinetic energy (TKE) in the valve plane (note: the broken lines indicate the line profiles to be compared in Figure 5.11)

from the valve edge, which experiences a pressure increase due to geometric discontinuity and cross-sectional area expansion. Subsequently, the turbulence merges and appears in a bag shape downstream. The experimental and numerical data align well in terms of shape and intensity.

Figure 5.11 presents a comparison of two specific locations (y = 0 and -3 mm). It reflects the observation in Figure 5.10, in which the two peaks represent the turbulence induced by the intake valve and intake port due to the separating flow. They eventually merge into one, as shown in Figure 5.11 (b). In direct comparison, LES yields slightly overpredicted turbulence when contrasted with the experimental data. It can also be observed in Figure 5.10. Notably, the discrepancies between the experimental and simulated results are more pronounced here than in the time-averaged velocity analysis of the intake flow jet. This divergence may be attributed to the jet-flapping effect discerned in the PIV experiment, as the computation of turbulent kinetic energy relies on velocity fluctuations. Under the same operational conditions as the current examined engine flow bench, the jet-flapping frequency escalates to $752Hz$ [24].

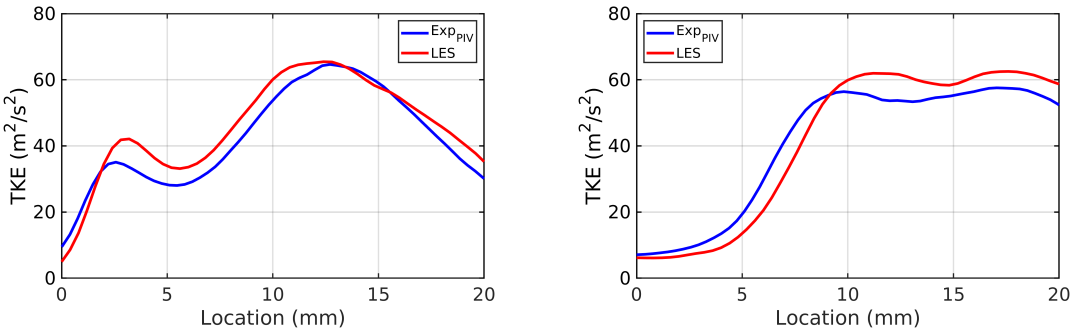

(a) $y = 3mm$ (b) $y = 0mm$

Figure 5.11: Quantitative comparison of turbulent kinetic energy (TKE) in the valve plane

5.3.2 Anisotropic turbulence of the intake flow

As elaborated upon in this section, Reynolds stress tensors exhibit both diagonal and off-diagonal components. The former, termed normal stress, has been the focus of comparison thus far. In the subsequent part of this section, the discussion will focus on the latter, represented as shear stress.

Off-diagonal components intensify the discrepancies between diagonal components, thus reinforcing turbulence anisotropy. In essence, the intrinsic difference between normal and shear stress lies in their impact on anisotropy intensity, either diminishing or augmenting it. In particular, shear stress is prevalent in confined domains, such as ICEs, which are subject to increased turbulence structure deformation.

The anisotropic phenomenon of the underlying in-cylinder turbulence will be examined in this section. The anisotropic tensor derived by the Reynolds stress tensor reads:

$$b_{ij} = \frac{\overline{u_i' u_j'}}{\overline{u_i' u_i'}} - \frac{\delta_{ij}}{3} \tag{5.2}$$

The anisotropic tensor or the shear stress from the Reynolds stress tensor can distort the turbulence. It can change from spherical isotropic turbulence to a cigar- or pancake-like shape according to the number of prevailing components from the anisotropic tensor. Figure 5.12 illustrates the so-called “turbulence anisotropy invariant map”, where the possible states of turbulence are categorized based on two anisotropic invariants ξ and η [127–129].

These two invariants are defined as follows:

$$\mathrm{I} = 0.0 \quad \mathrm{II} = -\frac{b_{ij}b_{ji}}{2} \quad \mathrm{III} = \frac{b_{ij}b_{jk}b_{ki}}{3} \tag{5.3}$$

$$\xi^3 = \frac{\mathrm{III}}{2} \quad \eta^2 = \frac{-\mathrm{II}}{3}. \tag{5.4}$$

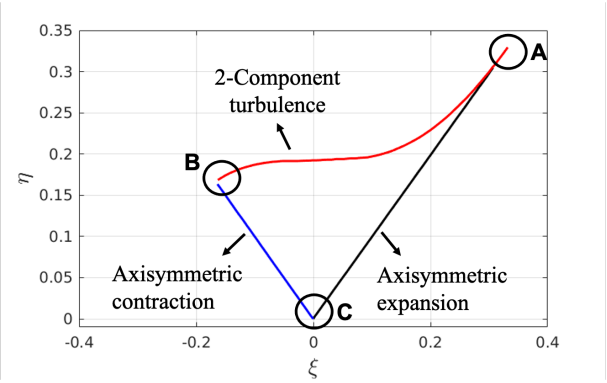

Figure 5.12: Turbulence anisotropy invariant map outlining the possible states of turbulence [129]

The entire spectrum of potential turbulence states resides within the confines of the invariant map and aligns with its boundaries, as shown in Figure 5.12. These states are categorized as 1C, 2C, and 3C; namely, one-component turbulence, two-component isotropic turbulence, and three-component isotropic turbulence, respectively. The boundaries delineating states 3C and 1C, as well as states 3C and 2C, are categorized as axisymmetric expansion and contraction, respectively. The curve linking the 2C and 1C states denotes the two-component anisotropic turbulence. In this state, the suppression of one component signifies the flow condition prevalent in close proximity to the wall [77, 129]. As the anisotropic tensor represents the shear stress of the turbulence, the state of two-component anisotropic turbulence exhibits the highest anisotropic intensity. This observation is supported by the application of anisotropic turbulence intensity F, derived from the three principal invariants of the anisotropic tensor, as shown in equation (5.3) [129]. The definition of the intensity of anisotropic turbulence F is:

$$\mathrm{F} = 1 + 27\mathrm{III} + 9\mathrm{II}. \tag{5.5}$$

By evaluating the anisotropic tensors and two invariants (ξ and η), a comprehensive understanding of in-cylinder anisotropic turbulence is attainable for both the symmetry

and valve planes. The study focuses on the spatial domain, ranging from x = -33 mm to x = 33 mm and y = -10 mm to y = -45 mm. The data collected from each computational cell converge within the invariant map (η vs. ξ), as illustrated in Figure 5.13. Moreover, this visualization employs three iso-lines, delineating anisotropic intensity values of 0.6, 0.85, and 0.98, to facilitate better understanding. The anisotropic intensity (F) ranges from 0 to 1, indicating a spectrum from two-component anisotropic turbulence to three-component isotropic turbulence 3C.

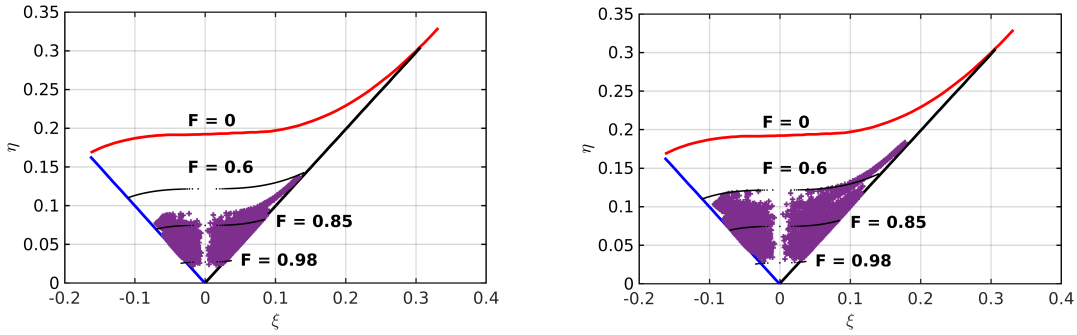

(a) Symmetry plane

(b) Valve plane

Figure 5.13: In-cylinder turbulence representation within the anisotropy invariant map in both the symmetry and valve planes, ranging from x = -33 to x = 33 mm and y = -10 to y = -45 mm

As depicted in Figure 5.13, the in-cylinder turbulence within both the symmetry and valve planes primarily occupies regions close to the three-component isotropic state. Notably, this distribution lies axisymmetrically along the plane-strain limit, depicted as the broken line in Figure 5.12. Interestingly, no points fall within this region. Based the definition of ξ in Equations (5.3) and (5.4), within this region, ξ appears to be zero, implying that at least one anisotropic tensor is zero. When it occurs, the turbulence is influenced strictly by specific directions. This phenomenon is scarcely observed in complex wall-bounded flows, such as engine flows. In contrast, the turbulence within both planes is significantly influenced by shear stress components in all directions.

By applying three anisotropic intensity boundaries (F = 0.6, 0.85, and 0.98), it becomes evident that the vast majority of the turbulence lies within a threshold $F \geq 0.6$. This observation aligns with the notion that anisotropic turbulence predominantly arises in regions with obstacles or walls. As previously discussed, anisotropic turbulence is generated and determined by the shear stress. Its intensity will deteriorate when confronted with a positive pressure gradient following the flow expansion from the intake port into

the cylinder.

While the turbulence behavior within the symmetry and valve planes exhibits qualitative similarity, the turbulence in the valve plane displays a slightly more pronounced inclination towards anisotropic expansion compared to the symmetry plane. This dissimilarity may be attributed to the influence of the intake jet. In contrast, the turbulence state in the symmetry plane undergoes a quantitatively weaker anisotropic level with an F threshold value between 0.85 and 0.98.

The orientation of in-cylinder turbulence is comprehensively explored and compared in Figure 5.13. However, a detailed comprehension of the spatial distribution of each turbulence state in both the symmetry and the valve planes is required. To achieve this, a categorization strategy as outlined by Zengraf et al. [26] is employed, utilizing two invariants, II and III, as demonstrated in equation 7. This approach allows for the replication of the spatial distribution of the turbulent states, as depicted in Figure 5.14.

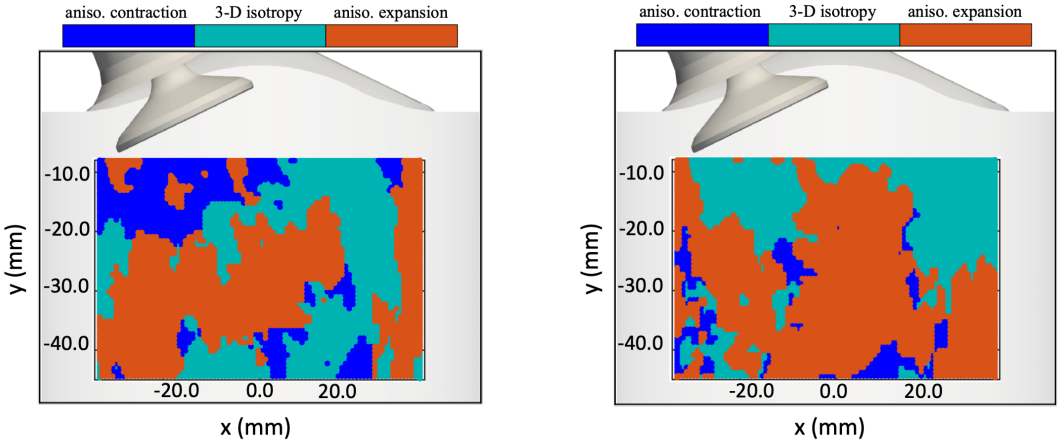

(a) Symmetry plane

(b) Valve plane

Figure 5.14: Spatial distribution of the turbulent state in both the symmetry and valve planes. Note: red: anisotropic expansion, blue: anisotropic contraction, green: three-component isotropic turbulence

Figure 5.14 outlines the spatial distribution of the turbulence states in both the symmetry and valve planes. The result offers some insights into the turbulence structure based on its local characteristic flow pattern. In the symmetry plane, the dominant features of in-cylinder turbulence encompass anisotropic expansion and isotropy. However, a notable inclination towards anisotropic expansion is evident within the region, spanning from x

= 25 mm to x = 33 mm, as shown in Figure 5.14 (a). This occurrence is attributed to the primary tumble flow, elaborated upon in the previous section and shown in Figure 5.4.

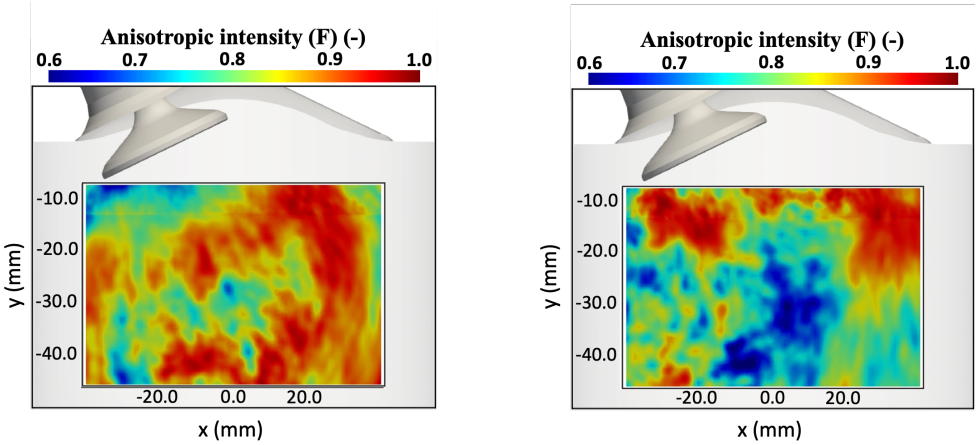

(a) Symmetry plane

(b) Valve plane

Figure 5.15: Spatial distribution of the anisotropic intensity (F) in both the symmetry and valve planes. Note: legend scale exhibits from 0.6 to 1.0

In contrast, the turbulence structure in the valve plane is characterized exclusively by anisotropic expansion. With a valve plane width of 76 mm, it is worth noting that from the axis center at x = 0, the left and right extents are situated at x = -38 mm and x = 38 mm, respectively. Therefore, the spatial distribution of the turbulence state with its width of 66 mm closely aligns with the intake flow jet, identified as (C1) and (C2) in Figure 5.7. The turbulence structure influenced by the intake flow jet (C2) displays anisotropic expansion in the valve plane, ranging from x = -33 to -25 mm and y = -20 to -10 mm. A similar finding also appears at x = 20 to 33 mm, affected by the intake flow jet (C1). The spatial distribution of anisotropic intensity F is also considered in both planes for further exploration. This distribution is depicted in Figure 5.15, offering an additional layer of insight for an in-depth investigation.

The spatial distribution of the anisotropic intensity F shows a relationship between it and the characteristic turbulence states. First, no results reach the actual three-component isotropic state (F = 1, and η and ξ = 0). This finding agrees with the turbulence anisotropy data within the invariant triangle shown in Figure 5.13. As can be seen in Figure 5.15, the three-component isotropy state displayed in Figure 5.14 lies mainly in the region where the anisotropic intensity F exceeds the value of 0.85. According to the definition

of the 3-component isotropy state from Zengraf et al.[26], the in-cylinder turbulence is classified as isotropy when the principal invariant (II) is greater than a constant value of -0.02. The threshold (II > -0.02) lies within a range of the anisotropy intensity F between 0.8 and 0.85 as the anisotropy intensity F does not appear as a straight line within the anisotropy invariant map. This clarifies the phenomenon that excessive points within the 3C isotropy state, as shown in Figure 5.14, are still inside the invariant map. In essence, the three-component isotropy state (3C) ever really existing in real applications, such as wind turbines, ICEs, and even atmospheric flow, have been discussed and explored extensively [130–132].

While the disparity of the 3C isotropic state has been resolved, Figure 5.15 cannot identify the specific regions of anisotropic expansion and contraction. This is because both states are determined by the orientation of the turbulent eddy rather than by the anisotropic intensity. However, in Figure 5.15, certain regions exhibiting high anisotropic intensity can be regarded as anisotropic expansion by using Figure 5.14 as reference, particularly in the valve plane. This phenomenon aligns with the observations made in the invariant map, as shown in Figure 5.13.

5.4 Characteristics of intake jet

Apart from investigating the in-cylinder flow and its associated turbulence, the following research focuses on the intake jet and its near-wall anisotropic turbulence close to the valve wall. The first step is ascertaining whether the intake flow jet exhibits any free shear jet flow characteristics. Pope [77] shares a thorough investigation of Reynolds stress tensors on a free shear jet. Some characteristics can be outlined here.

- Free shear jet is self-similar.
- Reynolds stress of the free shear jet displays a significant level of anisotropy; both normal and shear stress components contribute to the overall behavior of the jet.
- Jet centerline exhibits the lowest local turbulence intensity.
- The turbulent wake formed behind the jet is axisymmetric but deviates from the jet centerline.

Pope [77] identifies the turbulent jet as self-similar based on several empirical observations. One of these observations is that the normalized velocity profile $\overline{u}(\delta)/\overline{u}_0$ exhibits uniform behavior along the centerline of the jet in each section. $\overline{u}_0$ is the time-average velocity at the jet centerline.

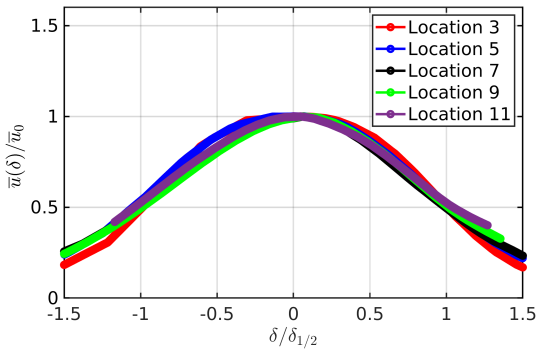

Figure 5.16: Time-averaged velocity profiles of a cross-section of the jet centerline at several locations. Note: the section index follows the examined points from the upstream intake jet toward the downstream, as shown in Figure 5.9 (b). The normalized length ($\delta_{1/2}$) is the distance between the jet centerline and the location of half of the maximum velocity ($\overline{u}(\delta)/\overline{u}_0$ = 0.5)

Figure 5.16 presents five distinct sections (section width 10 mm) situated along the jet centerline at various positions. The location of each section is normalized by the length ($\delta_{1/2}$) defined as the distance between the jet centerline and the location of half of the maximum velocity ($\overline{u}(\delta)/\overline{u}_0 = 0.5$), following the description by Pope [77]. Due to the semi-axisymmetry of the intake flow jet, both sides apart from the jet centerline are normalized by their own value. Figure 5.16 reveals that the intake valve jet is self-similar from upstream toward downstream, although the intake jet structure becomes increasingly dispersed at the jet downstream, shown in Figure 5.9 (a).

To delve into the additional attributes of the aforementioned free shear jet, several aspects, including turbulent kinetic energy (TKE), turbulence intensity (I), and intensity of anisotropic turbulence (F), are investigated. The definition of turbulence intensity (I) by Pope [77] exhibits:

$$I = \frac{\overline{u'}}{\overline{u}}. \tag{5.6}$$

where $\overline{u'} = \sqrt{\frac{2}{3}\text{TKE}}$ and $\overline{u}$ is the time-averaged velocity magnitude.

In Figure 5.17 (a) and (c), it can be observed that the wake of the intake jet demonstrates axisymmetric behavior, although it may not be as pronounced as in a free shear jet. Additionally, the intake jet centerline exhibits the lowest local turbulence intensity, as depicted in Figure 5.17 (a) and (b). This observation is consistent with the positioning of

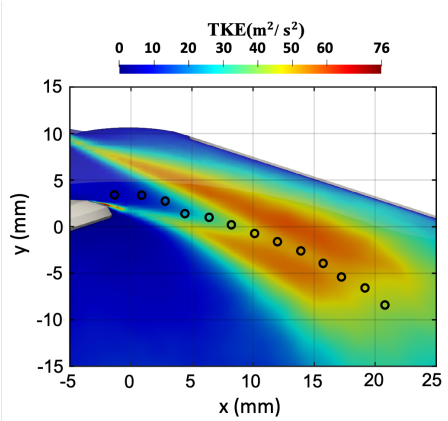

(a) Valve jet centerline trajectory within the TKE spatial distribution

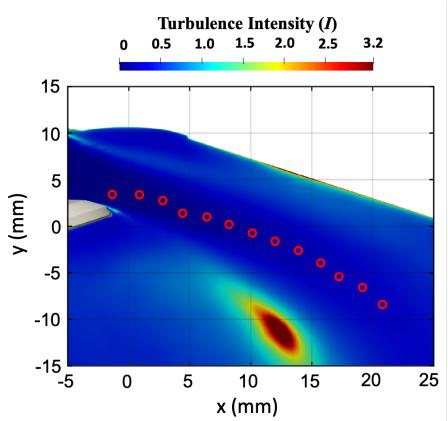

(b) Valve jet centerline trajectory within the turbulence intensity (I) spatial distribution

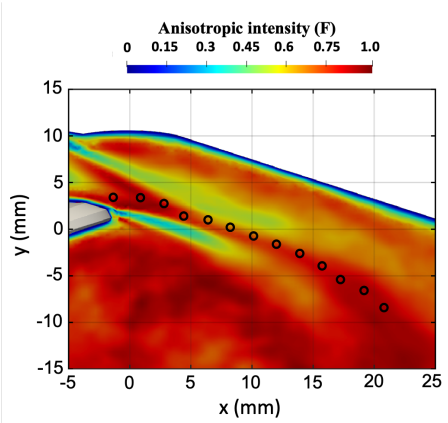

(c) Valve jet centerline trajectory within the turbulence anisotropy intensity (F) spatial distribution

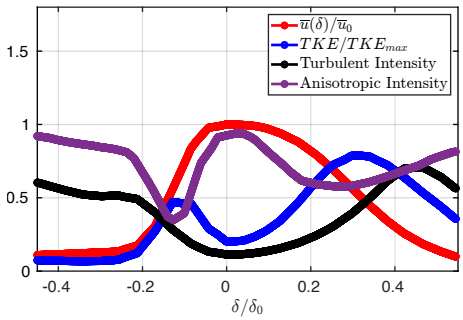

(d) Profiles of time-averaged flow and turbulence structure across the valve jet at location 5, as depicted in Figure 5.9 (b), with index number counting from upstream to downstream

Figure 5.17: Turbulence structure of the intake jet centerline. Note: δ represents the cross-section length of 10 mm, and the jet centerline is located at $\delta/\delta_0 = 0$

the jet centerline between the turbulent wake generated by the intake valves and intake port. The same pattern is evident in anisotropy intensity (F), as shown in Figure 5.17 (c).

To provide a complete investigation of the axisymmetric wake of the intake jet, a cross-section region of the jet centerline has been deployed, shown in Figure 5.17 (d). The cross-section has an overall length (δ_0) of 10 mm, and the span of the cross-section, denoted as δ, is normalized by the length d. Notably, the location $\delta/\delta_0 = 0$ corresponds to the jet centerline. The profiles presented in Figure 5.17 (d) support the notion that the intake flow jet features axisymmetric wakes. Within this context, the focal point of the intake flow jet demonstrates the lowest turbulence intensity (I) and turbulent kinetic energy (TKE), while experiencing the highest value of anisotropic turbulence intensity (F). Away from the jet centerline, both turbulence intensity (I) and turbulent kinetic energy (TKE) increase, accompanied by a reduction in anisotropic turbulence intensity (F). Interestingly, the behavior of the intake valve jet exhibits some compatibility with the turbulence characteristics of a free shear jet, as previously outlined.

As elucidated by Choi and Lumley [127, 129], and reiterated earlier, regions affected by strong shear stress, such as areas with obstacles and walls, tend to exhibit anisotropic turbulence. While efforts have been dedicated to examining turbulence along the jet centerline, it is crucial to investigate the near-wall region. In this region, the turbulence state closest to the wall transitions from the two-component anisotropic turbulence, featuring the highest anisotropic turbulent intensity, toward the invariant map interior region approaching the one-component turbulence (1C). Subsequently, the turbulence state progresses closer to the invariant map boundary, denoting the anisotropic axisymmetric expansion. Figure 5.18 exemplifies the anisotropic turbulence state trajectory of a canonical pipe flow, ranging from $y^+ < 1$ to the center of the turbulent mixing layer [133]. Anisotropic turbulence intensity decreases along with the location from the wall to the pipe centerline. Considering that pipe flow possesses its characteristic flow direction, the orientation of turbulence aligns closely with axisymmetric expansion. Despite the substantial decay in anisotropic turbulence intensity, the turbulence in pipe flow has yet to attain the state of three-component isotropic turbulence (3C).

Figure 5.19 (a) displays the anisotropy trajectory within the invariant map at the location, crossing the near-wall boundary layer and further, extending up to $y^+ = 300$. The trajectory starts from a two-component anisotropic turbulence state and advances toward the axisymmetric expansion. This behavior aligns with the pipe flow data presented in Figure 5.18, particularly in near-wall regions. However, the trajectory subsequently moves away from axisymmetric expansion into the interior of the anisotropic invariant map before eventually returning to it. Notably, as the trajectory returns, its anisotropic intensity increases. This phenomenon can be attributed to the presence of a thin near-wall boundary layer, induced by intake turbulence originating from the intake valve and intake

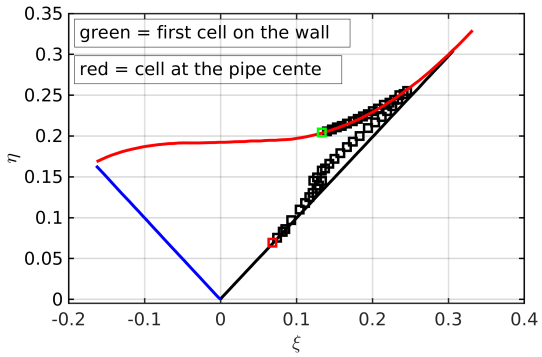

Figure 5.18: Near-wall DNS channel flow data plotted within anisotropy invariant map [133]. Note: Green square represents the first cell on the wall with $y^+ < 1$ whereas the red square represents the centerline of the pipe flow

port. For a more thorough comprehension of this phenomenon, extracting the diagonal Reynolds stress, as per the definition of the turbulence regime, can provide valuable insights.

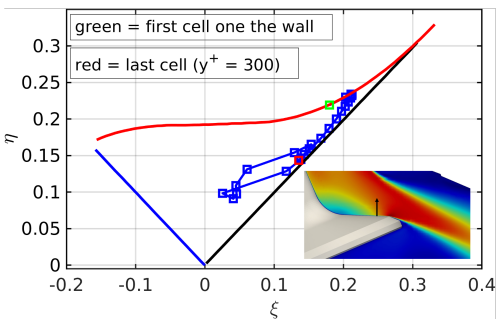

(a) Anisotropy trajectory within the invariant map at the intake valve wall (up to $y^+ = 300$).

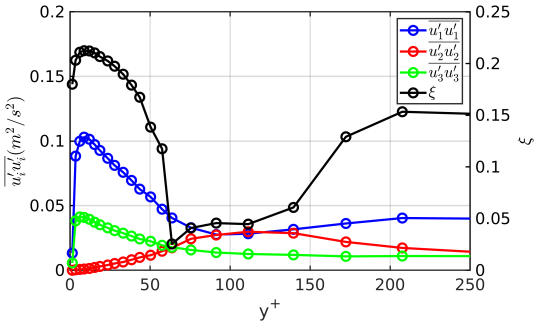

(b) Profiles of the diagonal Reynolds stress components and anisotropy invariant ξ plotted from the wall at the cross-section depicted above in Figure 5.19 (a). Note: $u_2^{'}$ is the wall-normal direction and $u_1^{'}$ is the streamwise direction.

Figure 5.19: Near-wall anisotropy trajectory within the anisotropic invariant map at the intake valve

Figure 5.19 (b) exhibits the near-wall profile of diagonal Reynolds stress and the

corresponding invariant ξ, covering the near-wall region $y^+ = 250$, as depicted in Figure 5.19 (a). Due to increased turbulence production and the dominance of the Reynolds stress component in the main flow direction, the anisotropic trajectory transitions from the two-component anisotropic turbulence state (indicated by the upper curved boundary of the invariant map) to an axisymmetric expansion. However, it is evident that the near-wall flow behavior on the valve is distinctly different than that of canonical channel flow. Due to complex geometry, the turbulence production of spanwise direction is also prominent. In the wall distance range of $y^+ = 50$ to 150, the generation of the wall-normal Reynolds stress component becomes appropriately pronounced. Consequently, the anisotropy trajectory briefly shifts towards anisotropic axisymmetric contraction. This phenomenon implies that the near-wall turbulence within the range from $y^+ = 50$ to 150 is already influenced by the free stream turbulence, underscoring the absence of the near-wall log law commonly observed in engine flow [33].

5.5 Analysis of near-wall non-equilibrium effects

Near-wall treatments for ICEs application have received great attention over the past decade. Studies by DNS [134] and Large Eddy Simulation (LES) [19, 31] clearly show that the characteristics of the near-wall flow inside ICEs deviate significantly from the equilibrium conditions. The relevant non-equilibrium effects are characterized by the following factors:

- Influence of the wall-tangential pressure gradient.
- Wall boundary-layer flow is not always wall-parallel.
- Combustion and mixture formation occur within the wall boundary layer.
- Wall boundary-layer flow is not quasi-steady.

According to the boundary-layer theory based on canonical flows [135], the spanwise components (direction perpendicular to streamwise components) within the near-wall boundary layer are much smaller than streamwise and wall-normal components.

However, under complex geometry, such as ICEs, the direction of the flow is not as apparent as the canonical channel flow. It is also discussed in the previous section that the near-wall spanwise component in ICEs, such as in the intake valve region, behaves distinctively from that in the case of channel flows. Following several studies based on the 2-D Navier-Stokes equation, developing a wall function accounting for the non-equilibrium near-wall effects, consider the wall-tangential direction [136, 137].

All the effects above can be described in the 2-D Navier-Stokes equation below:

$$\frac{\partial}{\partial t}((\mu+\mu_t)\frac{\partial u}{\partial y}) = \underbrace{\frac{\partial \rho u}{\partial t}}_{(d)} + \underbrace{\frac{\partial(\rho uu)}{\partial x} + \frac{\partial(\rho vu)}{\partial y}}_{(b)} + \underbrace{\frac{\partial p}{\partial x}}_{(a)} + \underbrace{\rho f}_{(c)} \tag{5.7}$$

In this study, an engine flow bench operates under a stationary state, and combustion and fuel mixture are not involved. Therefore, the flow within an engine flow bench is in a quasi-steady state. The non-equilibrium factors, including combustion and fuel-air mixing and unsteady effect, are neglected despite their contributions. Equation 5.7 can be rewritten as:

$$\frac{\partial}{\partial y}((\mu+\mu_t)\frac{\partial \overline{u}}{\partial y}) = \underbrace{\frac{\partial(\rho\overline{uu})}{\partial x} + \frac{\partial(\rho\overline{uv})}{\partial y}}_{(b)} + \underbrace{\frac{\partial \overline{p}}{\partial x}}_{(a)} \tag{5.8}$$

where $\overline{(.)}$ denotes time-averaged operator.

According to studies by Popovac et al. [137] and Li et al. [136], the wall-tangential pressure gradient remains independent of the wall-normal direction (y). Moreover, the convective term is zero at the wall and yet behaves linearly from the wall. Equation 5.8 can be integrated over the wall-normal distance (y). It reads

$$[(\mu+\mu_t)\frac{\partial \overline{u}}{\partial y}]_y - \tau_w = [\frac{1}{2}(\frac{\partial(\rho\overline{uu})}{\partial x} + \frac{\partial(\rho\overline{uv})}{\partial y}) + \frac{\partial \overline{p}}{\partial x}]_y y \tag{5.9}$$

Integration of Equation (5.9) allows the derivation of the time-averaged wall-tangential velocity profile ($\overline{u}(y)$) within the viscous region. It appears as a function of the wall-normal distance, density, dynamic viscosity, wall shear stress, the wall-tangential pressure gradient, and convective term. Finally, the functional dependence of the time-averaged velocity ($\overline{u}(y)$) is given by

$$\begin{aligned}\overline{u}(y) &= f(y,\rho,\mu,\tau_w,\frac{\partial p}{\partial x},(\frac{\partial(\rho\overline{uu})}{\partial x} + \frac{\partial(\rho\overline{uv})}{\partial y})) \\ &= \frac{\tau_w}{\mu}y + \frac{1}{4\mu}(\frac{\partial(\rho\overline{uu})}{\partial x} + \frac{\partial(\rho\overline{uv})}{\partial y})y^2 + \frac{1}{2\mu}\frac{\partial \overline{p}}{\partial x}y^2\end{aligned} \tag{5.10}$$

Equation 5.10 is a near-wall velocity profile within the viscous region. It appears as a second-order polynomial equation. It no longer follows the law of wall [138], considering

that the pressure gradient and convective terms play an important role. According to Equation (5.10), the non-equilibrium wall effects can be categorized into three different terms: wall shear stress, convective term, and wall-tangential pressure gradient. The corresponding scaling parameters for the three terms above will be exhibited respectively to investigate their contributions to the non-equilibrium near-wall effects.

$$u_\tau = |\frac{\tau_w}{\rho}|^{1/2} \tag{5.11}$$

$$u_p = |\frac{\mu}{\rho}\frac{\partial \overline{p}}{\partial x}|^{1/3} \tag{5.12}$$

$$u_{conv} = |\frac{1}{2}\frac{\mu}{\rho}\frac{\partial(\rho\overline{uu})}{\partial x} + \frac{\partial(\rho\overline{vu})}{\partial y}|^{1/3} \tag{5.13}$$

$$u_c = u_\tau + u_p + u_{conv} \tag{5.14}$$

The scaling parameter (u_τ) is a standard reference velocity utilized widely for the inner layer scaling as friction velocity based on wall shear stress. The scaling parameter (u_p) is based on wall-tangential pressure gradient, which has been appearing in several studies [139–141]. For the convective term (u_{conv}), it is to follow a study by Li et al. [136]. By combining all these terms, an overall near-wall effect can be accounted for, as described in Equations (5.11) to (5.14).

The investigation commences within the viscous region of the flow impingement on the liner wall. In Figure 5.20, the flow field and wall patch reveal a pronounced distribution of strong pressure gradient. The investigated plane is situated at an angle of 54° counterclockwise to the symmetry plane. This particular plane is chosen due to the flow impingement induced by the intake jet, denoted as (C2) in Figure 5.7. In contrast to the intake jet (C1) in Figure 5.7, the intake jet (C2), constrained by the intake valve layout, does not form a tumble motion. Instead, it causes an impinging flow upon the liner wall. By examining the wall-tangential pressure gradient from the first computational cell along the wall, spanning from y = 0 to y = -35 mm, two distinctive belt-shaped distributions emerge, separated by a region with a relatively low-pressure gradient, indicating the impinging center. During flow impingement, the impinging center experiences the most significant wall-normal stress induced by the impinging flow. Subsequently, the flow, once it collides with the wall, initiates wall shear and forms a near-wall jet flow. It then induces the production and escalation of the wall-tangential pressure gradient [142]. This phenomenon will be further explored in the subsequent section through the application of the introduced near-wall scaling parameters.

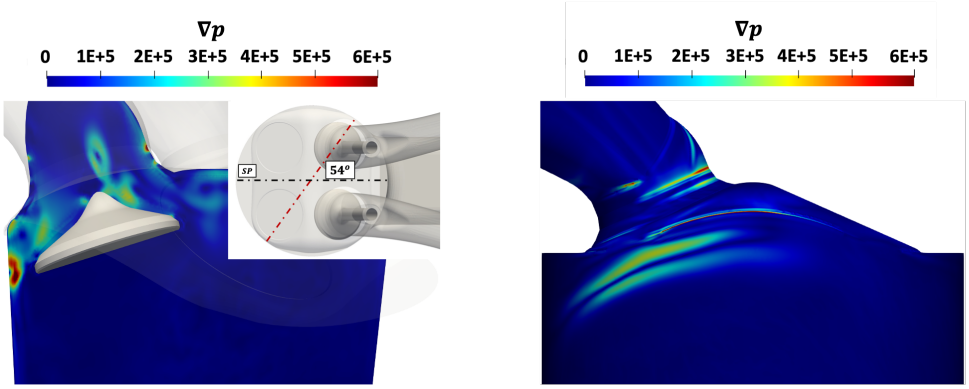

(a) In-cylinder pressure gradient. Note: the presented plane is situated at an angle of 54^o counterclockwise from the symmetry plane

(b) Wall-tangential pressure gradient at the liner wall. Note: side view of the engine flow bench

Figure 5.20: Pressure gradient distribution in the intake flow impinging region. Both in-cylinder field and wall are presented

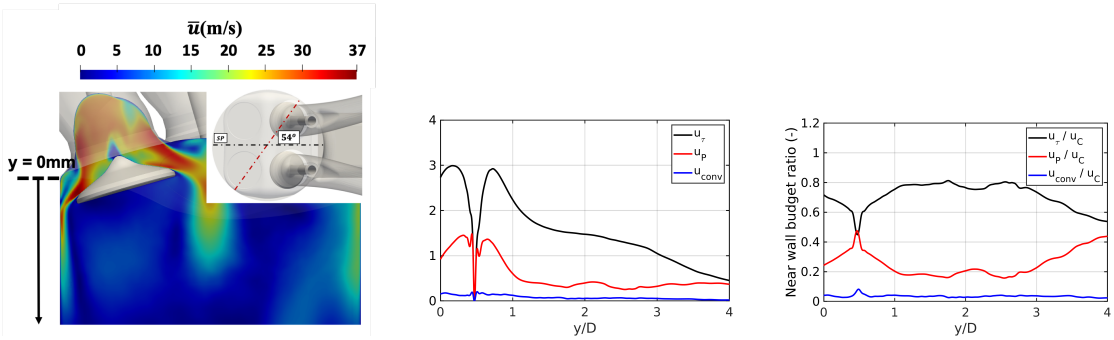

(a) Impingement liner wall sampling

(b) Near-wall effects profile along the impingement liner wall

(c) Near-wall budget analysis along the impingement liner wall

Figure 5.21: Near-wall effects analysis at impingement liner wall situated at an angle of 54^o counterclockwise from the symmetry plane. Note: D represents the valve lift of 9.21 mm

To delve deeper, the initial cell data along the wall, positioned at the same afore-

mentioned distance, is extracted. The measured location follows the engine flow bench coordinate on the y-axis and is normalized by the valve lift (D = 9.21 mm), as shown in Figure 5.21. Figure 5.21 (b) and (c) highlight the distribution of near-wall effects and the proportional contribution of these effects.

At the stagnation point of the impingement center, all near-wall contributions are zero, as depicted in Figure 5.21 (b). It aligns well with the characteristics of the impinging center, in which the only contribution is in the wall-normal direction, as illustrated previously. Moving away from the impingement center, both the wall shear stress and wall-tangential pressure gradient exhibit significant production. This production displays a semi-axisymmetric behavior that aligns with the fundamental characteristics of wall-impinging flows [142]. Additionally, the convective effects within the viscous region have a relatively minor impact compared to the wall-tangential pressure gradient. This observation reflects the common practice of neglecting the convective term in wall functions [139, 141, 143]. An intriguing aspect emerges where wall shear stress continues dominating the near-wall effects, contributing approximately 75% to 80% of the overall near-wall effects. Moreover, this contribution notably decreases at the impinging center. This near-wall analysis can be plausible only if the same near-wall effects can be observed in fundamental impinging flow.

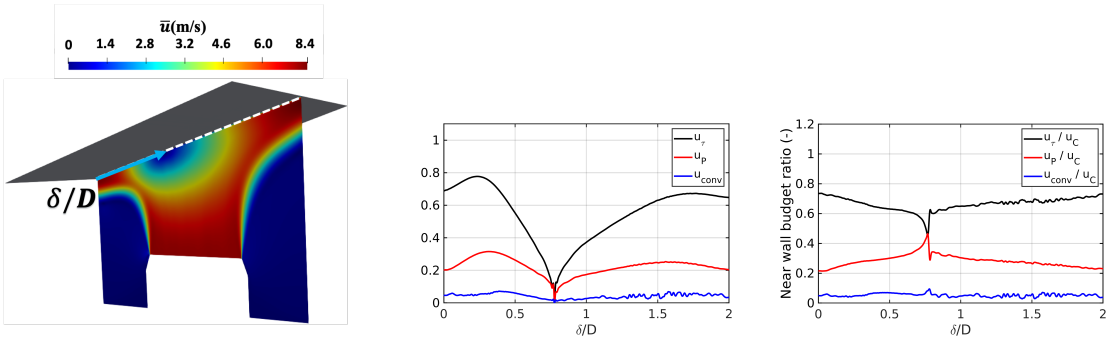

(a) Impingement liner wall sampling

(b) Near-wall effects profile along the impingement liner wall

(c) Near-wall budget analysis along the impingement liner wall

Figure 5.22: Near-wall effects analysis at an inclined impinging wall of its inclined angle of 75^o [144] served as a reference for liner wall impingement, as shown in Figure 5.21

To establish a meaningful comparison with the canonical flow, Figure 5.22 presents a near-wall effect analysis of an inclined impinging flow at an angle of 75° [144]. The

reference is chosen as the inclined angle is close to the valve angle of the target engine flow bench. Remarkably, the results between the liner wall impingement and the inclined impinging flow exhibit strong comparability. This alignment is evident in various aspects, including the overall shape of the effects and their contribution levels by comparing Figure 5.21 (c) and Figure 5.21 (c).

In addition to the impingement of the intake jet on the liner wall, the region around the intake valve plays a crucial role during the intake phase. As the intake flow navigates through the intake ports and impinges upon the intake valve, it generates large-scale motions and their corresponding turbulence. This leads to a notable pressure gradient at the intake valves, particularly pronounced close to the valve tip. Figure 5.23 illustrates and investigates the phenomenon: the intake flow interacts with the intake valve, creating a strong pressure gradient, particularly in proximity to the valve tip.

Due to the geometric discontinuity between the intake valve, a separating flow occurs at the valve tip, marked as a white broken line in Figure 5.23 (a). This separation causes a significant reduction in wall shear stress (u_τ), as depicted in Figure 5.23 (b), specifically in the red patch where $\delta/D > 1.1$. Given the substantial flow passing by the intake valves, the impact of the convective term within the viscous region remains minimal, contributing at most around 5 percent of the overall effect.

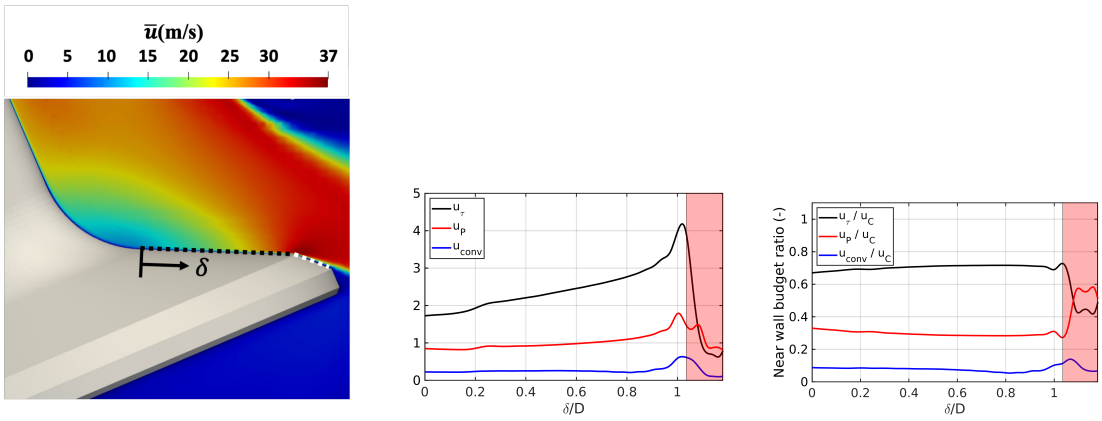

(a) Intake valve sampling

(b) Near-wall effects profile along the intake valve

(c) Near-wall budget analysis along the intake valve

Figure 5.23: Near-wall effects analysis at the intake valve. Note: the red patch indicates the region beyond the intake valve tip, marked as a white broken line in Figure 5.23 (a). D represents the valve lift of 9.21 mm

The analysis of near-wall effects provides strong evidence that the engine flow operates in a non-equilibrium manner. Specifically, during the intake phase, the engine flow exhibits a significant wall-tangential pressure gradient, which accounts for an average of 20 to 30 percent of the overall near-wall contribution. This observation highlights that the conventional wall function approach based on canonical channel flow might not be appropriate for such complex and non-equilibrium engine flow scenarios.

Furthermore, several wall functions [136, 137] considering non-equilibrium effects, such as near-wall pressure gradient, and contribution of convection, follow the assumptions in the near-wall region:

- The term, pressure gradient ($\frac{\partial \overline{p}}{\partial x}$), is independent of the wall-normal distance (y) and can be taken as constant.
- The convection terms are zero at the wall and behave linearly with the wall-normal distance (y).

To justify whether these assumptions are valid in engine applications, by extracting the near-wall region from the valve wall up to $y^+ = 100$, Figure 5.24 demonstrates a profile of the terms of pressure gradient and convection. The results reveal that the assumptions are valid yet conditionally. Within the near-wall region ($y^+ < 100$), the term, pressure gradient ($\frac{\partial \overline{p}}{\partial x}$), remains constant; however, the convection term behaves linearly only in the region ($y^+ < 20$). It suggests that applying a non-equilibrium wall function in engine application, especially during the intake phase, the first grid must be placed within the region ($y^+ < 20$) to get a more accurate result.

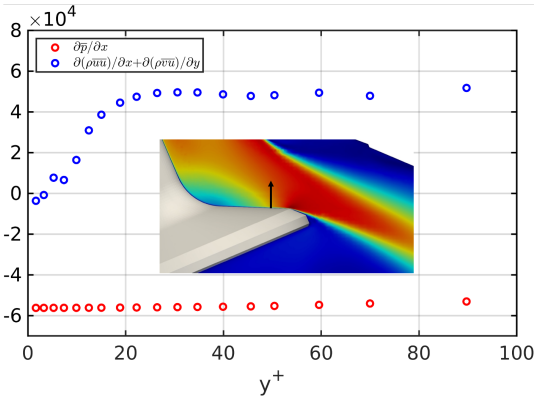

Figure 5.24: Profile of the pressure gradient and convective term along the wall-normal direction at $\delta/D = 0.5$, as shown in Figure 5.23

5.5.1 Turbulent budget analysis

As yet, attention has primarily been dedicated to understanding the non-equilibrium effects along the engine walls, particularly within the viscous layer where $y^+ < 5$. Within this region, turbulence is dominated by the effects of molecular viscosity. The behavior of near-wall turbulence in the intake valve region remains elusive. Consequently, employing the equation that governs the transport of turbulent kinetic energy (TKE) can provide valuable insights into the turbulence dynamics within the intake valve region. The governing equation of turbulent kinetic energy (TKE) transportation is illustrated as follows:

$$\frac{\partial k}{\partial t} + \widetilde{u}_i \frac{\partial k}{\partial x_i} = \underbrace{-\langle \widetilde{u_i'} \widetilde{u_j'} \rangle \frac{\partial \widetilde{u}_i}{\partial x_i}}_{P_k} \underbrace{- 2\nu (\widehat{S'}_{ij} \widehat{S'}_{ij})}_{\epsilon_k} \underbrace{- 2 \frac{\partial}{\partial x_j} \langle \widetilde{u_j'} \widehat{p'} \rangle}_{\Pi_{tke}} + \underbrace{2\nu \frac{\partial}{\partial x_j} (\widetilde{u_i'} \widehat{S'}_{ij})}_{D_{tke}} \underbrace{- \frac{\partial}{\partial x_j} \langle \frac{1}{2} \widetilde{u_i'} \widetilde{u_i'} \widetilde{u_j'} \rangle}_{T_{tke}} \quad (5.15)$$

where $\widehat{(.)}$ and $\widetilde{(.)}$ denote the filter operator and the Favre operator, respectively. The rate of deformation tensor $\widehat{S'}_{ij} = \frac{1}{2}(\frac{\partial \widetilde{u_i'}}{\partial x_j} + \frac{\partial \widetilde{u_j'}}{\partial x_i})$.

Equation 5.15 comprises five essential terms for the near-wall turbulence budget, which are turbulence production (P_{TKE}), turbulence dissipation (ϵ_{TKE}), pressure diffusion (Π_{TKE}), viscous diffusion (D_{TKE}) and turbulence diffusion (T_{TKE}).

To investigate the near-wall turbulence, the analysis is conducted at a chosen location of $\delta/D = 0.5$, as shown in Figure 5.23. This location consists of the near-wall effect from the wall-tangential pressure gradient of approximately 30 percent of the total contributions, as depicted in Figure 5.23 (c). The data is extracted in the direction normal to the intake valve wall, extending up to 3 mm with a corresponding $y^+ = 350$. The profiles of each term are shown in figure 5.25.

The behavior depicted in Figure 5.25 for the near-wall turbulence budget stands in stark contrast to that of canonical channel flow [77]. In canonical channel flow, turbulence production is balanced by turbulence diffusion (T_{TKE}) and viscous diffusion (D_{TKE}). However, in the case of the intake flow jet, turbulence production finds balance through pressure diffusion (Π_{TKE}) and viscous diffusion (D_{TKE}). A similar pattern is also observed in an inclined impinging flow [145]. It is noteworthy that a distinct spike in turbulence production (P_{TKE}) emerges after $y^+ > 100$, possibly attributed to the influence of the free-stream flow. This can reflect the previous analysis that anisotropic intensity increases with increasing the invariant ξ after $y^+ > 100$, deviating from the near-wall flow phenomenon, as shown in Figure 5.19 (b).

As a result, the near-wall inner layer is exceedingly thin in comparison to the funda-

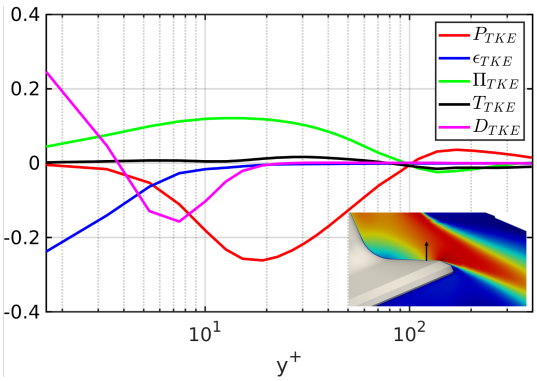

Figure 5.25: Profile of the turbulence budget terms along the wall-normal direction at $\delta/D = 0.5$, as shown in Figure 5.23

mental canonical channel flow. These findings collectively indicate that the presence of wall-tangential pressure gradient significantly influences the near-wall flow in ICEs, particularly in the intake valve region during the intake phase.

5.6 Conclusion

This chapter has provided a comprehensive investigation of the near-wall and free-stream in-cylinder flow within an engine flow bench, with a focus on simulating the intake flow of a real engine application. Key findings and observations from this study can be summarized as follows:

- LES is employed in this study and effectively reproduced the large-scale motion and turbulence structure. It demonstrated good agreement with reference experimental PIV data.
- Turbulence anisotropy analysis revealed that the in-cylinder turbulence structure of the engine flow is characterized by a strong orientation towards axisymmetric expansion and contraction. This orientation results from the specific topological pattern of the engine flow, notably the tumble vortex and the intake overflow jet. The intensity of turbulence anisotropy (F) in the in-cylinder flow typically exhibited values higher than 0.6, primarily initiated by the anisotropy weakening of the intake flow. Additionally, the turbulent flow field in the valve plane displayed a higher level of anisotropy than the in-cylinder flow in the central tumble plane.

- The turbulence characteristics of the intake jet resemble those of a canonical free shear jet, primarily due to the significant influence of near-wall turbulence associated with the intake port, especially the intake valves.
- The near-wall non-equilibrium effects within the engine flow bench were investigated through near-wall budget analysis. The flow region studied included the viscous layer on the jet impact area on the liner wall and the intake valves. Results showed that the high Reynolds number (Re = 32,400) of the inlet flow resulted in a substantial pressure gradient, leading to non-equilibrium effects that varied across different regions. Notably, a significant contribution from the pressure gradient in the flow direction was observed in both regions, comparable to the basic oblique impinging flow. These findings suggest that the classical wall function modeling approach based on the classical zero-pressure-gradient boundary layer may no longer be valid for ICEs applications.

6 Spray-wall-flow interaction in a GDI engine flow bench[1]

Effort throughout the thesis, so far, has been devoted to the investigation and discussion of the spray morphologies and spray-wall interaction in a constant-volume chamber where the boundary conditions are well controlled. Even though it can simulate engine conditions, the engine flow, including the large-scale motion and turbulence structure extensively discussed in Chapter 5, is neglected. An engine flow bench is suitable for investigating spray-wall-flow interaction closer to the condition in real engines. An engine flow bench reduces the complexity in the number of variables inherent in engine flow and whole-engine simulation and facilitates a detailed investigation during the intake phase. Therefore, an engine flow bench operating under various mass flow rates is applied in this chapter to understand spray-wall-flow interaction exclusively under early-injection conditions.

This chapter will transition from the experimental measurement of spray plume visualization and numerical setup to the investigation of spray-wall-flow interaction. The investigation will detail the validation in spray formation, comparing the penetration length and qualitative Mie scattering images. Thereupon, spray plumes from each injector hole will be investigated under varying mass flow rates. Both the evaporation effect and spray-wall-flow interaction are to be discussed. Finally, the spray's impact on the in-cylinder turbulence kinetic energy will be examined.

Apart from the configuration of the engine flow bench, which has been discussed in detail in Chapter 5, the engine flow bench operates with various mass flow rates (100%, 75%, and 50%) to provide a variation of the *Re*. The definition of *Re* is illustrated in Chapter 5 and can be also found in a work by Welch et al. [24] The 100% mass flow rate was set by adjusting the mass flow rate to match the intake velocity of a motored engine at -270° CA. The engine speed and intake pressure of the motored engine described here are 800 rpm and 0.95 bar, respectively [24]. In this study, 50% and 100% mass flow rates are chosen to investigate the spray-flow interaction, and the corresponding Reynolds

[1]This section is partly taken from a publication by Lien et al. [3], which was accomplished during the work on this thesis. In Ref. [3], I was the first author.

numbers (*Re*) are 32,400 and 16,200, respectively. Table 6.1 summarizes the relevant boundary conditions of the engine flow bench.

Table 6.1: Experimental parameters of the operating conditions

Condition	100%	50%	0%
Inlet temperature ($T_{\text{in},2}$)(°C)	22.7	23.2	21.9
Inlet pressure ($P_{\text{in},2}$)(bar)	1.0	1.0	1.0
Outlet pressure ($P_{\text{out},2}$)(bar)	0.998	1.007	1.0
Mass flow rate ($\dot{m}_{\text{in}}$)(kg/h)	94.10	47.09	0.517
Reynolds number	32,400	16,200	178

In addition to the operating conditions, a multi-hole counter-bore injector is mounted on the cylinder head (spray-guided) at an angle (8 °) to investigate the interaction between the intake flow and spray. The applied multi-hole counter-bore injector (Spray G) is from ECN, and the injection pressure is set to 200 bar with a total injected mass of 10 mg. In this chapter, pure iso-octane is employed as injected fuel. The injection settings for the experiments under the three targeted conditions are shown in Table 6.2.

Table 6.2: Essential parameters of the injector operating conditions

Spray G (iso-octane)	
Fuel	iso-octane
Fuel temperature (K)	363
Injection pressure (bar)	200
Electronic injection duration (ms)	0.66
Total injection duration (ms)	0.78
Total injected mass (mg)	10

As the spray contains a two-phase flow, liquid and vapor, PIV measurement was utilized to measure the gas phase of the bulk flow, while volumetric Mie scattering was used for liquid spray visualization. Following the setup from PIV measurement, the spray formation images are acquired by obtaining Mie scattering of light from a pulsed LED in volume illumination from the bottom through the optical window, as shown in figure 5.1. An effective sampling rate of 25 kHz was achieved. Figure 6.1 shows the schematic of the Mie scattering measurement and a captured spray plume. To provide a more accurate statistic of spray formation under different mass flow rates of the engine flow bench, the experiment sampled 100 injection cycles at each mass flow rate. The Mie scattering measurement and post-processing procedure details can be found in a study from Geschcwindner et al. [42].

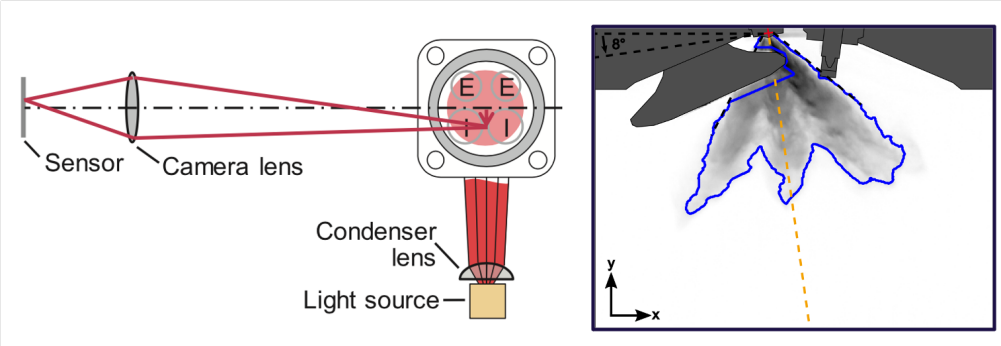

Figure 6.1: Top view of the optical measurement using Mie scattering image and side view of the spray plume image [42]. Reprinted with permission.

Following the meshing strategy introduced in Chapter 5 to provide a scale-resolved LES and alleviate the uncertainties derived from wall functions. In this chapter, the same near-wall treatment, 15 near-wall cell layers with a growing ratio of 1.05 are placed to resolve the near-wall boundary layer sufficiently, and the cell size nearest to the wall is 12 µm (y^+_{avg} = 0.6), is also applied, as shown in Figure. The superscript + refers to quantities that are non-dimensionalized via the viscous length scale $\sigma_v = \nu/u_\tau$, where ν and u_τ are the molecular viscosity and friction velocity, respectively. The primary cell size is set to 350 µm. Moreover, the mesh is also designed to capture the spray evolution within the engine flow bench. Figure 6.2 (b) displays a two-cone shape refinement at the central tumble plane. Both feature a hexahedron-type mesh up to 40 mm, which covers the whole spray evolution during the injection. The size of the finest-cone mesh is 0.125 mm. A summary of the relevant mesh parameters is given in Table 6.3.

Table 6.3: Essential mesh setup for LES simulation

LES	
Cell number	20 millions
y^+	avg. 0.6
x^+ *and* z^+	avg. 1.0
Boundary layers	15
First layer mesh refinement	0.25 mm
Second layer mesh refinement	0.125 mm

Furthermore, as the spray-wall interaction is one of the objectives in this chapter, a single-layer strategy is applied for calculating wall film development. Figure 6.3 demon-

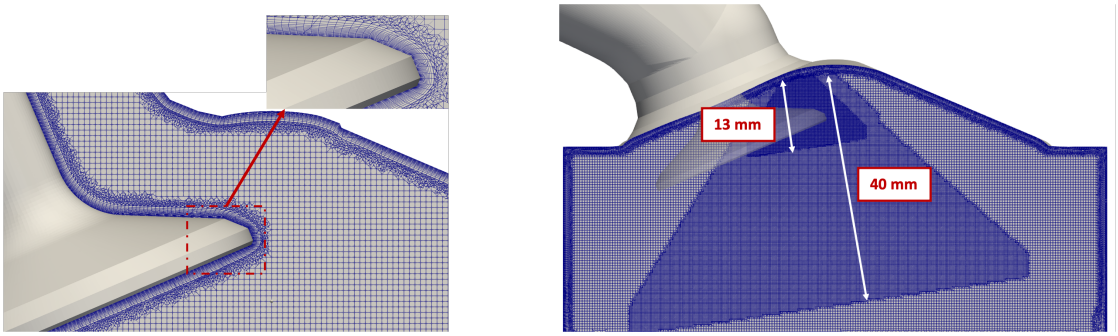

(a) Near-wall meshing strategy

(b) Spray refinement region at central tumble plane

Figure 6.2: Mesh configuration and meshing strategy of LES

strates the wall film strategy and the applied mesh. Since the in-cylinder flow is simulated using LES, the turbulence is captured statistically and may influence the spray formation. The multi-cycle spray injection simulation is thus required to mitigate the cycle-to-cycle variation. The averaged data is sampled through 25 cycles of injections at each mass flow rate.

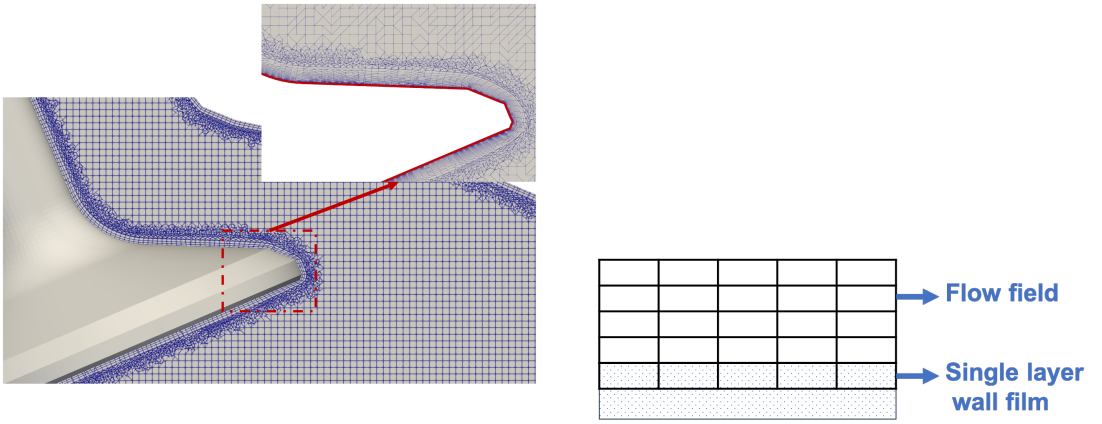

(a) Wall film mesh strategy

(b) Schematic of single-layer mesh

Figure 6.3: Mesh configuration and meshing strategy of wall film formation. Note: Red color denotes the single-layer mesh for wall film calculation

Often, the numerical liquid spray penetration is calculated based on the mass fraction of the liquid droplets. Nevertheless, this assumption is hardly applied to the post-processed experimental data based on the obtained Mie scattering signal. Following the same procedure as the experiments to acquire a comparable numerical Mie scattering signal, every injection cycle is assigned an individual threshold s [42]. The individual threshold (s) is 5% of the maximum spray intensity at each injection cycle. Unlike the experimental Mie scattering, the numerical Mie scattering signal($S_{\mathbf{Mie}}$) is calculated based on each Lagrangian particle [55]. The equation is written as:

$$S_{\mathbf{Mie}} = n_p \frac{\pi}{4} d_p^2, \tag{6.1}$$

where n_p is the number of liquid droplets inside each Lagrangian particle.

Equation 6.1 follows the assumption that the intensity of the Mie scattering signal is proportional to the projected liquid droplets and that all the liquid droplets are spherical. Thereafter, the obtained binarized numerical Mie signal is projected onto the X-Y plane, and the signal boundary is calculated based on the individual threshold (s). Figure 6.4 shows the numerical Mie scattering data procedure corresponding to the experimental one in Figure 6.1.

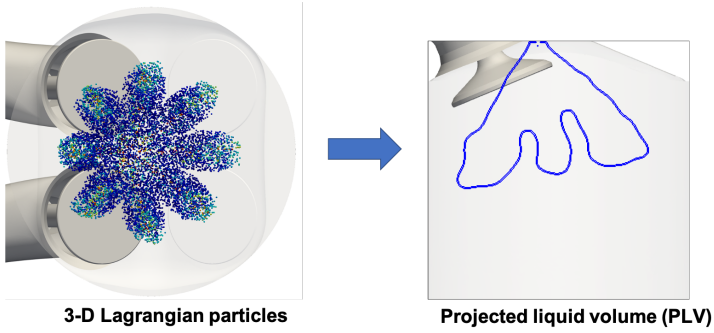

Figure 6.4: Schematic pathway to post-process the simulation data, projected liquid volume using Mie scattering signal for comparison

The spray penetration length and spray angle are calculated based on the binarized Mie scattering signal to provide a more consistent comparison with experimental data [55]. The penetration length is calculated based on 99% of the binarized Mie scattering signal, while the spray angle is calculated by means of the plume width and penetration based on the maximum and minimum signal thresholds, 99% and 5%, respectively. Both definitions are shown in Figure 6.5.

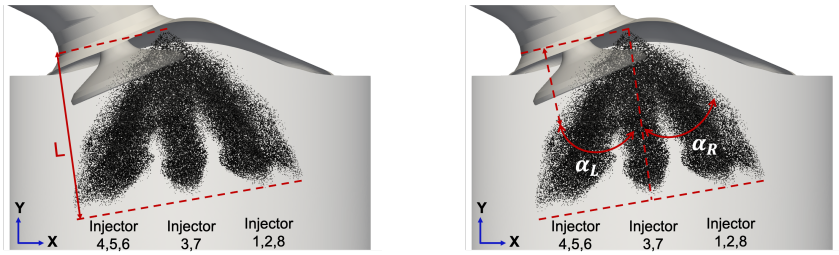

(a) Spray penetration length (b) Spray angle

Figure 6.5: Schematic definition of spray penetration length and spray angle

Before delving into the results and discussions directly, it is imperative to assess if the present mesh is sufficient enough for resolving turbulence using LES. Previously, the mesh assessment has been conducted using the LES index based on Pope [77] and proposed by Celik et al. [83] in Chapters 3 and 4. The same technique will be also employed in the present study. Figure 6.6 shows the viscosity ratio and its corresponding examining index in the tumble plane at aSOI $= 0.64$ ms. Due to the resolution of the in-cylinder flow, the primary mesh size is set up as 350 µm. The majority of the viscosity ratio lies below 15, resulting in its corresponding index value of 85%. It is worth noting as the index only weighs the sub-grid viscosity and the molecular viscosity, this index cannot solely represent the near-wall resolution. The sub-grid viscosity (ν_t) is dampened to zero due to the wall boundary conditions. To resolve the near-wall region by capturing the turbulence kinetic energy production, it is inevitable to apply a meshing strategy, as shown previously in Table 6.3.

6.1 Spray formation: validation and investigation

In Chapter 5, the in-cylinder flow within the target engine flow bench has been exclusively discussed and validated in not only the central tumble but also the valve planes. Building upon this, the section includes the spray into each mass flow rate (MFR) and compares it with the experimental Mie scattering images. The inclusion of a no-flow case serves as a benchmark to compare and gain a better understanding of the spray-flow interaction under different mass flow rates (MFRs).

Figure 6.7 first provides a comparison of the spray penetration length and spray angle ($\alpha = \alpha_\mathrm{L} + \alpha_\mathrm{R}$). It is observed that neither the spray penetration length nor the spray angle varies significantly with different mass flow rates. This suggests that spray-flow

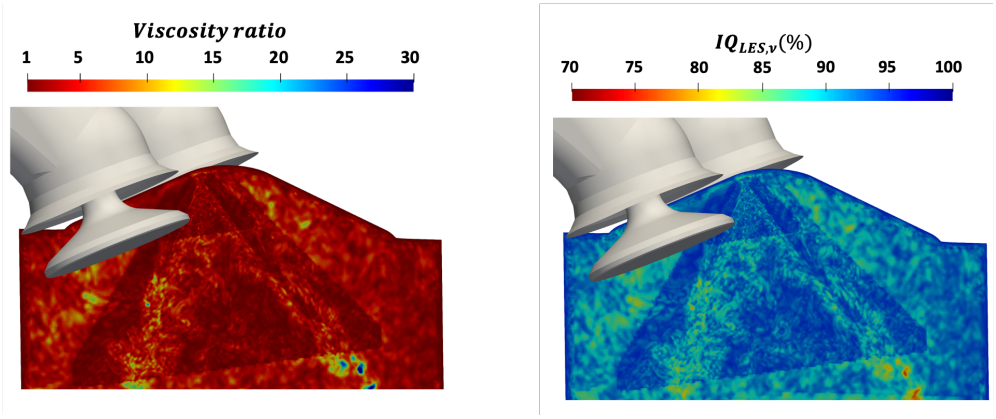

(a) Viscosity ratio ($\frac{\nu_{t,eff}}{\nu}$) (b) LES quality index ($IQ_{LES,\nu}$)

Figure 6.6: Examining mesh quality at a time after the start of injection (aSOI) = 0.64 ms

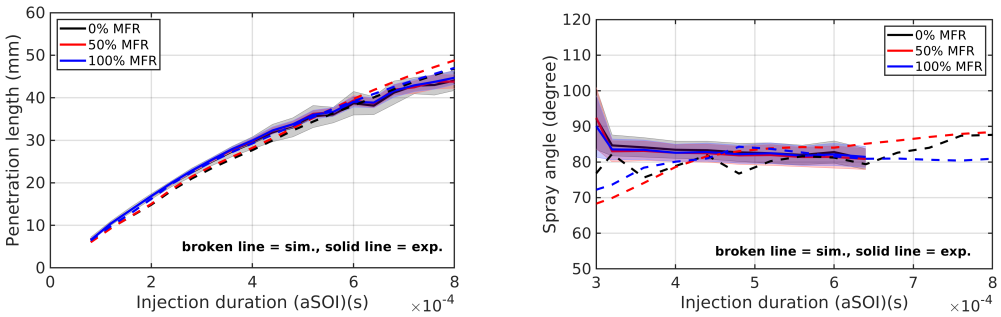

(a) Penetration length (b) Spray angle

Figure 6.7: Quantitative comparison of spray penetration length and spray angle

interaction might have a minor influence in all cases, although these are merely global quantities. It should be noted that the experimental measurement of the spray angle is limited from 0.3 ms until 0.64 ms aSOI due to the obstruction caused by the valves and disturbance in the in-cylinder flow. Nonetheless, the simulation data align well with the experimental results.

Figure 6.8 further presents a qualitative comparison of the spray plume evolution using the mean binarized Mie scattering images. It is observed that as the mass flow rate (MFR) increases, the line-of-sight protection of the spray plumes becomes distorted by the in-cylinder flow. Unlike the quantitative comparison, in which the spray-flow interaction

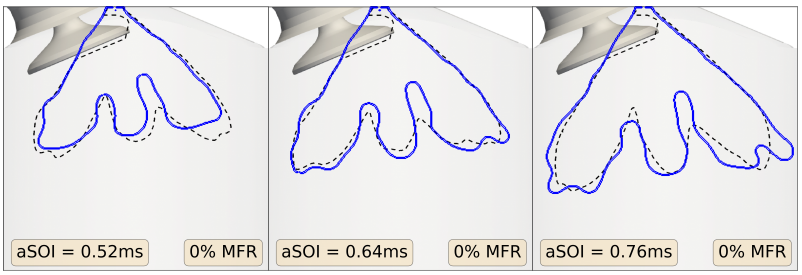

(a) No-flow case

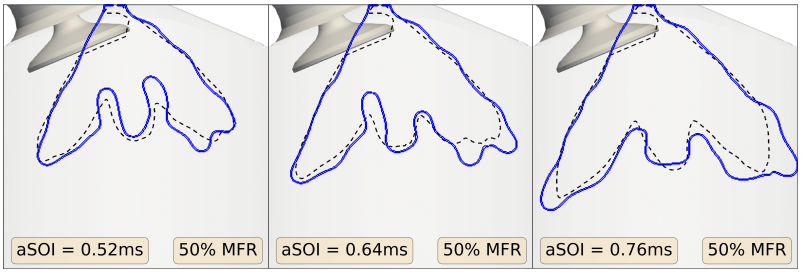

(b) 50% mass flow rate

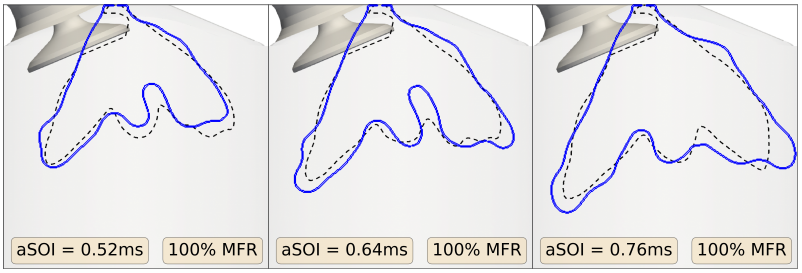

(c) 100% mass flow rate

Figure 6.8: Qualitative comparison of the projected liquid boundary using Mie scattering images. Black broken line: the experimental data, Blue solid line: the simulation data

is not as prominent, the influence of the spray-flow interaction starts to manifest itself at aSOI = 0.64 ms. Increasing the mass flow rate leads to the distortion of the left-wing spray plumes, resulting in a narrower and sharper shape that extends further downstream. Furthermore, the plume structures from left to right start to collide with each other in the case of a 100% mass flow rate. It is worth noting that the binarized Mie scattering images are calculated for each cycle and averaged. The plume-to-plume variation thus

cannot be observed if it is below the setup threshold (s).

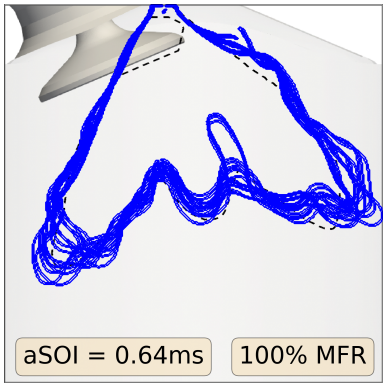

(a) Single injection at 100% MFR

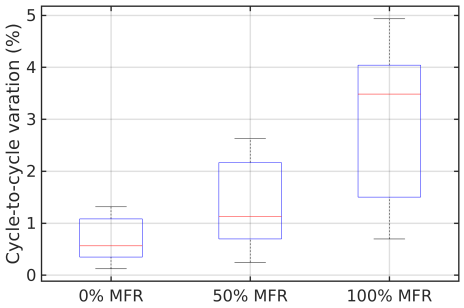

(b) Cycle-to-cycle variation.

Figure 6.9: Cycle-to-cycle variations of spray formation. Note: figure (b) presents the deviation of the liquid penetration length over 25 injections.

Apart from the validations with experimental data, it was mentioned previously, the demonstrated spray plume is averaged over 25 injections at each MFR. The cycle-to-cycle variations may occur and become more intense by increasing MFR. To understand this phenomenon, Figure 6.9 (a) shows the plume shape of each injection at aSOI = 0.64 ms in the case of 100% MFR. The cycle-to-cycle variation can be observed, especially in the left- and right-wing plumes. It is evident that the intake flow has an impact on the spray formation despite a high spray injection pressure of 200 bar.

To quantify the cycle-to-cycle variation under different MFR, Figure 6.9 (b) examines the liquid penetration length with 25 injections. The cycle-to-cycle variation becomes more notable by increasing MFR. In the case of 0% ambient flow, the variation is less than 1%, whereas the variation increases up to a maximum of 5% for the case of 100% MFR. It indicates the necessity of multi-cycle simulation for LES for real GDI applications.

So far, the validation of the simulation data has been achieved by comparing it with experimental data qualitatively and quantitatively. The observation of spray-flow interaction becomes more apparent as the mass flow rate increases. The following section will focus extensively on the effects of spray-flow interaction.

6.2 Spray-wall-flow interaction

The aforementioned disturbance effect on spray formation at different mass flow rates can be attributed to convection, evaporation, and spray-wall interaction. Spray-wall interaction likely occurs on the piston, valves, cylinder liner wall, and even spark plug when it comes to a real GDI engine. However, in a GDI engine flow bench with its piston removed and the fixed valve lift used in this study, spray-wall interaction is expected to occur primarily on the valves and cylinder liner wall. All the effects will be discussed and examined individually in this section.

Although the presence of spray-flow interaction was evidently observed in Figure 6.8, it has not yet been possible to quantify how a 100% mass flow rate differs from a no-flow one. Given the symmetrical arrangement of the injector holes in Spray G, it can be assumed that the boundary of the plume behaves symmetrically from left to right. To quantify this symmetry, an axisymmetric index (F_α) can be defined by means of the spray angle (α_L and α_R), which is shown in Figure 6.5. This index F_α is written as:

$$F_\alpha = \frac{\alpha_R}{\alpha_L}, \tag{6.2}$$

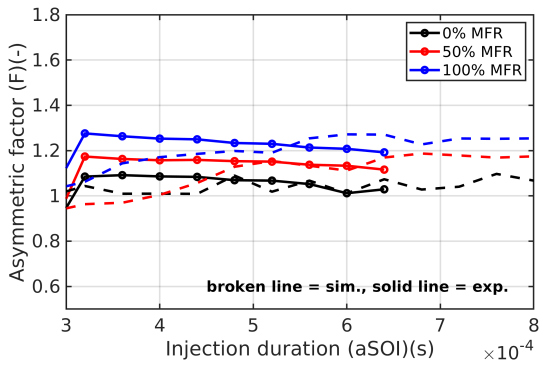

Figure 6.10: Quantitative comparison of the axisymmetric factor (F_α), defined in equation 6.2

Equation 6.2 weighs the left and right spray angles. If the spray plume is distorted and shifts towards the right-hand side, the axisymmetric factor will be greater than one. Conversely, if the plume moves towards the left, the factor will be less than one. Figure 6.10 illustrates how the axisymmetric factor evolves with time, up to 0.8 ms. In the no-flow case, the factor remains close to unity throughout the entire evolution, indicating approximate axisymmetry. In contrast, this index F_α grows when the mass flow rate

increases. Interestingly, index F_α remains stable in all cases, at 1.2 and 1.3 for 50% and 100% mass flow rates, respectively. It is important to note that Figure 6.10 does not provide information about the orientation of the distorted plume, and the projected central plume is not taken into account.

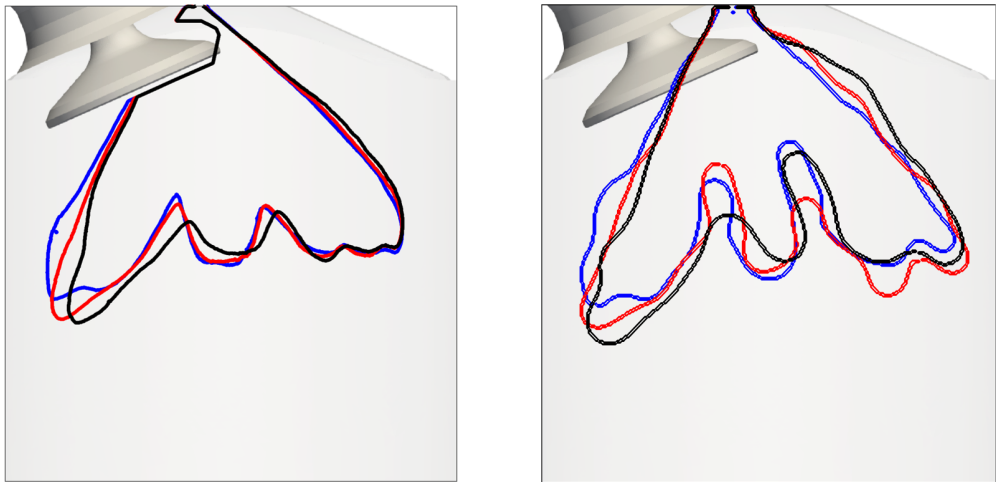

(a) Experimental PLV (b) Numerical PLV

Figure 6.11: Quantitative comparison of PLV with different mass flow rates at aSOI = 0.64 ms. Blue line: 0% MFR, red line: 50% MFR, and black line: 100% MFR.

Figure 6.11 further presents the PLV images at aSOI = 0.64 ms. It reveals that the examination can be biased by merely using the axisymmetric index (F_α). As the mass flow rate increases, the left-wing plume undergoes the most significant distortion, resulting in a reduction in the left spray angle (α_L). By contrast, the right-wing plume remains intact with mass flow rates, except for the minor distortion on the upstream right-wing plume. The behavior of the central plume closely resembles that of the right-wing plume; it shifts towards the right as the mass flow rate increases. Despite the presence of the spray-flow interaction, it does not affect the plume penetration. The greatest penetration is located at the left- and right-hand side plumes. This explains the consistency of the plume penetration with different MFRs, as shown in Figure 6.7.

All the evidence indicates that the intake flow, especially the intake jet, plays a crucial role in the local spray-flow interaction. Based on the current observation, the spray plumes from each injector hole do not behave symmetrically with varying MFRs. Questions arise from this observation as to whether the spray plume from each injector hole behaves homogeneously and whether the evaporation due to convection also contributes to the

phenomenon. To address these questions, Figure 6.12 (a) provides the index of each injector hole, offering more constructive information for further analysis. Figure 6.12 (b) demonstrates the evaporation effect of each injector hole, represented by the evaporation ratio calculated as the normalized vapor mass compared to the no-flow case, facilitating direct comparisons.

Compared to the no-flow case, the vapor mass increases by at most 9.5% and 4.3% in the case of 100% and 50% mass flow rates, respectively. Interestingly, most of the evaporation occurs primarily close to the right-hand side, where the intake jet resides, except Plume 1, which is far from the intake jet. On the other hand, the vapor mass of Plumes 4 and 6 on the left-hand side increases slightly by approximately 1% to 2%, compared to the no-flow case. Notably, Plume 5, which is expected to have minimum evaporation due to its location, exhibits the highest evaporation contribution. The heterogeneous behavior among the plumes cannot be attributed to convective evaporation alone. This merits a more in-depth investigation of each plume's penetration length.

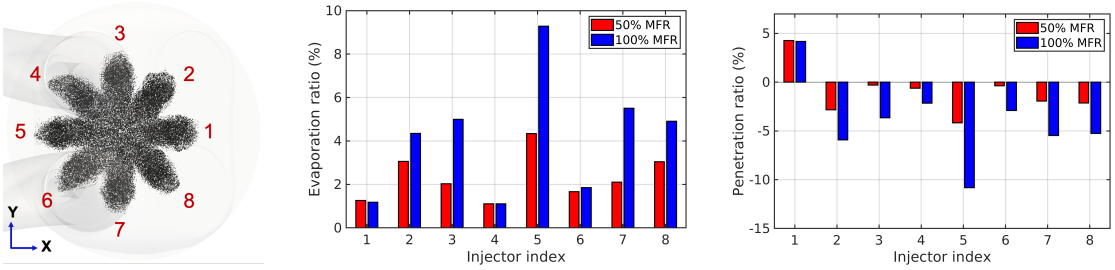

(a) Index of each injector hole

(b) Evaporation ratio

(c) Penetration ratio

Figure 6.12: Examination of how the evaporation and penetration ratios affect each spray plume

Figure 6.12 (c) compares the penetration length of each plume. The penetration ratio, similarly to the evaporation ratio, is normalized by the no-flow case. Due to the disturbance of the intake flow, almost all plumes exhibit reduced penetration compared to the no-flow case. Plumes 4 and 6 experience decreased penetration, albeit with minor influence from the intake jet. Notably, Plume 1 demonstrates increased penetration as the mass flow rate increases, while Plume 5 encounters the most significant disturbance. Plumes 3 and 7, dwelling in the center, have penetration that is a mere 4% and 2% less in the case of 100% and 50% mass flow rates, respectively. Although Plume 5 undergoes a strong reduction in the penetration length in the case of 100% MFR, the rest of the plumes exhibit no more than a 5% difference compared with the no-flow case. This

finding aligns with the results in Figure 6.7, where the penetration length appears to be relatively independent of the mass flow rate. However, attention should be devoted to Plumes 1 and 5, as both reside in the central tumble plane and display the most disparate behaviors.

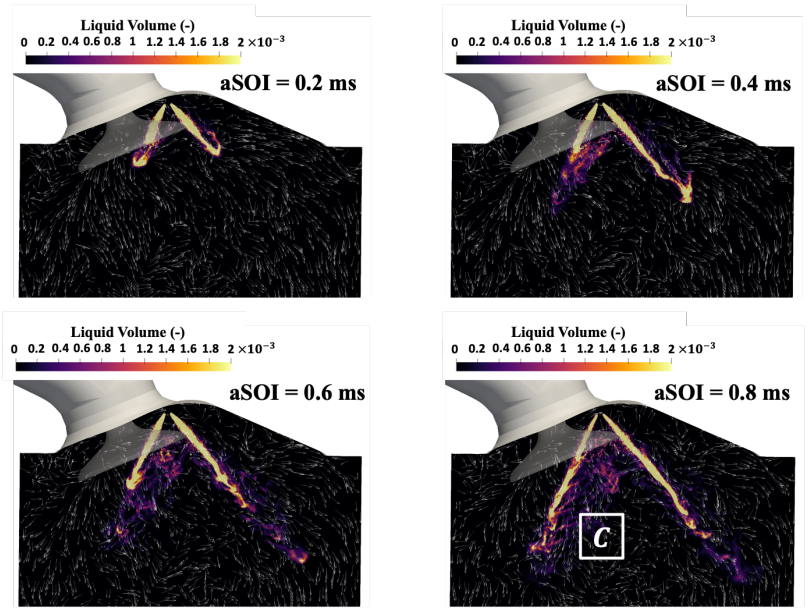

Figure 6.13: Evolution of Plume 5 (left) and 1 (right) at the central tumble plane in the case of 100% MFR. Note: the arrows show the plane velocity vector

The temporal evolution of Plumes 1 and 5 in the case of 100% MFR is shown in Figure 6.13. The arrows in the figure represent the velocity vector in the plane, while the colored contour indicates the liquid volume fraction of droplets, referred to as “voildFraction” in OpenFOAM. This liquid volume fraction is derived from each Lagrangian particle based on the number of droplets within it and their size.

The intake jet convergence region, denoted as B in Figure 5.4, is in the trajectory of Plume 5. Inevitably, Plume 5 must travel through this region throughout the whole injection. Consequently, as soon as Plume 5 reaches the convergence region, the disturbance occurs, causing the further breakup of spray and the dispersion and shifting of droplets towards the right. At aSOI $= 0.8$ ms, there are noticeable weak liquid volume signals of Plume 5, marked as C in Figure 6.13.

By contrast, Plume 1 follows the trend of the tumble vortex, labeled A in Figure 5.4. This vortex does not cause either counterflow or significant disturbance; instead, it propels

Plume 1 further downstream. This explains why the highest and lowest penetration lengths occur at the same plane and clarifies why Plume 5 exhibits the highest evaporation among the plumes.

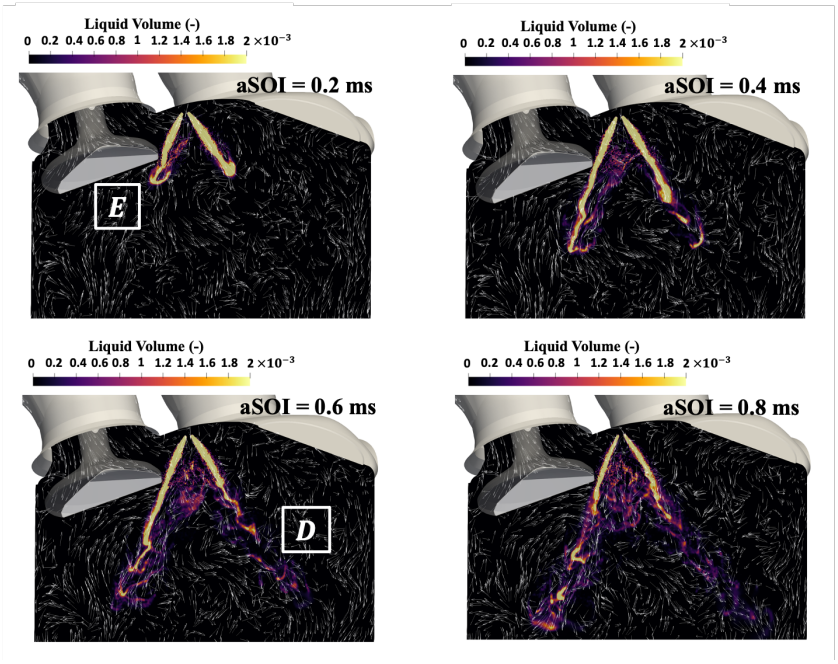

Figure 6.14: Evolution of Plume 4 (left) and 8 (right) at the cross-section plane in the case of 100% MFR. Note: the arrows show the plane velocity vector

Figure 6.14 focuses on the evolution of Plume 4 and Plume 8. In the previous discussion, it was mentioned that Plume 4 and Plume 6 exhibit the lowest evaporation and independent penetration with respect to the mass flow rate. Both of these plumes are located symmetrically to the central tumble plane and in proximity to the intake valves. On the other hand, Plume 2 and Plume 8, which are axisymmetric to the injector center, behave differently.

The evolution of Plume 8 shows that its structure remains intact until aSOI = 0.4 ms. However, at that point, Plume 8 encounters an intake-flow-induced vortex downstream, labeled D in Figure 6.14. This vortex causes additional breakups even though the spray is able to penetrate further. By contrast, the evolution of Plume 4 is different from that of Plume 8. Spray-wall interaction can be observed at aSOI = 0.2 ms, marked as E in Figure 6.14. Plume 4 hits the intake valve, and it causes the deformation of the spray

structure downstream. This deformation remains and can be observed at aSOI = 0.4 and 0.6 ms below the intake valve. However, spray-wall interaction does not affect the spray propagation, causing either strong breakup or dissipation. Nevertheless, together with the intake flow, it causes liquid droplets to dissipate toward the right.

As shown in Figure 6.13 and 6.14, a clear explanation can be found for why all the plumes behave distinctively and how the spray plume is deformed with mass flow rate due to the plumes' local flow. Throughout the injection, the spray does not penetrate long enough to hit the liner wall. However, spray-wall interaction occurs in Plumes 4 and 6 on the intake valves. In the real engine configuration, this can lead to soot formation as the fuel film develops and accumulates over multiple engine cycles.

Figure 6.15 provides a comparison of the deposited fuel film thickness on the intake valves at aSOI = 0.8 ms. At the end of the injection, the averaged thickness of the fuel film ranges from 2 to 5 µm in each case. Convection plays a role in enhancing evaporation and reducing the size and thickness of the fuel film. As the mass flow rate increases, the size and thickness of the fuel film decrease. Despite the symmetrical geometry of the intake valves and injector holes, the fuel film on the two valves takes on shapes that differ, although only by a minor amount, when the mass flow rates are varied. This phenomenon might be due to the variation of different plumes, and deviations in the statistical data over 25 cycles.

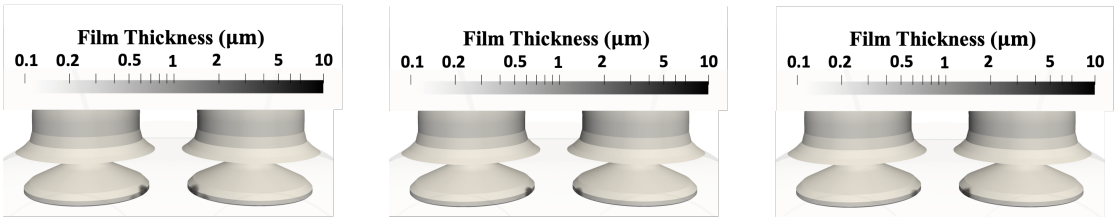

(a) 0% MFR (b) 50% MFR (c) 100% MFR

Figure 6.15: Fuel film deposits on the intake valves at aSOI = 0.8 ms

To quantitatively analyze the effect of convection on fuel film evaporation. Figure 6.16 compares the mass ratios of the fuel film. The mass ratio is normalized by the total injected mass (10 mg). The fuel film deposition reaches a steady state roughly after the injection is complete at aSOI = 0.78 ms for all cases. In no-flow cases, the overall deposited mass is 0.9% of the overall injected mass, whereas it makes up merely 0.6% and 0.4% in the case of 50% and 100% mass flow rates, respectively. Spray-wall interaction starts to take place at aSOI = 0.15 ms.

The convective evaporation effect can be observed from the beginning of spray-wall

interaction; during the early stage of the injection, fuel mass deposits exhibit a similar trend as the mass flow rate increases. This trend starts to deviate after aSOI = 0.4 ms; logically, less fuel accumulates on the valves in the 100% mass flow rate case.

Figure 6.16 suggests that increasing the mass flow rate effectively reduces the fuel film deposition. As mentioned previously, the 100% mass flow rate case is meant to simulate the motored engine at 800 rpm, which is a relatively low speed compared to real engine operating conditions. Furthermore, in this study, the spray injection pressure is set up as 200 bar. By increasing the injection pressure to 350 bar, which is the trend of GDI engines, the overall momentum of the spray and its transport increase, resulting in high evaporation and less fuel film deposits. Therefore, in real engines, the overall deposited mass may even be less than 0.4% of the total injected mass.

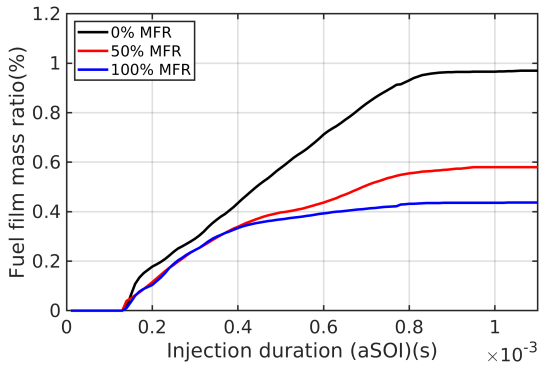

Figure 6.16: Time evolution of the fuel film mass ratio

In comparison to a constant-volume chamber with quiescent conditions, the evaporation of GDI spray within an engine flow bench is caused not only by the ambient temperature, pressure, and spray-induced turbulence but also by the in-cylinder flow producing spray-flow interaction.

6.3 Turbulence kinetic energy and spray

Spray-flow interaction in real engine applications has been extensively investigated and studied, in terms not only of spray formation but also of its impact on the global turbulence kinetic energy at the central tumble plane [25, 57]. Under the late-injection condition during the compression phase, in-cylinder flow is highly susceptible to the spray; the structure of the tumble flow can hardly preserve, and it is replaced by the counter-rotational flow due to spray-induced air entrainment [42, 57]. On the other hand, under

the early-injection condition, the in-cylinder flow pattern remains intact and has less influence from the spray as massive airflow travels through the intake ports toward the cylinder [25, 57]. In this case, the global turbulence kinetic energy resembles that of a motored engine without the presence of spray.

This section follows the research concepts mentioned above and aims to investigate the changes in the global turbulence kinetic energy during the injection process under different mass flow rates. The turbulence kinetic energy (TKE) is obtained by means of phased-averaged velocity fluctuation ($\overline{u_i'}$), which is in line with the definition of LES stating that the filtered velocity comprises the time-averaged velocity and filtered velocity fluctuation. This is written as:

$$\widetilde{u_i} = \overline{u}_i + \widetilde{u_i'} \tag{6.3}$$

To ensure that the comparison with experimental data is consistent, the turbulence kinetic energy (TKE) is presented as a two-dimensional quantity and can be calculated using the following formula:

$$\mathrm{TKE} = \frac{1}{2}(\overline{u_x'u_x'} + \overline{u_y'u_y'}) \tag{6.4}$$

where $\overline{u_x'}$ and $\overline{u_y'}$ represent the velocity fluctuations in the x and y directions, respectively.

Figure 6.17 shows an investigation of the global turbulence kinetic energy at the central tumble plane under different mass flow rates. The global turbulence kinetic energy represents the averaged TKE of the central tumble plane. To ensure that the intake flow is stable and minimize perturbations, the distance between the optical mirror and flow exit in the engine flow bench is extended up to 255 mm below the cylinder head, compared to the motored engine with its displacement of 86 mm, as shown in Figures 5.1 and 5.2. The domain of the central tumble plane examined is set to 50 mm below the cylinder head, providing a reasonable and consistent setup comparable to a motored engine, as shown in Figure 4 of a study by Welch et al. [24].

The global turbulence kinetic energy exhibits various initial values (aSOI = 0 ms) depending on the mass flow rate. However, during the injection, the maximum value of the global turbulence kinetic energy decreases as the mass flow rates increase. This observation indicates that even though the spray contributes to the global turbulence kinetic energy, the spray is disrupted by the in-cylinder flow, leading to the spray's dissipation. All three cases reach their peak turbulence kinetic energy values at approximately aSOI = 0.6 ms; thereupon, they start to decay after the injection ends (aSOI = 0.78 ms) toward their initial value before the injection. This behavior aligns well with the findings from motored engine cases under early-injection conditions [25]. During the injection, the

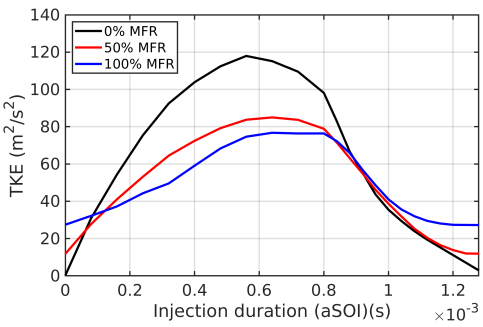

(a) Evolution of the time-averaged global turbulence kinetic energy

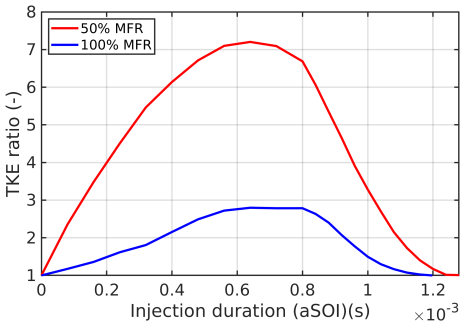

(b) Evolution of the time-averaged global turbulence kinetic energy ratio

Figure 6.17: Comparison of the time-average global turbulence kinetic energy at the central tumble plane during the injection. Note: the TKE ratio is normalized by the global TKE before injection with different mass flow rates.

high-speed spray-air-entrainment flow contributes to an increase in turbulence. However, as the injection comes to an end, the turbulence gradually dissipates.

Figure 6.17 (b) provides a ratio that normalizes the global turbulence kinetic energy by its initial value before the injection. The 50% mass flow case shows an escalation of the global turbulence kinetic energy up to 7 times its value before the injection, while the 100% mass flow rate case exhibits a threefold enhancement. This suggests that increasing the mass flow rate intensifies the disturbance of the spray formation and potentially improves the air-fuel mixture.

6.4 Conclusion

Extending the research from a constant-volume chamber toward an engine flow bench provides further insights into real engine applications under early-injection conditions. This study offers a more comprehensive characterization of the spray-flow interaction on each spray plume. Furthermore, spray-wall interaction and fuel film deposits with different MFRs are also discussed. Several findings are summarized as follows:

- The spray-flow interaction becomes more intensive as mass flow rates increase. Due to the influence of the intake flow, spray plumes are shifted rightward toward the exhaust ports. These findings are consistent in both the experiments and the simulations.

- The deformation of spray plumes can be misleading if one solely relies on global quantities, such as the penetration length, spray angle, and axisymmetric factor. Spray plumes behave heterogeneously associated with their local characteristic flows. The turbulence in the jet convergence region in the central tumble plane effectively disrupts Plume 5, leading to significant spray deformation and evaporation.
- By investigating the heterogeneous behavior of all spray plumes, spray plumes oriented along the intake flow jet exhibit higher penetration and lower evaporation, whereas those not oriented along the intake jet stream exhibit higher evaporation and reduced penetration. This confirms the influence of the air entrainment induced by the intake flow affects evaporation and penetration length.
- Wall wetting is observed on the intake valves in this study; however, it does not affect spray formation despite the distortion of the spray plumes (Plumes 4 and 6) after the occurrence. Convective evaporation effectively reduces the fuel film, cutting the residual mass of the fuel film by up to 50% compared to the no-flow case when the mass flow rate is 100%.
- Under early-injection conditions, the global turbulence kinetic energy eventually returns to its original values after the injection, although a ramp-up of its values during the injection can be observed due to the spray-air-entrainment-induced turbulence. This phenomenon agrees well with experimental research based on motored engines under early-injection conditions. Evidence of the spray-flow interaction indicates that the higher the mass flow rate, the less the global turbulence kinetic energy ramps up during injection.

7 Conclusion and outlook

With the ever-increasing computational resources for numerical simulations and the pressing need to regulate zero-carbon emissions, the development of a suite of high-fidelity models for GDI spray becomes imperative. This dissertation contributes to this challenge, encompassing the formulation of robust Lagrangian frameworks and an exhaustive investigation of the salient physics intrinsic to a spectrum of operational states, extending from early- to late-injection conditions. These models have been extensively validated, not only within a constant-volume chamber but also in a GDI engine flow bench, ensuring their reliability and accuracy.

The conceptual foundation of these models is rooted in a DNS inner-nozzle study [4], which suggests that the liquid spray experiences complete atomization in the vicinity of the injector hole. As a consequence, the deformation and secondary breakup of liquid droplets dominate the entire spray evolution. Through thorough validation against experimental data, encompassing both liquid and vapor phases obtained by DBI and Schlieren measurements, respectively, the efficacy of the models has been established.

A noteworthy aspect of this research lies in the investigation of different droplet distribution models. While the blob method, assuming ejected droplet size to be equivalent to the injector diameter, can accurately capture global properties like liquid penetration length, it tends to cause delayed evaporation and breakup, leading to an unphysical sharp plume tip downstream. To strive towards a future of synthesized fuel-blended gasoline, the models have been extended to handle multi-component fuels. The successful simulation of a three-component gasoline surrogate (E00) [110] demonstrates the models' capability to reproduce not only the overall spray plume characteristics but also the spatial distribution of high- and low-volatile fuels.

Furthermore, the research extends further toward the intricate spray-wall interaction within a constant-volume chamber under simulated cold start conditions. The simulation replicates characteristic flows, such as wall jets and wall jet vortices, induced by this interaction. Moreover, the phenomenon of spray cooling, resulting from air-entrainment-induced evaporation, is accurately reproduced, with simulated temperatures closely aligned with 0-D analytical results [63]. Due to the constant temperature boundary condition, the heat transfer from the wall is overpredicted. Nevertheless, the simulation

successfully matches the experimental aggregate data concerning wall film thickness.

To comprehensively examine spray-wall-flow interaction within a GDI engine, it is imperative to understand the in-cylinder flow during the intake phase. To this end, a scale-resolved LES approach is employed to investigate free-stream and near-wall turbulence within an engine flow bench, simplifying the inherent complexity of the engine flow and focusing on the intake flow. The simulated in-cylinder large-scale motion and turbulence structure aligns well with reference experimental PIV data. The turbulence anisotropy analysis reveals a strong orientation toward axisymmetric expansion and contraction, corresponding to vortex compression and stretching, respectively. This is attributed to the specific topological pattern of the engine flow, characterized by the tumble vortex and the intake overflow jet.

Moreover, the near-wall budget analysis facilitates investigating near-wall non-equilibrium effects, with a particular focus on the intake valve and liner wall region. The intake flow with a high *Re* number induces a substantial pressure gradient, and the non-equilibrium effects are found to vary across different regions. The effects of the pressure gradient are found to be significant. This suggests that the classical wall function modeling approach based on the classical zero pressure gradient boundary layer may no longer be valid in ICE applications.

Ultimately, the culmination of the acquired knowledge is applied to the assessment of the spray-wall-flow interaction in an engine flow bench under various MFRs. As MFRs increase, the spray-flow interaction intensifies, and the heterogeneous behavior of all spray plumes becomes apparent. Plumes oriented along the intake flow jet exhibit higher penetration and lower evaporation, while those not aligned with the intake jet stream exhibit increased evaporation and reduced penetration. This observation confirms the significant impact of air entrainment induced by the intake flow on both evaporation and penetration length. Additionally, wall wetting is observed on the intake valves, and convective evaporation effectively reduces the fuel film, cutting its residual mass by up to 50% compared to the no-flow case when the mass flow rate is 100%. Under early-injection conditions, although the global turbulence kinetic energy experiences a transient increase during the injection, it eventually returns to its original values.

In conclusion, the work presented in this thesis represents a substantial advancement in the field of GDI spray modeling. The developed suite of Lagrangian models, rooted in DNS insights, showcases great accuracy and reliability in reproducing complex spray dynamics under various conditions. Extending the models to handle multi-component fuels and exploring spray-wall interactions within an engine flow bench provides valuable insights into critical phenomena that impact the efficiency and emissions of GDI engines. The findings contribute significantly to the ongoing efforts to achieve more environmentally friendly and sustainable transportation solutions.

7.1 Future work

The future work derived from this research aims to address the complexities and challenges posed by real ICE applications, with a particular focus on e-fuels and synthesized fuel-blended gasoline. To further enhance the suite of Lagrangian models and spray-wall interaction strategy, the following steps will be taken:

1. Conjugate Heat Transfer Model (CHT) Implementation:
    - Introduce a conjugate heat transfer model (CHT) to establish a coupling between the fuel film and the solid wall, addressing the fact that real wall boundaries do not maintain a constant temperature.
    - This addition will enable a more accurate representation of heat transfer processes, which play a crucial role in the interaction between the fuel spray and engine components.
2. Multi-Component Fuel Simulation:
    - Develop a comprehensive framework capable of accurately simulating multi-component fuels, including e-fuels (such as methanol and hydrogen) and synthesized fuel-blended gasoline (e.g., E10 and E85).
    - Address the challenges associated with solving heat and mass transfer accurately for each fuel, accounting for their unique characteristics, such as density, diffusivity, and volatility.
3. Incorporation of Real or Synthesized Fuel-Blended Gasoline:
    - Recognize that conventional gasoline surrogate (pure iso-octane) may not fully capture the characteristics of real or synthesized fuel-blended gasoline, especially when dealing with highly volatile fuels like e-fuels and blended ones with higher volatility. [43, 44, 112]
    - Account for the effects of boiling and flash boiling regimes, where liquid droplets undergo intense evaporation not only from the surface but also from within. Consider the potential influence of bubble-induced breakup on spray dynamics.

List of Symbols

Characteristic number

F_{α}	Spray axisymmetric factor
B_m	Spalding mass number
$C_{D,sphere}$	Sphere drag coefficient
C_D	Drag coefficient
C_d	Discharge coefficient
IQ_{LES}	LES quality index
R_p	Pressure ratio for boiling regime
La	Laplace number
Le	Lewis number
Nu	Nusselt number
Oh	Ohnesorge number
Pr	Prandtl number
Re	Reynolds number
Sc	Schmidt number
Sh	Sherwood number
We	Weber number
F	Turbulence anisotropy intensity

Greek Symbols

α_ν	Constant of LES quality index
α_s	Overall heat transfer coefficient
β	Non-dimensional evaporation parameter
Δ	Filter width
ϵ_k	Turbulence dissipation
η	Non-dimensional parameter of the turbulence anisotropy invariant map
μ_t	Sub-grid viscosity
ν	Molecular viscosity
$\nu_{t,eff}$	Effective viscosity
ν_t	Eddy viscosity
Φ	Arbitrary extensive quantity
ϕ	Sphericity
$\phi_\perp$	Crosswise sphericity
π	Ratio of the circumference of a circle to its diameter
Π_{tke}	Turbulence pressure diffusion
ρ	Density
σ_i	Singular value of the resolved velocity gardient tensor
τ_d	Particle time constant for Stokes flow
ξ	Non-dimensional parameter of the turbulence anisotropy invariant map

Latin Symbols

ΔV	Volume of each Eulerain cell
A_{inj}	Cross-section area of each injector hole

B_0	KH-RT breakup model constant
B_1	KH-RT breakup model constant
b_{ij}	Reynolds stress anisotropy tensor
C_σ	Model constant for sigma model
$c_{p,k}$	Specific heat of each specie
C_{rt}	KH-RT breakup model constant
d	Diameter
$D_{k,i}$	Diffusion coefficient
D_{tke}	Viscous diffusion
e	Eccentricity of droplet
E_D	Dissipation during the splash
$E_{I\sigma}$	Total kinetic energy of incident splashed droplets
E_{KI}	Total kinetic energy of incident splashed droplets
E_{KS}	Total kinetic energy of residual splashed droplets
$E_{S\sigma}$	Total surface energy of residual splashed droplets
f_k	Volume force on species k
g_{ij}	Velocity gradient tensor
g_i	Gravitational acceleration
h	Specific enthalpy
$h^0_{f,k}$	Enthalpy formation for each specie
h_c	Heat transfer coefficient
h_s	Sensible enthalpy
h_t	Total enthalpy

h_v	heat of vaporization
I	Turbulence intensity
k_g	Thermal conductivity
m	Mass
M_k	Molecular mass
M_{ratio}	Splash mass ratio
N	Total number of the Lagrangian particles within the Eulerian cell
p	pressure
P_k	Turbulence production
R	Universal gas constant
r	Radius
r_j	Region radius of the filter kernel
s	Mask threshold of spray Mie signal
S_{Mie}	Numerical Mie signal
S_ρ	Source term of liquid fuel phase change
S_{h_t}	Source term of enthalpy exchange
S_{ij}	Rate of strain tensor
S_{u_i}	Source term of liquid fuel momentum exchange
S_{Y_k}	Source term of liquid fuel phase change of each species
$SrfC_p$	Surface area of the droplet
T	Temperature
T_{tke}	Turbulence diffusion
u	Velocity

u_τ	Near-wall scaling friction velocity
u_{conv}	Near-wall scaling on convection
u_p	Near-wall scaling on streamwise pressure gradient
$V_{k,i}$	Diffusion velocity
X	Mole fraction
x^+	non-dimensional wall-streamwise distance
x_i	Center point of the filter kernel
y	Droplet distortion factor
y^+	non-dimensional wall-normal distance
Y_k	Mass fraction of each specie
z^+	non-dimensional wall-spanwise distance
III	Turbulence anisotropy invariant
II	Turbulence anisotropy invariant
I	Turbulence anisotropy invariant

Operators

$\int$	Integration
$\overline{(.)}$	Time-avergaed
$\sum$	Summation
$\nabla.$	Gradient
$\widehat{(.)}$	Scale-separating filter
$\widetilde{(.)}$	Favre filter

Subscripts

$(.)_{boiling}$	Boiling regime

$(.)_g$	Gas phase
$(.)_p$	Liquid particles
$(.)_t$	Sub-grid

Acronyms

LES Large Eddy Simulation

DNS Direct Numerical Simulation

RANS Reynolds-averaged Navier Stokes

aSOI after the start of injection

DBI diffuse back-illumination

ICEs internal combustion engines

DISI direct-injection spark-ignition

SI spark-ignition

GDI gasoline direct-injection

PFI port fuel injection

ECN Engine Combustion Network

PIV particle image velocimetry

TPIV tomographic particle image velocimetry

DBI diffuse back-illumination

LIF laser-induced fluorescence

LCI low-coherence interferometry

TKE turbulence kinetic energy

CDF cumulative distribution function

PLV projected liquid volume

LVF liquid volume fraction

PDI phase-doppler interferometry

MFR mass flow rate

MFRs mass flow rates

PLIF planar laser-induced fluorescence

List of Figures

List of Tables

Bibliography

[1] Hao-Pin Lien et al. “Numerical studies of gasoline direct-injection sprays (ECN Spray G) under early- and late-injection conditions using Large Eddy Simulation and droplets-statistics-based Eulerian–Lagrangian framework”. en. In: *Fuel* 357 (Feb. 2024), p. 129708. ISSN: 00162361. DOI: 10.1016/j.fuel.2023.129708. URL: https://linkinghub.elsevier.com/retrieve/pii/S0016236123023220.

[2] Hao-Pin Lien et al. “Characteristics of near-wall flow and free-stream turbulence during the intake phase of a direct-injection engine”. In: *Int J Heat Fluid Flow* (2023).

[3] Hao-Pin Lien et al. “Spray formation and spray-wall-flow interaction within a gasoline direct-injection (GDI) engine under early-injection conditions – a flow bench study”. In: *Int. J. Engine Res.* (2023).

[4] Yongxiang Li et al. “Direct Numerical Simulation of Atomization Characteristics of ECN Spray-G Injector: In-Nozzle Fluid Flow and Breakup Processes”. In: *Flow Turbul. Combust* (2023). DOI: 10.1007/s10494-023-00514-2.

[5] Graham Conway et al. “A review of current and future powertrain technologies and trends in 2020”. In: *Transportation Engineering* 5 (Sept. 1, 2021), p. 100080. ISSN: 2666-691X. DOI: 10.1016/j.treng.2021.100080. URL: https://www.sciencedirect.com/science/article/pii/S2666691X21000361 (visited on 03/15/2023).

[6] Ziyoung Lee et al. “Review on spray, combustion, and emission characteristics of recent developed direct-injection spark ignition (DISI) engine system with multi-hole type injector”. In: *Fuel* 259 (Jan. 2020), p. 116209. ISSN: 00162361. DOI: 10.1016/j.fuel.2019.116209. URL: https://linkinghub.elsevier.com/retrieve/pii/S0016236119315637 (visited on 03/14/2023).

[7] EPA. *The 2022 EPA Automotive Trends Report*. Dec. 2022.

[8] Hua Zhao. *Advanced direct injection combustion engine technologies and development*. Woodhead Publishing in mechanical engineering. Boca Raton: CRC Press, 2010.

[9] Eshan Singh et al. “Particulate Matter Emissions in Gasoline Direct-Injection Spark-Ignition Engines: Sources, Fuel Dependency, and Quantities”. In: *Fuel* 338 (Apr. 2023), p. 127198. ISSN: 00162361. DOI: 10.1016/j.fuel.2022.127198. URL: https://linkinghub.elsevier.com/retrieve/pii/S0016236122040224 (visited on 03/13/2023).

[10] Namho Kim et al. “Ability of Particulate Matter Index to describe sooting tendency of various gasoline formulations in a stratified-charge spark-ignition engine”. In: *Proceedings of the Combustion Institute* 38.4 (2021), pp. 5791–5799. ISSN: 15407489. DOI: 10.1016/j.proci.2020.06.173. URL: https://linkinghub.elsevier.com/retrieve/pii/S1540748920302625 (visited on 03/14/2023).

[11] F. Zhao, M. C. Lai, and D. L. Harrington. *Automotive Spark-Ignited Direct-Injection Gasoline Engines*. OCLC: 437191525. Burlington: Elsevier, 2000. ISBN: 978-0-08-055279-8.

[12] H. Zhao. “Overview of gasoline direct injection engines”. In: *Advanced Direct Injection Combustion Engine Technologies and Development*. Elsevier, 2010, pp. 1–19. ISBN: 978-1-84569-389-3. DOI: 10.1533/9781845697327.1. URL: https://linkinghub.elsevier.com/retrieve/pii/B9781845693893500013 (visited on 06/12/2023).

[13] U. Spicher and T. Heidenreich. “Stratified-charge combustion in direct injection gasoline engines”. In: *Advanced Direct Injection Combustion Engine Technologies and Development*. Elsevier, 2010, pp. 20–44. ISBN: 978-1-84569-389-3. DOI: 10.1533/9781845697327.20. URL: https://linkinghub.elsevier.com/retrieve/pii/B9781845693893500025 (visited on 06/12/2023).

[14] Ch. Schwarz et al. “Potentials of the Spray-Guided BMW DI Combustion System”. In: SAE 2006 World Congress & Exhibition. Apr. 3, 2006, pp. 2006--01–1265. DOI: 10.4271/2006-01-1265. URL: https://www.sae.org/content/2006-01-1265/ (visited on 06/12/2023).

[15] Florian Schumann et al. “Potential of spray-guided gasoline direct injection for reduction of fuel consumption and simultaneous compliance with stricter emissions regulations”. In: *International Journal of Engine Research* 14.1 (Feb. 2013), pp. 80–91. ISSN: 1468-0874, 2041-3149. DOI: 10.1177/1468087412451695. URL:

http://journals.sagepub.com/doi/10.1177/1468087412451695 (visited on 06/12/2023).

[16] P. G. Hill and D. Zhang. *The effects of swirl and tumble on combustion in spark-ignition engines*. ISSN: 03601285 Issue: 5 Pages: 373–429 Publication Title: Progress in Energy and Combustion Science Volume: 20. Jan. 1994. DOI: 10.1016/0360-1285(94)90010-8.

[17] Rodney J. Tabaczynski. "Turbulence and turbulent combustion in spark-ignition engines". In: *Progress in Energy and Combustion Science* 2.3 (Jan. 1976). Publisher: Pergamon, pp. 143–165. ISSN: 03601285. DOI: 10.1016/0360-1285(76)90010-1.

[18] Stefan Buhl et al. "Investigation of an IC Engine Intake Flow Based on Highly Resolved LES and PIV". In: *Oil Gas Sci. Technol. – Rev. IFP Energies nouvelles* 72.3 (May 2017), p. 15. ISSN: 1294-4475, 1953-8189. DOI: 10.2516/ogst/2017012. URL: http://ogst.ifpenergiesnouvelles.fr/10.2516/ogst/2017012 (visited on 12/16/2022).

[19] Peter C Ma et al. "Non-equilibrium wall-modeling for internal combustion engine simulations with wall heat transfer". In: *International Journal of Engine Research* 18.1 (Feb. 2017), pp. 15–25. ISSN: 1468-0874, 2041-3149. DOI: 10.1177/1468087416686699. URL: http://journals.sagepub.com/doi/10.1177/1468087416686699 (visited on 12/16/2022).

[20] Daniel Freudenhammer et al. "Volumetric intake flow measurements of an IC engine using magnetic resonance velocimetry". In: *Experiments in Fluids* 55.5 (2014). ISSN: 07234864. DOI: 10.1007/s00348-014-1724-6.

[21] Daniel Freudenhammer et al. "The Influence of Cylinder Head Geometry Variations on the Volumetric Intake Flow Captured by Magnetic Resonance Velocimetry". In: *SAE Int. J. Engines* 8.4 (Apr. 14, 2015), pp. 1826–1836. ISSN: 1946-3944. DOI: 10.4271/2015-01-1697. URL: https://www.sae.org/content/2015-01-1697/ (visited on 12/16/2022).

[22] B. Peterson et al. "Assessment and application of tomographic PIV for the spray-induced flow in an IC engine". In: *Proceedings of the Combustion Institute* 36.3 (2017), pp. 3467–3475. ISSN: 1540-7489. DOI: https://doi.org/10.1016/j.proci.2016.06.114.

[23] Brian Peterson et al. “Spray-induced temperature stratification dynamics in a gasoline direct-injection engine”. In: *Proceedings of the Combustion Institute* 35.3 (2015), pp. 2923–2931. ISSN: 15407489. DOI: 10.1016/j.proci.2014.06.103. URL: https://linkinghub.elsevier.com/retrieve/pii/S1540748914002612 (visited on 01/12/2023).

[24] Cooper Welch et al. “Experimental characterization of the turbulent intake jet in an engine flow bench”. In: *Exp Fluids* 64.5 (May 2023), p. 91. ISSN: 0723-4864, 1432-1114. DOI: 10.1007/s00348-023-03640-9. URL: https://link.springer.com/10.1007/s00348-023-03640-9 (visited on 06/07/2023).

[25] Cooper Welch et al. “The influence of in-cylinder flows and bulk gas density on early Spray G injection in an optical research engine”. In: *International Journal of Engine Research* 24.1 (Jan. 2023), pp. 82–98. ISSN: 1468-0874, 2041-3149. DOI: 10.1177/14680874211042320. URL: http://journals.sagepub.com/doi/10.1177/14680874211042320 (visited on 03/19/2023).

[26] Florian Zentgraf et al. “On the turbulent flow in piston engines: Coupling of statistical theory quantities and instantaneous turbulence”. In: *Physics of Fluids* 28.4 (Apr. 2016). Publisher: American Institute of Physics Inc., p. 45108. ISSN: 10897666. DOI: 10.1063/1.4945785. URL: https://doi.org/10.1063/1.494578528,045108.

[27] Peter C. Ma et al. “Development and Analysis of Wall Models for Internal Combustion Engine Simulations Using High-speed Micro-PIV Measurements”. In: *Flow Turbulence Combust* 98.1 (Jan. 2017), pp. 283–309. ISSN: 1386-6184, 1573-1987. DOI: 10.1007/s10494-016-9734-5. URL: http://link.springer.com/10.1007/s10494-016-9734-5 (visited on 12/16/2022).

[28] Marc Haussmann et al. “Evaluation of a Near-Wall-Modeled Large Eddy Lattice Boltzmann Method for the Analysis of Complex Flows Relevant to IC Engines”. In: *Computation* 8.2 (May 5, 2020), p. 43. ISSN: 2079-3197. DOI: 10.3390/computation8020043. URL: https://www.mdpi.com/2079-3197/8/2/43 (visited on 12/16/2022).

[29] Tobias Falkenstein et al. “Large-Eddy Simulation Study on Unsteady Effects in a Statistically Stationary SI Engine Port Flow”. In: SAE 2015 World Congress & Exhibition. Apr. 14, 2015, pp. 2015--01–0373. DOI: 10.4271/2015-01-0373. URL: https://www.sae.org/content/2015-01-0373/ (visited on 12/16/2022).

[30] Tobias Falkenstein et al. “LES of Internal Combustion Engine Flows Using Cartesian Overset Grids”. In: *Oil & Gas Science and Technology - Rev. IFP Energies nouvelles* 72.6 (Nov. 2017). Ed. by C. Angelberger, p. 36. ISSN: 1294-4475, 1953-8189. DOI: 10.2516/ogst/2017026. URL: http://ogst.ifpenergiesnouvelles.fr/10.2516/ogst/2017026 (visited on 12/16/2022).

[31] Karri Keskinen et al. “Numerical assessment of wall modelling approaches in scale-resolving in-cylinder simulations”. In: *International Journal of Heat and Fluid Flow* 74 (Dec. 2018), pp. 154–172. ISSN: 0142727X. DOI: 10.1016/j.ijheatfluidflow.2018.09.016. URL: https://linkinghub.elsevier.com/retrieve/pii/S0142727X1830002X (visited on 11/29/2022).

[32] Martin Schmitt et al. “Investigation of wall heat transfer and thermal stratification under engine-relevant conditions using DNS”. In: *International Journal of Engine Research* 17.1 (Jan. 2016), pp. 63–75. ISSN: 1468-0874, 2041-3149. DOI: 10.1177/1468087415588710. URL: http://journals.sagepub.com/doi/10.1177/1468087415588710 (visited on 06/13/2023).

[33] Frank Hartmann et al. “Spatially Resolved Experimental and Numerical Investigation of the Flow through the Intake Port of an Internal Combustion Engine”. In: *Oil Gas Sci. Technol. – Rev. IFP Energies nouvelles* 71.1 (Jan. 2016), p. 2. ISSN: 1294-4475, 1953-8189. DOI: 10.2516/ogst/2015022. URL: http://ogst.ifpenergiesnouvelles.fr/10.2516/ogst/2015022 (visited on 12/16/2022).

[34] Kaushal Nishad et al. “Numerical Investigation of Flow through a Valve during Charge Intake in a DISI -Engine Using Large Eddy Simulation”. In: *Energies* 12.13 (2019), p. 2620. ISSN: 1996-1073. DOI: 10.3390/en12132620.

[35] Tobias Falkenstein et al. “Experiments and Large-Eddy Simulation for a Flowbench Configuration of the Darmstadt Optical Engine Geometry”. In: *SAE Int. J. Engines* 13.4 (July 8, 2020), pp. 03--13--04–0032. ISSN: 1946-3944. DOI: 10.4271/03-13-04-0032. URL: https://www.sae.org/content/03-13-04-0032/ (visited on 12/16/2022).

[36] Marianna Migliaccio et al. “CFD Modeling and Validation of the ECN Spray G Experiment under a Wide Range of Operating Conditions”. In: Sept. 2019, pp. 2019--24–0130. DOI: 10.4271/2019-24-0130. URL: https://www.sae.org/content/2019-24-0130/ (visited on 11/22/2023).

[37] Marianna Migliaccio et al. “Numerical Investigation on GDI Spray under High Injection Pressure up to 100 MPa”. In: Sept. 2020, pp. 2020--01–2108. DOI: 10.4271/2020-01-2108. URL: https://www.sae.org/content/2020-01-2108/ (visited on 11/21/2023).

[38] N. Mitroglou et al. “Spray Structure Generated by Multi-Hole Injectors for Gasoline Direct-Injection Engines”. In: SAE World Congress & Exhibition. Apr. 16, 2007, pp. 2007--01–1417. DOI: 10.4271/2007-01-1417. URL: https://www.sae.org/content/2007-01-1417/.

[39] Volker Sick, Michael C. Drake, and Todd D. Fansler. “High-speed imaging for direct-injection gasoline engine research and development”. In: *Exp Fluids* 49.4 (Oct. 2010), pp. 937–947. ISSN: 0723-4864, 1432-1114. DOI: 10.1007/s00348-010-0891-3. URL: http://link.springer.com/10.1007/s00348-010-0891-3.

[40] Guy Hoffmann et al. “Fuel System Pressure Increase for Enhanced Performance of GDi Multi-Hole Injection Systems”. In: *SAE Int. J. Engines* 7.1 (Apr. 1, 2014), pp. 519–527. ISSN: 1946-3944. DOI: 10.4271/2014-01-1209. URL: https://www.sae.org/content/2014-01-1209/.

[41] Kaushik Saha et al. “Coupled Eulerian Internal Nozzle Flow and Lagrangian Spray Simulations for GDI Systems”. In: WCX™ 17: SAE World Congress Experience. Mar. 28, 2017, pp. 2017--01–0834. DOI: 10.4271/2017-01-0834. URL: https://www.sae.org/content/2017-01-0834/.

[42] Christopher Geschwindner et al. “Analysis of the interaction of Spray G and in-cylinder flow in two optical engines for late gasoline direct injection”. In: *International Journal of Engine Research* 21.1 (Jan. 2020), pp. 169–184. ISSN: 1468-0874, 2041-3149. DOI: 10.1177/1468087419881535. URL: http://journals.sagepub.com/doi/10.1177/1468087419881535 (visited on 01/12/2023).

[43] Tawfik Badawy, Hongming Xu, and Yanfei Li. “Macroscopic spray characteristics of iso-octane, ethanol, gasoline and methanol from a multi-hole injector under flash boiling conditions”. In: *Fuel* 307 (Jan. 2022), p. 121820. ISSN: 00162361. DOI: 10.1016/j.fuel.2021.121820. URL: https://linkinghub.elsevier.com/retrieve/pii/S0016236121016999 (visited on 02/08/2023).

[44] P.G. Aleiferis and Z.R. van Romunde. “An analysis of spray development with iso-octane, n-pentane, gasoline, ethanol and n-butanol from a multi-hole injector under hot fuel conditions”. In: *Fuel* 105 (Mar. 2013), pp. 143–168. ISSN: 00162361.

DOI: 10.1016/j.fuel.2012.07.044. URL: https://linkinghub.elsevier.com/retrieve/pii/S0016236112005935 (visited on 01/30/2023).

[45] Masayuki Adachi et al. “Characterization of Fuel Vapor Concentration Inside a Flash Boiling Spray”. In: International Congress & Exposition. Feb. 24, 1997, p. 970871. DOI: 10.4271/970871. URL: https://www.sae.org/content/970871/ (visited on 06/18/2023).

[46] Zhenhua An, Jiangkuan Xing, and Ryoichi Kurose. “Numerical Study on the Phase Change and Spray Characteristics of Liquid Ammonia Flash Spray”. In: *SSRN Journal* (2022). ISSN: 1556-5068. DOI: 10.2139/ssrn.4313224. URL: https://www.ssrn.com/abstract=4313224 (visited on 02/08/2023).

[47] Engine Combustion Network. *Sandia Spray G Data*. Engine Combustion Network. URL: https://ecn.sandia.gov/data/sandia-spray-g-data/ (visited on 02/03/2023).

[48] Joonsik Hwang et al. “Spatio-temporal identification of plume dynamics by 3D computed tomography using engine combustion network spray G injector and various fuels”. In: *Fuel* 280 (Nov. 2020), p. 118359. ISSN: 00162361. DOI: 10.1016/j.fuel.2020.118359. URL: https://linkinghub.elsevier.com/retrieve/pii/S0016236120313557 (visited on 01/31/2023).

[49] Daniel J. Duke et al. “Time-resolved X-ray Tomography of Gasoline Direct Injection Sprays”. In: *SAE Int. J. Engines* 9.1 (Sept. 1, 2015), pp. 143–153. ISSN: 1946-3944. DOI: 10.4271/2015-01-1873. URL: https://www.sae.org/content/2015-01-1873/ (visited on 01/31/2023).

[50] Daniel J. Duke et al. “Internal and near nozzle measurements of Engine Combustion Network “Spray G” gasoline direct injectors”. In: *Experimental Thermal and Fluid Science* 88 (Nov. 2017), pp. 608–621. ISSN: 08941777. DOI: 10.1016/j.expthermflusci.2017.07.015. URL: https://linkinghub.elsevier.com/retrieve/pii/S089417771730211X (visited on 01/20/2023).

[51] Lukas Weiss et al. “Development of limited-view tomography for measurement of Spray G plume direction and liquid volume fraction”. In: *Exp Fluids* 61.2 (Feb. 2020), p. 51. ISSN: 0723-4864, 1432-1114. DOI: 10.1007/s00348-020-2885-0. URL: http://link.springer.com/10.1007/s00348-020-2885-0.

[52] Davide Paredi et al. “Combined Experimental and Numerical Investigation of the ECN Spray G under Different Engine-Like Conditions”. In: WCX World Congress Experience. Apr. 3, 2018, pp. 2018--01–0281. DOI: 10.4271/2018-01-0281.

URL: https://www.sae.org/content/2018-01-0281/ (visited on 01/23/2023).

[53] Francesco Duronio et al. “ECN Spray G: Coupled Eulerian internal nozzle flow and Lagrangian spray simulation in flash boiling conditions”. In: *International Journal of Engine Research* (Apr. 5, 2022), p. 146808742210907. ISSN: 1468-0874, 2041-3149. DOI: 10.1177/14680874221090732. URL: http://journals.sagepub.com/doi/10.1177/14680874221090732.

[54] Bizhan Befrui et al. “ECN GDi Spray G: Coupled LES Jet Primary Breakup - Lagrangian Spray Simulation and Comparison with Data”. In: 2016.

[55] Andrea Pati et al. “Numerical and experimental investigations of the early injection process of Spray G in a constant volume chamber and an optically accessible DISI engine”. In: *International Journal of Engine Research* 23.12 (Dec. 2022), pp. 2073–2093. ISSN: 1468-0874, 2041-3149. DOI: 10.1177/14680874211039422. URL: http://journals.sagepub.com/doi/10.1177/14680874211039422 (visited on 01/23/2023).

[56] Fabien Tagliante et al. “Large-Eddy Simulation of Laser-Ignited Direct Injection Gasoline Spray for Emission Control”. In: *Energies* 14.21 (Nov. 3, 2021), p. 7276. ISSN: 1996-1073. DOI: 10.3390/en14217276. URL: https://www.mdpi.com/1996-1073/14/21/7276.

[57] Hao Chen et al. “Influence of Early and Late Fuel Injection on Air Flow Structure and Kinetic Energy in an Optical SIDI Engine”. In: WCX World Congress Experience. Apr. 3, 2018, pp. 2018--01–0205. DOI: 10.4271/2018-01-0205. URL: https://www.sae.org/content/2018-01-0205/ (visited on 05/17/2023).

[58] M. C. Drake et al. “Piston Fuel Films as a Source of Smoke and Hydrocarbon Emissions from a Wall-Controlled Spark-Ignited Direct-Injection Engine”. In: SAE 2003 World Congress & Exhibition. Mar. 3, 2003, pp. 2003--01–0547. DOI: 10.4271/2003-01-0547. URL: https://www.sae.org/content/2003-01-0547/ (visited on 06/14/2023).

[59] Eric Stevens and Richard Steeper. “Piston Wetting in an Optical DISI Engine: Fuel Films, Pool Fires, and Soot Generation”. In: SAE 2001 World Congress. Mar. 5, 2001, pp. 2001--01–1203. DOI: 10.4271/2001-01-1203. URL: https://www.sae.org/content/2001-01-1203/ (visited on 06/14/2023).

[60] Kazuya Miyashita et al. “High-Speed UV and Visible Laser Shadowgraphy of GDI In-Cylinder Pool Fire”. In: SAE 2016 International Powertrains, Fuels & Lubricants Meeting. Oct. 17, 2016, pp. 2016--01–2165. DOI: 10.4271/2016-01-2165. URL: https://www.sae.org/content/2016-01-2165/ (visited on 06/14/2023).

[61] Logan White, Julien Manin, and Lyle M. Pickett. “High-speed low-coherence interferometry for film thickness measurements in impinging gasoline direct injection sprays”. In: *COMODIA* 2022.10.0 (2022), pp. C3–3. ISSN: 2424-2918. DOI: 10.1299/jmsesdm.2022.10.C3-3. URL: https://www.jstage.jst.go.jp/article/jmsesdm/2022.10/0/2022.10_C3-3/_article (visited on 06/08/2023).

[62] Mong-Tung Lin and Volker Sick. “Is Toluene a Suitable LIF Tracer for Fuel Film Measurements?” In: SAE 2004 World Congress & Exhibition. Mar. 8, 2004, pp. 2004--01–1355. DOI: 10.4271/2004-01-1355. URL: https://www.sae.org/content/2004-01-1355/ (visited on 06/13/2023).

[63] Meghnaa Dhanji et al. “Spray-wall Interactions: a Study of Impinging Sprays on Transient Thermal Loading and Fuel Film Deposition”. In: *ILASS Europe 2023*. 32nd Conference on Liquid Atomization & Spray Systems. Napoli, Italy, Sept. 4, 2023.

[64] Kamal Shway, Michele Bardi, and Sebastian A. Kaiser. “Quantitative UV-absorption imaging of liquid fuel films and their evaporation”. In: ().

[65] Florian Schulz, Jürgen Schmidt, and Frank Beyrau. “Development of a sensitive experimental set-up for LIF fuel wall film measurements in a pressure vessel”. In: *Exp Fluids* 56.5 (May 2015), p. 98. ISSN: 0723-4864, 1432-1114. DOI: 10.1007/s00348-015-1971-1. URL: http://link.springer.com/10.1007/s00348-015-1971-1 (visited on 06/14/2023).

[66] Jan N Geiler et al. “Development of laser-induced fluorescence to quantify in-cylinder fuel wall films”. In: *International Journal of Engine Research* 19.1 (Jan. 2018), pp. 134–147. ISSN: 1468-0874, 2041-3149. DOI: 10.1177/1468087417733865. URL: http://journals.sagepub.com/doi/10.1177/1468087417733865 (visited on 06/14/2023).

[67] Donald W. Stanton and Christopher J. Rutland. “Multi-dimensional modeling of thin liquid films and spray-wall interactions resulting from impinging sprays”. In: *International Journal of Heat and Mass Transfer* 41.20 (Oct. 1998), pp. 3037–3054. ISSN: 00179310. DOI: 10.1016/S0017-9310(98)00054-4. URL: https:

//linkinghub.elsevier.com/retrieve/pii/S0017931098000544 (visited on 03/02/2023).

[68] C. Bai, Henrik Rusche, and AD Gosman. “Modeling of gasoline spray impingement”. In: *Atomization and Sprays - ATOMIZATION SPRAYS* 12 (Jan. 2002), pp. 1–28. DOI: 10.1615/AtomizSpr.v12.i123.10.

[69] Chengxin Bai and A. D. Gosman. “Development of Methodology for Spray Impingement Simulation”. In: International Congress & Exposition. Feb. 1, 1995, p. 950283. DOI: 10.4271/950283. URL: https://www.sae.org/content/950283/ (visited on 02/26/2023).

[70] P. J. O’Rourke and A. A. Amsden. “A Spray/Wall Interaction Submodel for the KIVA-3 Wall Film Model”. In: SAE 2000 World Congress. Mar. 6, 2000, pp. 2000--01–0271. DOI: 10.4271/2000-01-0271. URL: https://www.sae.org/content/2000-01-0271/ (visited on 06/14/2023).

[71] Roberto Torelli et al. “Toward predictive and computationally affordable Lagrangian–Eulerian modeling of spray–wall interaction”. In: *International Journal of Engine Research* 21.2 (Feb. 2020), pp. 263–280. ISSN: 1468-0874, 2041-3149. DOI: 10.1177/1468087419870619. URL: http://journals.sagepub.com/doi/10.1177/1468087419870619 (visited on 02/26/2023).

[72] CHR. MUNDO, M. SOMMERFELD, and C. TROPEA. “DROPLET-WALL COLLISIONS: EXPERIMENTAL STUDIES OF THE DEFORMATION AND BREAKUP PROCESS”. In: ().

[73] A. L. Yarin and D. A. Weiss. “Impact of drops on solid surfaces: self-similar capillary waves, and splashing as a new type of kinematic discontinuity”. In: *J. Fluid Mech.* 283 (Jan. 25, 1995), pp. 141–173. ISSN: 0022-1120, 1469-7645. DOI: 10.1017/S0022112095002266. URL: https://www.cambridge.org/core/product/identifier/S0022112095002266/type/journal_article (visited on 03/04/2023).

[74] Rohit Mishra and Christopher Rutland. “Evaluating Surface Film Models for Multi-Dimensional Modeling of Spray-Wall Interaction”. In: WCX SAE World Congress Experience. Apr. 2, 2019, pp. 2019--01–0209. DOI: 10.4271/2019-01-0209. URL: https://www.sae.org/content/2019-01-0209/ (visited on 03/04/2023).

[75] Wenchuan Liu et al. “Eulerian–Lagrangian modeling of spray G atomization with focus on vortex evolution and its interaction with cavitation”. In: *Applied Mathematical Modelling* 107 (July 2022), pp. 103–132. ISSN: 0307904X. DOI: 10.1016/j.apm.2022.01.017. URL: https://linkinghub.elsevier.com/retrieve/pii/S0307904X22000427 (visited on 06/21/2023).

[76] Engine Combustion Network. *Primary Spray G Datasets*. Engine Combustion Network. URL: https://ecn.sandia.gov/gasoline-spray-combustion/target-condition/primary-spray-g-datasets/ (visited on 06/12/2023).

[77] Stephen B. Pope. *Turbulent flows*. IOP Publishing, 2001.

[78] Thierry Poinsot and D. Veynante. *Theoretical and numerical combustion*. 2nd ed. Philadelphia: Edwards, 2005. 522 pp. ISBN: 978-1-930217-10-2.

[79] *Explosion Dynamics Laboratory*. URL: https://shepherd.caltech.edu/EDL/PublicResources/sdt/thermo.html (visited on 06/16/2023).

[80] *Gasoline Surrogate | Combustion*. URL: https://combustion.llnl.gov/mechanisms/surrogates/gasoline-surrogate (visited on 06/16/2023).

[81] A. Leonard. “Energy Cascade in Large-Eddy Simulations of Turbulent Fluid Flows”. In: *Advances in Geophysics*. Vol. 18. Elsevier, 1975, pp. 237–248. ISBN: 978-0-12-018818-5. DOI: 10.1016/S0065-2687(08)60464-1. URL: https://linkinghub.elsevier.com/retrieve/pii/S0065268708604641 (visited on 06/16/2023).

[82] Franck Nicoud et al. “Using singular values to build a subgrid-scale model for large eddy simulations”. In: *Physics of Fluids* 23.8 (2011). DOI: 10.1063/1.3623274.

[83] I. B. Celik, Z. N. Cehreli, and I. Yavuz. “Index of Resolution Quality for Large Eddy Simulations”. In: *Journal of Fluids Engineering* 127.5 (Sept. 1, 2005), pp. 949–958. ISSN: 0098-2202, 1528-901X. DOI: 10.1115/1.1990201. URL: https://asmedigitalcollection.asme.org/fluidsengineering/article/127/5/949/478030/Index-of-Resolution-Quality-for-Large-Eddy (visited on 02/10/2023).

[84] Akira Yoshizawa and Kiyosi Horiuti. “A Statistically-Derived Subgrid-Scale Kinetic Energy Model for the Large-Eddy Simulation of Turbulent Flows”. In: *J. Phys. Soc. Jpn.* 54.8 (Aug. 15, 1985), pp. 2834–2839. ISSN: 0031-9015, 1347-4073. DOI: 10.1143/JPSJ.54.2834. URL: http://journals.jps.jp/doi/10.1143/JPSJ.54.2834 (visited on 02/12/2023).

[85] Alex B. Liu, Daniel Mather, and Rolf D. Reitz. “Modeling the Effects of Drop Drag and Breakup on Fuel Sprays”. In: International Congress & Exposition. Mar. 1, 1993, p. 930072. DOI: 10.4271/930072. URL: https://www.sae.org/content/930072/ (visited on 12/22/2022).

[86] A. Haider and O. Levenspiel. “Drag coefficient and terminal velocity of spherical and nonspherical particles”. In: *Powder Technology* 58.1 (May 1989), pp. 63–70. ISSN: 00325910. DOI: 10.1016/0032-5910(89)80008-7. URL: https://linkinghub.elsevier.com/retrieve/pii/0032591089800087 (visited on 01/03/2023).

[87] Rainer N. Dahms and Joseph C. Oefelein. “The significance of drop non-sphericity in sprays”. In: *International Journal of Multiphase Flow* 86 (Nov. 2016), pp. 67–85. ISSN: 03019322. DOI: 10.1016/j.ijmultiphaseflow.2016.07.010. URL: https://linkinghub.elsevier.com/retrieve/pii/S030193221530104X (visited on 01/29/2023).

[88] Tuan M. Nguyen et al. “The Corrected Distortion model for Lagrangian spray simulation of transcritical fuel injection”. In: *International Journal of Multiphase Flow* 148 (Mar. 2022), p. 103927. ISSN: 03019322. DOI: 10.1016/j.ijmultiphaseflow.2021.103927. URL: https://linkinghub.elsevier.com/retrieve/pii/S0301932221003311 (visited on 12/14/2022).

[89] Peter J. O’Rourke and Anthony A. Amsden. “The Tab Method for Numerical Calculation of Spray Droplet Breakup”. In: 1987 SAE International Fall Fuels and Lubricants Meeting and Exhibition. Nov. 1, 1987, p. 872089. DOI: 10.4271/872089. URL: https://www.sae.org/content/872089/ (visited on 02/08/2023).

[90] A. A. Amsden, P. J. O’Rourke, and T. D. Butler. “KIVA-II: A computer program for chemically reactive flows with sprays”. In: (May 1989). DOI: 10.2172/6228444. URL: https://www.osti.gov/biblio/6228444.

[91] Andreas Richter and Petr A. Nikrityuk. “Drag forces and heat transfer coefficients for spherical, cuboidal and ellipsoidal particles in cross flow at subcritical Reynolds numbers”. In: *International Journal of Heat and Mass Transfer* 55.4 (Jan. 2012), pp. 1343–1354. ISSN: 00179310. DOI: 10.1016/j.ijheatmasstransfer.2011.09.005. URL: https://linkinghub.elsevier.com/retrieve/pii/S0017931011005023 (visited on 12/22/2022).

[92] R.S. Miller, K. Harstad, and J. Bellan. “Evaluation of equilibrium and non-equilibrium evaporation models for many-droplet gas-liquid flow simulations”. In: *International Journal of Multiphase Flow* 24.6 (Sept. 1998), pp. 1025–1055. ISSN: 03019322. DOI: 10.1016/S0301-9322(98)00028-7. URL: https://linkinghub.elsevier.com/retrieve/pii/S0301932298000287 (visited on 01/02/2023).

[93] B Zuo, A M Gomes, and C J Rutland. “Modelling superheated fuel sprays and vaproization”. In: *International Journal of Engine Research* 1.4 (Aug. 1, 2000), pp. 321–336. ISSN: 1468-0874, 2041-3149. DOI: 10.1243/1468087001545218. URL: http://journals.sagepub.com/doi/10.1243/1468087001545218 (visited on 01/10/2023).

[94] Peter Stephan et al., eds. *VDI-Wärmeatlas: mit 1046 Abbildungen und 483 Tabellen*. 12. Auflage. Springer Reference Technik. Berlin [Heidelberg]: Springer Vieweg, 2019. 2082 pp. ISBN: 978-3-662-52988-1.

[95] Jörn Hinrichs et al. *Modelling of the transport mechanisms in the direct neighbourhood of evaporating fuel droplets*. Technical final report FVV no. 1263. Sept. 23, 2020.

[96] K. Luo, O. Desjardinsy, and H. Pitsch. *DNS of droplet evaporation and combustion in a swirling combustor*. Annual Research Briefs 2008. Center for Turbulence Research, NASA Ames/Stanford Univ., 2008.

[97] Zhi-Fu Zhou, Guan-Yu Lu, and Bin Chen. “Numerical study on the spray and thermal characteristics of R404A flashing spray using OpenFOAM”. In: *International Journal of Heat and Mass Transfer* 117 (Feb. 2018), pp. 1312–1321. ISSN: 00179310. DOI: 10.1016/j.ijheatmasstransfer.2017.10.095. URL: https://linkinghub.elsevier.com/retrieve/pii/S0017931017330958 (visited on 03/23/2023).

[98] Christopher Price et al. “AN APPROACH TO MODELING FLASH-BOILING FUEL SPRAYS FOR DIRECT-INJECTION SPARK-IGNITION ENGINES”. In: *Atomiz Spr* 26.12 (2016), pp. 1197–1239. ISSN: 1044-5110. DOI: 10.1615/AtomizSpr.2016015807. URL: http://www.dl.begellhouse.com/journals/6a7c7e10642258cc,40f1ad8b3f7a9795,743e9c612ff4d396.html (visited on 05/30/2023).

[99] G.I. Taylor and Great Britain Chemical Defence Experimental Establishment. *The Shape and Acceleration of a Drop in a High Speed Air Stream*. 1974. URL: https://books.google.de/books?id=veHJzQEACAAJ.

[100] Franz X. Tanner. “DEVELOPMENT AND VALIDATION OF A CASCADE ATOMIZATION AND DROP BREAKUP MODEL FOR HIGH-VELOCITY DENSE SPRAYS”. In: *Atomiz Spr* 14.3 (2004), pp. 211–242. ISSN: 1045-5110. DOI: 10.1615/AtomizSpr.v14.i3.20. URL: http://www.dl.begellhouse.com/journals/6a7c7e10642258cc,1a3536ab07ef4f94,42d549a8001c013a.html (visited on 02/09/2023).

[101] Huu P. Trinh, C. P. Chen, and M. S. Balasubramanyam. “Numerical Simulation of Liquid Jet Atomization Including Turbulence Effects”. In: *Journal of Engineering for Gas Turbines and Power* 129.4 (Oct. 1, 2007), pp. 920–928. ISSN: 0742-4795, 1528-8919. DOI: 10.1115/1.2747253. URL: https://asmedigitalcollection.asme.org/gasturbinespower/article/129/4/920/471434/Numerical-Simulation-of-Liquid-Jet-Atomization (visited on 02/09/2023).

[102] Mark A. Patterson and Rolf D. Reitz. “Modeling the Effects of Fuel Spray Characteristics on Diesel Engine Combustion and Emission”. In: *SAE Transactions* 107 (1998). Publisher: SAE International, pp. 27–43. ISSN: 0096-736X. URL: https://www.jstor.org/stable/44736506 (visited on 02/09/2023).

[103] Makoto Nagaoka and Kiyomi Kawamura. “A Deforming Droplet Model for Fuel Spray in Direct-Injection Gasoline Engines”. In: SAE 2001 World Congress. Mar. 5, 2001, pp. 2001--01–1225. DOI: 10.4271/2001-01-1225. URL: https://www.sae.org/content/2001-01-1225/ (visited on 02/09/2023).

[104] M. Pilch and C.A. Erdman. “Use of breakup time data and velocity history data to predict the maximum size of stable fragments for acceleration-induced breakup of a liquid drop”. In: *International Journal of Multiphase Flow* 13.6 (Nov. 1987), pp. 741–757. ISSN: 03019322. DOI: 10.1016/0301-9322(87)90063-2. URL: https://linkinghub.elsevier.com/retrieve/pii/0301932287900632 (visited on 02/09/2023).

[105] Donald W. Stanton and Christopher J. Rutland. “Modeling Fuel Film Formation and Wall Interaction in Diesel Engines”. In: International Congress & Exposition. Feb. 1, 1996, p. 960628. DOI: 10.4271/960628. URL: https://www.sae.org/content/960628/ (visited on 03/04/2023).

[106] Rolf D. Reitz and R. Diwakar. “Structure of High-Pressure Fuel Sprays”. In: SAE International Congress and Exposition. Feb. 1, 1987, p. 870598. DOI: 10.4271/870598. URL: https://www.sae.org/content/870598/ (visited on 01/23/2023).

[107] *CFD Data Search*. Engine Combustion Network. URL: https://ecn.sandia.gov/cfd-data-search/ (visited on 06/18/2023).

[108] Giovanni Tretola, Salvador Navarro-Martinez, and Konstantina Vogiatzaki. "Primary break-up characterisation and droplet statistics of multi-hole sprays using a probabilistic surface density methodology". In: (2022).

[109] Salvador Navarro-Martinez et al. "An investigation on the impact of small-scale models in gasoline direct injection sprays (ECN Spray G)". In: *International Journal of Engine Research* 21.1 (Jan. 2020), pp. 217–225. ISSN: 1468-0874, 2041-3149. DOI: 10.1177/1468087419889449. URL: http://journals.sagepub.com/doi/10.1177/1468087419889449.

[110] Matthieu Cordier, Lama Itani, and Gilles Bruneaux. "Quantitative measurements of preferential evaporation effects of multicomponent gasoline fuel sprays at ECN Spray G conditions". In: *International Journal of Engine Research* 21.1 (Jan. 2020), pp. 185–198. ISSN: 1468-0874, 2041-3149. DOI: 10.1177/1468087419838391. URL: http://journals.sagepub.com/doi/10.1177/1468087419838391 (visited on 03/17/2023).

[111] Ioannis Karathanassis et al. "Comparative Investigation of Gasoline-like Surrogate Fuels using 3D Computed Tomography". In: *ICLASS* 1.1 (Aug. 30, 2021). DOI: 10.2218/iclass.2021.5941. URL: http://journals.ed.ac.uk/ICLASS_Edinburgh/article/view/5941 (visited on 06/19/2023).

[112] Heechang Oh et al. "Spray collapse characteristics of practical GDI spray for lateral-mounted GDI engines". In: *International Journal of Heat and Mass Transfer* 190 (July 2022), p. 122743. ISSN: 00179310. DOI: 10.1016/j.ijheatmasstransfer.2022.122743. URL: https://linkinghub.elsevier.com/retrieve/pii/S0017931022002253 (visited on 06/28/2023).

[113] V. Ebrahimian and C. Habchi. "Towards a predictive evaporation model for multicomponent hydrocarbon droplets at all pressure conditions". In: *International Journal of Heat and Mass Transfer* 54.15 (July 2011), pp. 3552–3565. ISSN: 00179310. DOI: 10.1016/j.ijheatmasstransfer.2011.03.031. URL: https://linkinghub.elsevier.com/retrieve/pii/S0017931011001773 (visited on 04/24/2023).

[114] A. Bader, P. Keller, and C. Hasse. "The influence of non-ideal vapor–liquid equilibrium on the evaporation of ethanol/iso-octane droplets". In: *International Journal of Heat and Mass Transfer* 64 (Sept. 2013), pp. 547–558. ISSN: 00179310. DOI: 10.1016/j.ijheatmasstransfer.2013.04.056. URL: https:

//linkinghub.elsevier.com/retrieve/pii/S0017931013003700 (visited on 05/01/2023).

[115] S. Tonini and G.E. Cossali. "A novel formulation of multi-component drop evaporation models for spray applications". In: *International Journal of Thermal Sciences* 89 (Mar. 2015), pp. 245–253. ISSN: 12900729. DOI: 10.1016/j.ijthermalsci.2014.10.016. URL: https://linkinghub.elsevier.com/retrieve/pii/S1290072914003007 (visited on 05/02/2023).

[116] Fernando Luiz Sacomano Filho et al. "A new robust modeling strategy for multi-component droplet heat and mass transfer in general ambient conditions". In: *International Journal of Heat and Mass Transfer* 194 (Sept. 2022), p. 123102. ISSN: 00179310. DOI: 10.1016/j.ijheatmasstransfer.2022.123102. URL: https://linkinghub.elsevier.com/retrieve/pii/S0017931022005749 (visited on 04/24/2023).

[117] Lyle M. Pickett, Caroline L. Genzale, and Julien Manin. "UNCERTAINTY QUANTIFICATION FOR LIQUID PENETRATION OF EVAPORATING SPRAYS AT DIESEL-LIKE CONDITIONS". In: *Atomiz Spr* 25.5 (2015), pp. 425–452. ISSN: 1044-5110. DOI: 10.1615/AtomizSpr.2015010618. URL: http://www.dl.begellhouse.com/journals/6a7c7e10642258cc,441042be565b52ed,738986f63f3f0847.html.

[118] Fredrik R. Westlye et al. "Diffuse back-illumination setup for high temporally resolved extinction imaging". In: *Appl. Opt.* 56.17 (2017), pp. 5028–5038. DOI: 10.1364/AO.56.005028. URL: https://opg.optica.org/ao/abstract.cfm?URI=ao-56-17-5028.

[119] L.-P. Hsiang and G.M. Faeth. "Drop deformation and breakup due to shock wave and steady disturbances". In: *International Journal of Multiphase Flow* 21.4 (Aug. 1995), pp. 545–560. ISSN: 03019322. DOI: 10.1016/0301-9322(94)00095-2. URL: https://linkinghub.elsevier.com/retrieve/pii/0301932294000952 (visited on 02/02/2023).

[120] Grazia Lamanna et al. "Towards a unified treatment of fully flashing sprays". In: *International Journal of Multiphase Flow* 58 (Jan. 2014), pp. 168–184. ISSN: 03019322. DOI: 10.1016/j.ijmultiphaseflow.2013.08.010. URL: https://linkinghub.elsevier.com/retrieve/pii/S0301932213001298 (visited on 05/29/2023).

[121] P. Keller et al. “Experimental and numerical analysis of iso-octane/ethanol sprays under gasoline engine conditions”. In: *International Journal of Heat and Mass Transfer* 84 (May 2015), pp. 497–510. ISSN: 00179310. DOI: 10.1016/j.ijheatmasstransfer.2015.01.011. URL: https://linkinghub.elsevier.com/retrieve/pii/S0017931015000186 (visited on 06/26/2023).

[122] Daniel Mayer et al. “Experimental Investigation of Flame-Wall-Impingement and Near-Wall Combustion on the Piston Temperature of a Diesel Engine Using Instantaneous Surface Temperature Measurements”. In: International Powertrains, Fuels & Lubricants Meeting. Sept. 10, 2018, pp. 2018--01–1782. DOI: 10.4271/2018-01-1782. URL: https://www.sae.org/content/2018-01-1782/ (visited on 06/29/2023).

[123] Fabian Köpple et al. “Experimental Investigation of Fuel Impingement and Spray-Cooling on the Piston of a GDI Engine via Instantaneous Surface Temperature Measurements”. In: *SAE Int. J. Engines* 7.3 (Apr. 1, 2014), pp. 1178–1194. ISSN: 1946-3944. DOI: 10.4271/2014-01-1447. URL: https://www.sae.org/content/2014-01-1447/ (visited on 06/30/2023).

[124] E. Baum et al. “On The Validation of LES Applied to Internal Combustion Engine Flows: Part 1: Comprehensive Experimental Database”. In: *Flow Turbulence Combust* 92.1 (Jan. 2014), pp. 269–297. ISSN: 1386-6184, 1573-1987. DOI: 10.1007/s10494-013-9468-6. URL: http://link.springer.com/10.1007/s10494-013-9468-6 (visited on 04/21/2023).

[125] John B. Heywood. *Internal Combustion Engine Fundamentals. N. York: McGraw-Hill*. McGraw-Hill, 1988. ISBN: 0-07-028637-X.

[126] Cooper Welch et al. “The Effects of Intake Pressure on In-Cylinder Gas Velocities in an Optically Accessible Single-Cylinder Research Engine”. In: *SAE Technical Paper*. Apr. 2020. DOI: 10.4271/2020-01-0792.

[127] John L. Lumley and Gary R. Newman. “The return to isotropy of homogeneous turbulence”. In: *Journal of Fluid Mechanics* 82.1 (1977), pp. 161–178. DOI: 10.1017/S0022112077000585.

[128] K. -S. Choi and J. L. Lumley. “Return to isotropy of homogeneous turbulence revisited”. In: *Turbulence and Chaotic Phenomena in Fluids*. Jan. 1984, pp. 267–272.

[129] Kwing So Choi and John L. Lumley. “The return to isotropy of homogeneous turbulence”. In: *Journal of Fluid Mechanics* 436 (2001), pp. 59–84. ISSN: 00221120. DOI: 10.1017/S002211200100386X.

[130] Ivana Stiperski and Marc Calaf. “Dependence of near-surface similarity scaling on the anisotropy of atmospheric turbulence”. In: *Q.J.R. Meteorol. Soc.* 144.712 (Apr. 2018), pp. 641–657. ISSN: 0035-9009, 1477-870X. DOI: 10.1002/qj.3224. URL: https://onlinelibrary.wiley.com/doi/10.1002/qj.3224 (visited on 01/26/2023).

[131] Nicholas Hamilton and Raúl Bayoán Cal. “Anisotropy of the Reynolds stress tensor in the wakes of wind turbine arrays in Cartesian arrangements with counter-rotating rotors”. In: *Physics of Fluids* 27.1 (Jan. 2015), p. 015102. ISSN: 1070-6631, 1089-7666. DOI: 10.1063/1.4903968. URL: http://aip.scitation.org/doi/10.1063/1.4903968 (visited on 01/26/2023).

[132] James R. MacDonald and Claudia M. Fajardo. “Turbulence Anisotropy Investigations in an Internal Combustion Engine”. In: *Journal of Engineering for Gas Turbines and Power* 143.9 (Sept. 1, 2021), p. 091011. ISSN: 0742-4795, 1528-8919. DOI: 10.1115/1.4050633. URL: https://asmedigitalcollection.asme.org/gasturbinespower/article/143/9/091011/1105256/Turbulence-Anisotropy-Investigations-in-an (visited on 08/23/2023).

[133] Sergio Hoyas and Javier Jiménez. “Scaling of the velocity fluctuations in turbulent channels up to Re=2003”. In: *Physics of Fluids* 18.1 (Jan. 1, 2006), p. 011702. ISSN: 1070-6631, 1089-7666. DOI: 10.1063/1.2162185. URL: https://pubs.aip.org/pof/article/18/1/011702/255572/Scaling-of-the-velocity-fluctuations-in-turbulent (visited on 08/24/2023).

[134] Karri Keskinen et al. “Novel Insight into Engine Near-Wall Flows and Wall Heat Transfer Using Direct Numerical Simulations and High-Fidelity Experiments”. In: *21. Internationales Stuttgarter Symposium* 21 (2021), pp. 377–394. ISSN: 978-3-658-33521-2.

[135] HERMANN GERSTEN SCHLICHTING KLAUS. *BOUNDARY-LAYER THEORY*. Place of publication not identified: SPRINGER, 2000. ISBN: 978-3-662-57095-1.

[136] Yongxiang Li et al. “Non-equilibrium wall functions for large Eddy simulations of complex turbulent flows and heat transfer”. In: *International Journal of Heat and Fluid Flow* 88 (Apr. 2021), p. 108758. ISSN: 0142727X. DOI: 10.1016/j.ijheatfluidflow.2020.108758. URL: https://linkinghub.elsevier.com/retrieve/pii/S0142727X20310870 (visited on 12/01/2022).

[137] M. Popovac and K. Hanjalic. “Compound Wall Treatment for RANS Computation of Complex Turbulent Flows and Heat Transfer”. In: *Flow Turbulence Combust* 78.2 (Mar. 2007), p. 177. ISSN: 1386-6184, 1573-1987. DOI: 10.1007/s10494-

006-9067-x. URL: https://link.springer.com/10.1007/s10494-006-9067-x (visited on 12/02/2022).

[138] T. Karman V. “The Analogy between Fluid Friction and Heat Transfer”. In: *Transactions of the American Society of Mechanical Engineers* 61 (1939), pp. 705–710. URL: https://ci.nii.ac.jp/naid/10025293231.

[139] Tsan-Hsing Shih. “A Generalized Wall Function”. In: ().

[140] J. C. R. Hunt. “A First Course in Turbulence. By H. TENNEKES and J. L. LUMLEY. M.I.T. Press, 1972. 300pp.” In: *Journal of Fluid Mechanics* 58.4 (1973), pp. 816–819. DOI: 10.1017/S002211207321251X.

[141] Michael Manhart, Nikolaus Peller, and Christophe Brun. “Compound Wall Treatment for RANS Computation of Complex Turbulent Flows and Heat Transfer”. In: *Theoretical and Computational Fluid Dynamics* 22 (2008), pp. 243–260. DOI: 10.1007/s00162-007-0055-0.

[142] C. V. Tu and David Wood. “Wall pressure and shear stress measurements beneath an impinging jet”. In: *Experimental Thermal and Fluid Science* 13 (1996), pp. 364–373. DOI: 10.1016/S0894-1777(96)00093-3.

[143] Spalding. “A Single Formula for the "Law of the Wall"”. In: ().

[144] Florian Ries et al. “Entropy Generation Analysis and Thermodynamic Optimization of Jet Impingement Cooling Using Large Eddy Simulation”. In: *Entropy* 21 (2019), pp. 243–260. DOI: 10.3390/e21020129.

[145] Florian Ries. “Numerical Modeling and Prediction of Irreversibilities in Sub- and Supercritical Turbulent Near-Wall Flows”. PhD thesis. Technical University Darmstadt, Nov. 2018.